Master's thesis

NTNU
Norwegian University of Science and Technology
Faculty of Natural Sciences
Department of Physics

Alexandra Metallinou Log

Development and investigation of HLLC-type finite-volume methods for one and two-phase flow in pipes with varying cross-sectional area.

Master's thesis in Applied Physics and Mathematics
Supervisor: Svend Tollak Munkejord, Morten Hammer and Jon Andreas Støvneng

June 2020

NTNU
Norwegian University of
Science and Technology

Alexandra Metallinou Log

Development and investigation of HLLC-type finite-volume methods for one and two-phase flow in pipes with varying cross-sectional area.

Master’s thesis in Applied Physics and Mathematics
Supervisor: Svend Tollak Munkejord, Morten Hammer and Jon Andreas Støvneng
June 2020

Norwegian University of Science and Technology
Faculty of Natural Sciences
Department of Physics

NTNU
Norwegian University of
Science and Technology

Abstract

In this work, the numerical solver Harten-Lax-van Leer Contact (HLLC) is extended for the application to flow through pipes with varying cross-sectional area. In addition, the homogeneous equilibrium two-phase model (HEM) solved by HLLC is used to simulate the depressurization of a pipe with constant cross-sectional area and results are compared to experimental data. The work is motivated by the need for accurate methods simulating CO_2 flow in order to enable large-scale CO_2 capture and storage. Two methods, HLLC+S and HLLCS, are proposed for fluid flow in pipes with varying cross-sectional area. HLLC+S simply adds a source term to the HLLC scheme, whereas HLLCS is formulated to include the stationary wave which is present in the governing equations for variable cross-section flow. For subsonic flow, the HLLCS scheme involves a nonlinear system and for resonant cases the system might not have a solution. Two source terms are tested for this solver and they have different strengths and weaknesses. The HLLC+S and HLLCS solvers are tested on a number of Riemann problems with the ideal gas equation of state (EOS) and compared to exact solutions. HLLCS is found to be significantly more accurate than HLLC+S. HLLC+S does not converge to the exact solution for discontinuous area change. Its error is low for small discontinuities and increases for large discontinuities. For smooth converging-diverging nozzles, however, its estimates are satisfactory. HLLC+S is further employed with the HEM and the Peng-Robsinon EOS for converging-diverging nozzles and two Riemann problems, showing that the scheme is robust enough to simulate such problems. The results suggest that HLLCS should be extended for a general EOS and tested on two-phase flow due to its superior accuracy. The two-phase modelling is validated by a depressurization test with HLLC, as the results agree with experimental data. Three boundary conditions (BCs) of increasing complexity are tested for the outlet boundary for the depressurization test and they all give similar results.

Sammendrag

I dette arbeidet er den numeriske løseren Harten-Lax van Leer Contact (HLLC) utvidet for å anvendes på strømning i rør med varierende tverrsnitt. I tillegg blir den homogene likevekts-tofasemodellen (HEM) løst av HLLC for å simulere strømning i rør med konstant tverrsnitt og resultatene blir sammenlignet med eksperimentelle data. Dette arbeidet er motivert av behovet for nøyaktige metoder som kan simulere CO_2-strømning i rør for å muliggjøre storskala CO_2-fangst og -lagring. To metoder, HLLC+S og HLLCS, blir foreslått for strømning i rør med varierende tverrsnitt. HLLC+S legger kun til et kildeledd på HLLC-metoden, mens HLLCS er formulert for å inkludere den stasjonære bølgen tilstede i ligningssystemet for strømning med varierende tverrsnitt. For subsonisk strømning involverer HLLCS-løseren et ikke-lineært ligningssystem, og for resonante strømningstilfeller er det mulig at dette systemet ikke har en løsning. To kildeledd blir testet for HLLCS og de har ulike styrker og svakheter. HLLC+S- og HLLCS-løserne er testet på en rekke Riemannproblemer med tilstandsligningen for ideell gass, og sammenlignet med den eksakte løsningen. HLLCS er betydelig mer nøyaktig enn HLLC+S. HLLC+S konvergerer ikke til den eksakte løsningen for diskontinuerlig arealendring. Feilen til løseren er lav for små diskontinuiteter og øker for større diskontinuiteter. Estimatene til løseren er derimot tilfredsstillende for glatte konvergerende-divergerende dyser. HLLC+S blir videre anvendt på HEM med Peng-Robinsons tilstandsligning for konvergerende-divergerende dyser og to Riemannproblemer, som viser at metoden er robust nok til å simulere slike problemer. Resultatene antyder at HLLCS bør utvides for en generell tilstandsligning og testes for tofasestrømning grunnet dens overlegne nøyaktighet. Tofasemodelleringen er validert av en test for trykkavlastning med HLLC der resultatene stemmer godt overens med eksperimentelle data. Tre grensebetingelser av stigende kompleksitet er testet for utløpsgrensen til trykkavlastningstesten og alle gir lignende resultater.

Preface

This thesis is the final work for the degree Master of Science in Applied Physics and Mathematics at the Norwegian University of Science and Technology (NTNU). The work contributes to the research of NCCS Task 7 CO_2 transport, and is a collaboration with SINTEF Energy Research to investigate methods for CO_2 flow modelling. A long-term goal of the investigation is to contribute to efficient and safe large-scale CO_2 capture and storage for the reduction of global warming. Climate change is of great concern for me and I appreciate that I have the opportunity to contribute to research related to this topic.

For this work, I have had the pleasure of being under the guidance of Chief Scientist Svend Tollak Munkejord and Research Scientist Morten Hammer from SINTEF Energy Research, and Associate Professor Jon Andreas Støvneng from the Department of Physics at NTNU. The discussions with my supervisors from SINTEF have been invaluable. I am very grateful for the thorough feedback I have received from Svend Tollak on my texts and the many insights and advice I have received from Morten regarding thermophysical modelling. I am also grateful to Jon Andreas who has helped me with the formalities regarding the thesis.

Furthermore, I would like to thank Xian-Kui Zhu for the permission to use an image from his research in this thesis, Figure 1.1, and Nikolai Andrianov who kindly sent configuration files for his program CONSTRUCT to produce solutions of the non-unique Riemann problems in this work. Lastly, I must thank Sindre Stenen Blakseth who helped me through many, many fruitful discussions.

Trondheim, June 2020,
Alexandra Metallinou Log

Contents

Nomenclature

Abbreviations

BC	Boundary condition
CCS	CO_2 capture and storage
EOS	Equation of state
FVM	Finite-volume method
HEM	Homogeneous equilibrium two-phase model
HLL	Harten, Lax and van Leer (FVM)
HLLC	Harten, Lax and van Leer with Contact (FVM)
HLLC+S	Harten, Lax and van Leer with Contact plus Source (FVM)
HLLCS	Harten, Lax and van Leer with Contact and Source (FVM)
LxF	Lax-Friedrichs (FVM)
PR	Peng-Robinson (EOS)
RH	Rankine-Hugoniot

Greek letters

α_g	Volume fraction of gas	
α_l	Volume fraction of liquid	
Γ	First Grüneisen coefficient	
γ	Ratio of specific heats	
ρ	Density,	$\mathrm{kgm^{-3}}$

Latin letters

A	Cross-sectional area,	$\mathrm{m^2}$
C	Courant number	
c	Speed of sound,	$\mathrm{ms^{-1}}$
E	Specific total energy,	$\mathrm{Jkg^{-1}}$
e	Specific internal energy,	$\mathrm{Jkg^{-1}}$
H	Specific stagnation enthalpy,	$\mathrm{Jkg^{-1}}$

h	Specific enthalpy,	Jkg^{-1}
p	Pressure,	Pa
s	Specific entropy,	$\mathrm{JK}^{-1}\mathrm{kg}^{-1}$
T	Temperature,	K
u	Velocity in x-direction,	ms^{-1}
w_g	Mass fraction of gas	

1. Introduction

1.1. The importance of CCS and CO_2 flow modelling

The Intergovernmental Panel on Climate Change (IPCC) points to CO_2 capture and storage (CCS) as a key method to contain global warming within 1.5 °C [1, 2]. In their 2018 special report, IPCC investigated several different pathways for achieving the 1.5 °C target. Nearly all of the pathways needed the employment of CCS to achieve the target, especially for decarbonizing the industry sector [1]. However, CCS technology is new, and little large-scale CCS infrastructure exists at present.

Norway is in the front of the development for large-scale CCS in Europe [3], and partakes in projects involving all parts of the CCS chain; capture, transportation and storage [4]. In particular, the Northern Lights project [5] focuses on the transportation and storage infrastructure needed for CCS in Norway. A goal of the Northern Lights project is to create an infrastructure with excess capacity such that not only Norwegian industry, but also European industry, can send captured CO_2 for long-term storage [4, 5]. The CO_2 will be transported by ships and pipelines [5].

It is vital that the CO_2 transport pipelines can be operated safely and economically. CO_2 pipelines are shown to be more prone to running-ductile fracture than for example pipelines transporting natural gas [6, 7]. This means that if a pipe is punctured, it is more prone to "peel" open due to the great pressure within the pipe. The fracture can propagate along the pipe for several hundred meters [8, 6, 9]. In Figure 1.1, a pipe after a fracture propagation test is shown. A running-ductile fracture can be violent enough to hurl away rock and steel and release vast amounts of CO_2 into the air. This is a major safety hazard, especially because pipelines will likely be situated near densely populated areas [6, 10]. In order to design safe pipelines, accurate models predicting the depressurization behaviour of CO_2 are necessary [11].

SINTEF Energy Research is developing a numerical workbench to analyse models and numerical methods for modelling CO_2 flow in pipelines [11]. The different models are tested against results of depressurization experiments from a newly built experiment rig depicted in Figure 1.2 [12]. The present work is part of the research related to the development, analysis and testing of numerical methods for the simulation of CO_2 flow in pipes.

1.2. Investigating the HLLC method for CO_2 flow modelling

In the introductory project for this master's thesis [13], it was shown that the numerical method Harten-Lax-van Leer-Contact (HLLC) [14] performs well for the simulation of

Figure 1.1.: Image of a pipe from a fracture propagation test in [8]. Note that there is a person standing inside the pipe in the upper left of the picture, giving a sense of the scale of this fracture. The image is included with the permission of Xian-Kui Zhu.

Figure 1.2.: The pipe used for experiments at the roof of SINTEF Energy Research's laboratory. Credit: SINTEF Energy Research

CO_2 flow. The HLLC method is designed such that the separation between fluids of different densities is resolved more accurately than for other methods such as the FORCE method [15] currently implemented in SINTEF's numerical workbench. This is useful for resolving different phases of a fluid accurately. For CCS transport pipelines, the CO_2 will likely be in liquid or dense-liquid form [10], but there are many situations where two-phase liquid-gas flow can occur. Examples include; when CO_2 is first injected into the pipe, during depressurization of the pipelines for maintenance, and during shut-in of the pipeline, i.e. closing the pipeline in both ends [16, 17]. It is therefore an important advantage that HLLC captures such flow accurately. Inspired by this promising result, we have further investigated the performance of HLLC for pipeline flow

a) for pipes with varying cross-sectional area, and

b) for pipes with constant cross-sectional area and pressure-driven outflow boundary conditions.

For the flow in pipes with varying cross-sectional area, two new HLLC-type methods have been developed and tested.

1.2.1. Flow in pipes with varying cross-sectional area

In a realistic pipeline there will be valves and nozzles present in order to control the fluid flow. Such components change the cross-sectional area of the pipe. It is therefore of interest to simulate the effect of both abrupt and smooth cross-sectional area changes on compressible flow. The system of equations modelling compressible flow in pipes with varying cross-sectional area take the following form

$$\boldsymbol{U}_t + \boldsymbol{F}(\boldsymbol{U})_x = \boldsymbol{S}, \tag{1.1}$$

where $\boldsymbol{S}$ is a source term making the system nonconservative. This source term complicates numerical simulations greatly and can cause instability and oscillations [18, 19]. Furthermore, the system belongs to the class of *resonant* systems [20], leading to the possibility of up to three possible solutions, i.e. three different wave configurations, to an initial Riemann problem [18, 21].

Several authors have constructed numerical methods for the compressible nozzle flow equations (1.1) [19, 22, 23, 24], and systems of similar form [25, 26, 27, 28, 29], developing "well-balanced" [30] schemes to capture the flow behaviour at discontinuities. For example, Kröner and Thanh presented a well-balanced numerical scheme based on the Lax-Friedrichs flux [21], which they later extended by adding a non-linear equation to ensure correct wave configurations are found for resonant cases [19]. Here, they focused mainly on solutions for the ideal gas equation of state (EOS). Brown et al. [31] proposed the first methodology for resolving two-phase flow in pipes with discontinuous cross-sectional area changes for the homogeneous equilibrium two-phase flow model (HEM) using the AUSM+-up scheme.

HLLC has yet to be tested on the problem of compressible flow with discontinuous cross sections[1]. However, augmented versions of HLLC have been constructed for similar systems, where abrupt changes are accounted for [25, 26]. An augmented version of HLLC for the Baer-Nunziato (BN) equations [33] was developed by Tokareva and Toro, giving promising results for many test cases [25]. Murillo and García-Navarro also developed an augmented version of HLLC for the shallow-water equations [26]. This method produced promising results as well, though the authors note difficulties such as the need for a "source-fix" to avoid unphysical solutions in certain cases.

1.2.2. Pressure-driven outflow

In the project work, [13], HLLC was tested and compared to other numerical methods for the HEM with the Peng-Robinson EOS. In the tests, extrapolation was used at the boundaries. It is however of interest to see how HLLC performs with more realistic boundary conditions (BCs) for outflow in particular. This is relevant for the simulation of depressurization experiments. It is further of interest how different BCs affect different numerical methods.

1.3. Present contribution

In the present work, an augmented version of HLLC, "HLLCS", is developed for compressible flow in pipes with smooth and discontinuous cross-sections. In addition, the HLLC method with an added source term, "HLLC+S", is applied to simulate the flow for this system. The latter approach is more similar to that of Brown et al. [31]. The two methods are applied to problems for ideal gas EOS with known exact solutions and their results are compared. HLLCS was not extended for a general EOS in this work due to the time-frame available. HLLC+S is general in its formulation and was therefore applied to two-phase tests in converging-diverging nozzles, and similar two-phase tests as those presented by Brown et al. [31]. All the code needed to test the numerical methods applied in this work was written by the author in FORTRAN 90 for the ideal gas EOS, and the code was coupled with the in-house thermodynamic library of SINTEF Energy Research to test both HLLC and HLLC+S with the Peng-Robinson EOS.

A second focus of this work has been to validate the CO_2 flow model, the HEM with the PR EOS, by simulating a pipe depressurization and comparing the results to experimental data from SINTEF's experiment rig [12]. Three different pressure BCs for outflow are described and applied in depressurization tests with HLLC and the well-known Lax-Friedrichs (LxF) method on the HEM. The BCs are nearly the same as those applied by Munkejord and Hammer [11] for the depressurization of CO_2-rich mixtures in pipes. Though the BCs are not new, the author finds that BCs are often under-reported in the literature and they are therefore described in detail in Section 3.2.

---

[1] An HLLC method for compressible pipe flow in *smooth* nozzles has been developed by LeMartelot et al. [32].

1.4. Structure of the report

The report consists of five chapters. Chapter 1 is the Introduction. In Chapter 2, the physical modelling is introduced. Here, the systems for flow in a pipe with constant cross-sectional area and varying cross-sectional area are presented, and the equations of state applied to simulate the thermodynamics of the fluid are introduced: the ideal gas EOS and the Peng Robinson EOS. Lastly, the HEM is described. In Chapter 3, the numerical methods applied in this work are presented. LxF is briefly introduced. HLLC is described in Subsection 3.1.3, HLLC+S in Subsection 3.1.4 and HLLCS is derived in Subsection 3.1.6. All the HLLC-type methods require wave speed estimates, and these are presented in Subsection 3.1.9. The results of numerical tests are presented in Chapter 4. Tests with the ideal gas EOS for HLLC+S and HLLCS are given in Section 4.2, and two-phase tests for HLLC+S are shown in Section 4.3. Lastly, the depressurization test with LxF and HLLC is presented in Section 4.4. In Chapter 5, a brief summary of the results, concluding remarks and recommendations for further work are given.

2. Physical modelling

This chapter introduces the physical modelling of the system approximating the flow of ideal gas or CO_2 in pipes. First, some general thermodynamics is introduced in Section 2.1. The Euler equations are presented in Section 2.2 and it is explained how waves occur for this system of equations for a discontinuous initial condition. The Euler equations with cross-sectional area change are presented in Section 2.3 and the waves occurring for this system are also explained. In Section 2.4, two equations of state are presented, the ideal gas EOS and the Peng-Robinson EOS. Lastly, the homogeneous equilibrium model for two-phase flow is outlined.

2.1. General thermodynamics

Before we delve into the system of equations applied to describe the flow of CO_2, some general thermodynamics which is used extensively through this work is introduced. Firstly, we will need the first law of thermodynamics for a reversible process in a closed system,

$$\mathrm{d}e = T\,\mathrm{d}s + \frac{p}{\rho^2}\,\mathrm{d}\rho, \tag{2.1}$$

where e is the specific internal energy, i.e., internal energy per mass, s is the specific entropy, ρ is the density, p is the pressure and T is the temperature.

If the pressure in the fluid is expressed as a general function of the specific internal energy and the density, $p = p(\rho, e)$, then a small change in pressure, dp, can be expressed as

$$\mathrm{d}p = \left(\frac{\partial p}{\partial \rho}\right)_e \mathrm{d}\rho + \left(\frac{\partial p}{\partial e}\right)_\rho \mathrm{d}e = (c^2 - \Gamma\frac{p}{\rho})\,\mathrm{d}\rho + \Gamma\rho\,\mathrm{d}e, \tag{2.2}$$

where c is the speed of sound and Γ is the first Grüneisen parameter. The speed of sound, c, is defined by

$$c^2 = \left(\frac{\partial p}{\partial \rho}\right)_s, \tag{2.3}$$

which can be equivalently expressed as

$$c^2 = \left(\frac{\partial p}{\partial \rho}\right)_e + \frac{p}{\rho^2}\left(\frac{\partial p}{\partial e}\right)_\rho \tag{2.4}$$

by the 1^{st} law of thermodynamics. For a fluid, the speed of sound determines the speed at which pressure waves travel through it.

The first Grüneisen parameter is defined as follows;

$$\Gamma = \frac{1}{\rho}\left(\frac{\partial p}{\partial e}\right)_\rho . \tag{2.5}$$

Though a more common form, which can be found by the many equivalences between derivatives in thermodynamics, is

$$\Gamma = \frac{1}{\rho C_V}\left(\frac{\partial p}{\partial T}\right)_\rho , \tag{2.6}$$

where C_V is the specific heat capacity at constant volume.

A function relating thermodynamic state variables such as the pressure to the specific internal energy and the density, $p = p(\rho, e)$, is called an *equation of state* (EOS). Two equations of state are used in this work, the ideal gas EOS and the Peng-Robinson EOS which are detailed in Section 2.4. However, we will first explore the governing equations of the fluid flow in pipes and nozzles without specifying a particular EOS. We will only assume that there is some general EOS, $p = p(\rho, e)$, with derivative relation (2.2).

2.2. The 1D Euler Equations

The 1D Euler equations can be used to model the flow of a compressible fluid in pipes with constant cross-section. We will often call these equations simply the Euler equations as all the work will be in 1D. In this section, the 1D Euler equations are described and analyzed, and the Riemann problem for these equations is outlined briefly.

The 1D Euler equations describe the mass balance,

$$\frac{\partial \rho}{\partial t} + \frac{\partial \rho u}{\partial x} = 0, \tag{2.7}$$

momentum balance

$$\frac{\partial \rho u}{\partial t} + \frac{\partial(\rho u^2 + p)}{\partial x} = 0, \tag{2.8}$$

and energy balance

$$\frac{\partial E}{\partial t} + \frac{\partial(E + p)u}{\partial x} = 0, \tag{2.9}$$

in a closed system with constant cross-section, no source terms and no viscous stresses. Here u is the velocity in x-direction and E is the total energy, the sum of internal energy and kinetic energy of the fluid; $E = \rho e + \frac{1}{2}\rho u^2$.

The system of equations can be written more compactly as

$$\boldsymbol{U}_t + \boldsymbol{F}_x = \boldsymbol{0}, \tag{2.10}$$

where

$$\boldsymbol{U} = \begin{pmatrix} U_1 \\ U_2 \\ U_3 \end{pmatrix} = \begin{pmatrix} \rho \\ \rho u \\ E \end{pmatrix}, \ \boldsymbol{F}(\boldsymbol{U}) = \begin{pmatrix} F_1 \\ F_2 \\ F_3 \end{pmatrix} = \begin{pmatrix} \rho u \\ \rho u^2 + p \\ (E + p)u \end{pmatrix},$$

and the subscripts t and x refer to the temporal and spatial derivatives respectively. We can write Equation (2.10) in quasi-linear form by using the chain rule on $\boldsymbol{F} = \boldsymbol{F}(\boldsymbol{U})$,

$$\boldsymbol{U}_t + \boldsymbol{A}(\boldsymbol{U})\boldsymbol{U}_x = \boldsymbol{0}, \tag{2.11}$$

where $\boldsymbol{A}(\boldsymbol{U}) = \frac{\partial \boldsymbol{F}}{\partial \boldsymbol{U}}$ is the Jacobian matrix of the system, so $\boldsymbol{A}(\boldsymbol{U})\boldsymbol{U}_x = \frac{\partial \boldsymbol{F}}{\partial \boldsymbol{U}}\boldsymbol{U}_x = \boldsymbol{F}(\boldsymbol{U})_x$.

If we assume that $p = p(\rho, e)$ as mentioned in Section 2.1 we may, through some manipulation, write the Jacobian matrix as:

$$\boldsymbol{A} = \begin{pmatrix} 0 & 1 & 0 \\ c^2 - u^2 - \Gamma(e + \frac{p}{\rho} - \frac{1}{2}u^2) & (2-\Gamma)u & \Gamma \\ u(c^2 - (\Gamma+1)(e + \frac{1}{2}u^2 + \frac{p}{\rho}) + \Gamma u^2) & e + \frac{p}{\rho} + \frac{1}{2}u^2 - \Gamma u^2 & (\Gamma+1)u \end{pmatrix}. \tag{2.12}$$

The full derivation of $\boldsymbol{A}$ can be found in the preliminary work for this master's thesis [13] and is included in Appendix A.

The eigenvalues and corresponding eigenvectors of $\boldsymbol{A}$ are;

$$\lambda_1 = u - c, \quad \lambda_2 = u, \quad \lambda_3 = u + c, \tag{2.13}$$

and

$$\boldsymbol{r}_1 = \begin{pmatrix} 1 \\ u - c \\ H - uc \end{pmatrix}, \ \boldsymbol{r}_2 = \begin{pmatrix} 1 \\ u \\ H - \frac{c^2}{\Gamma} \end{pmatrix}, \ \boldsymbol{r}_3 = \begin{pmatrix} 1 \\ u + c \\ H + uc \end{pmatrix}, \tag{2.14}$$

where $H = \frac{E+p}{\rho}$ and is called the stagnation enthalpy. The Euler equations (2.10) constitute a *hyperbolic system* as they satisfy the following properties:

1. The eigenvalues λ_i of $\boldsymbol{A}$ are real and distinct.
2. The eigenvectors, $\boldsymbol{r}_i$, of $\boldsymbol{A}$ are linearly independent.

This means that $\boldsymbol{A}$ can be diagonalized with real eigenvalues;

$$\boldsymbol{R}^{-1}\boldsymbol{A}\boldsymbol{R} = \boldsymbol{\Lambda}, \tag{2.15}$$

where $\boldsymbol{R} = [\boldsymbol{r}_1, \boldsymbol{r}_2, \boldsymbol{r}_3]$ is the matrix of the right eigenvectors of $\boldsymbol{A}$, and $\boldsymbol{\Lambda}$ is the diagonal matrix of the eigenvalues of $\boldsymbol{A}$. The fact that the system is hyperbolic allows us to reformulate the Euler equations in their characteristic form. This formulation is closely linked to which waves will propagate through the fluid.

2.2.1. Characteristics and Riemann invariants

The Euler equations (2.10) can be rewritten as

$$\boldsymbol{R}^{-1}\boldsymbol{U}_t + \boldsymbol{R}^{-1}\boldsymbol{A}\boldsymbol{R}\boldsymbol{R}^{-1}\boldsymbol{U}_x = \boldsymbol{0}, \tag{2.16}$$

where we have multiplied the equation with $\boldsymbol{R}^{-1}$ from the left and multiplied $\boldsymbol{A}$ from the right with the identity matrix $\boldsymbol{I}$ which can be expressed as $\boldsymbol{I} = \boldsymbol{R}\boldsymbol{R}^{-1}$. The characteristic variables are defined by $\partial \boldsymbol{W} = \boldsymbol{R}^{-1}\partial \boldsymbol{U}$ which can be shown to be

$$\partial \boldsymbol{W} = \begin{pmatrix} -\dfrac{\rho}{2c}\partial u + \dfrac{1}{2c^2}\partial p \\ \partial \rho - \dfrac{1}{c^2}\partial p \\ \dfrac{\rho}{2c}\partial u + \dfrac{1}{2c^2}\partial p \end{pmatrix}, \tag{2.17}$$

as is done in Appendix B.

Thus, Equation (2.16) becomes

$$\boldsymbol{W}_t + \boldsymbol{\Lambda}\boldsymbol{W}_x = \boldsymbol{0}. \tag{2.18}$$

Equation (2.18) describes scalar transport equations for the components in $\boldsymbol{W}$, w_i, that are advected at the velocities λ_i,

$$\frac{\partial w_i}{\partial t} + \lambda_i \frac{\partial w_i}{\partial x} = 0, \ i = 1,\, 2,\, 3. \tag{2.19}$$

This gives that

$$\frac{\mathrm{d}w_i(x_i(t), t)}{\mathrm{d}t} = 0 \text{ on characteristic lines } \frac{\mathrm{d}x_i(t)}{\mathrm{d}t} = \lambda_i \ i = 1,\, 2,\, 3; \tag{2.20}$$

i.e. on the *characteristic lines*, defined by $\frac{\mathrm{d}x_i}{\mathrm{d}t} = \lambda_i$, the characteristic variables w_i are constant:

$$\text{on } \frac{\mathrm{d}x_1(t)}{\mathrm{d}t} = u - c, \quad \partial w_1 = 0 \Leftrightarrow \partial p - \rho c \partial u = 0 \tag{2.21}$$

$$\text{on } \frac{\mathrm{d}x_2(t)}{\mathrm{d}t} = u, \quad \partial w_2 = 0 \Leftrightarrow \partial p - c^2 \partial \rho = 0 \tag{2.22}$$

$$\text{on } \frac{\mathrm{d}x_3(t)}{\mathrm{d}t} = u + c, \quad \partial w_3 = 0 \Leftrightarrow \partial p + \rho c \partial u = 0. \tag{2.23}$$

These characteristic lines are not necessarily straight as both u and c vary over time. They describe three different waves propagating at the speed defined by the eigenvalues λ_i. Along these waves, information about the state where the waves originated from is carried, as the characteristic variables stay constant on them.

Some quantities stay constant *across* these waves. These quantities are called Riemann invariants and can be shown to be [34]

$$s, \ u + \frac{2c}{\Gamma} \quad \text{across} \quad \frac{\mathrm{d}x_1}{\mathrm{d}t} = u - c \tag{2.24}$$

$$u, p \quad \text{across} \quad \frac{\mathrm{d}x_2}{\mathrm{d}t} = u \tag{2.25}$$

$$s, u - \frac{2c}{\Gamma} \quad \text{across} \quad \frac{\mathrm{d}x_3}{\mathrm{d}t} = u + c. \tag{2.26}$$

This is key in formulating the solution of the Riemann problem, often called the shock tube problem in gas dynamics.

2.2.2. The Riemann problem for the Euler equations

The Riemann problem for the 1D Euler equations is the initial value problem (IVP):

$$\boldsymbol{U}_t + \boldsymbol{F}(\boldsymbol{U})_x = \boldsymbol{0}, \tag{2.27}$$

$$\boldsymbol{U}(x,0) = \begin{cases} \boldsymbol{U}_L, & \text{if } x < 0 \\ \boldsymbol{U}_R, & \text{if } x \geq 0 \end{cases}, \tag{2.28}$$

where $\boldsymbol{U}_L$ and $\boldsymbol{U}_R$ are two different constant states. This problem is particularly relevant to study as the numerical methods used to sove the Euler equations are formulated as approximate Riemann problem solvers.

As explained in the previous section, the Euler equations have three characteristic waves which propagate at the speed of the eigenvalues λ_i. There are three types of waves which can arise for the Euler equations: shocks, rarefactions and contact discontinuities. The middle wave is always a contact discontinuity, and the others are either rarefactions or shocks.

Contact discontinuities and shocks

Two of the possible waves which can occur for the Euler equations are discontinuities. For the wave associated with the eigenvalue $\lambda_2 = u$ we always have a *contact discontinuity*, signifying the contact of two fluids in different states. Near a contact discontinuity, the characteristics are parallel. Across a contact discontinuity, p and u stay constant while ρ and e (and therefore also s) are discontinuous. For the waves associated with λ_1 and λ_3 we either have shocks or rarefactions. The characteristics on either side of a shock converge. Across shocks all the variables ρ, u, e, and p are discontinuous.

The velocity of a discontinuous wave is determined by the Rankine-Hugoniot condition,

$$\boldsymbol{F}(\boldsymbol{U}_r) - \boldsymbol{F}(\boldsymbol{U}_l) = S(\boldsymbol{U}_r - \boldsymbol{U}_l), \tag{2.29}$$

where S is the speed of the wave. l signifies that the state is just to the left of the discontinuity and r that the state is just to the right of it. The Rankine-Hugoniot relation is extensively used in the derivation of the numerical methods HLLC and HLLCS.

Rarefaction waves

It is also possible that the wave associated with λ_2 or λ_3 (or both), is a rarefaction. For rarefaction waves, the variables ρ, u, e, and p change smoothly. Along lines of smooth flow, the entropy stays constant as is shown in Appendix C. Therefore the entropy is conserved across a rarefaction. During the depressurization of a pipe, a rarefaction wave will travel into the pipe, while a shock and a contact discontinuity will exit the pipe. The conservation of entropy across the rarefaction can then be used in order to formulate a boundary condition for the flow outlet.

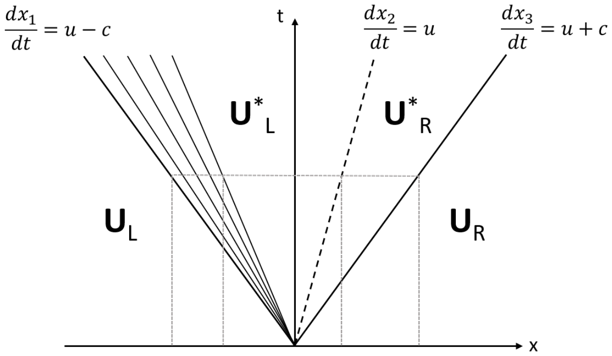

(a) Characteristics

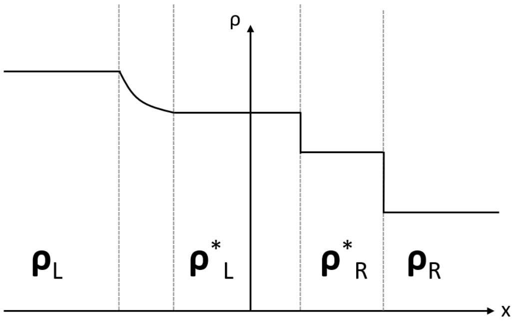

(b) Density solution

Figure 2.1.: A sketch of the characteristics (a) and density solution (b) for a Riemann problem where $\rho_L > \rho_R$ and $p_L > p_R$, giving a rarefaction to the left then a contact discontinuity and a shock to the right.

A full Riemann problem

We have now briefly outlined the different types of waves which can occur for the Euler equations. These waves can be combined to *connect* the left and right states given in the Riemann problem (2.28). An example of the solution to the Riemann problem (2.28) where all three possible waves occur is shown in Figure 2.1. Note that when showing the characteristic waves we assume that the time scale is short enough that u and c are approximately constant, so the characteristic lines are straight.

From information about the characteristics and the Riemann invariants, it is possible to find exact numerical solutions for the Riemann problem. Details on this can be found for example in [35], Chapter 4, for the special case of ideal gas EOS. However, determining the exact solution can be very computationally expensive for complex equations of state. This is why *approximate Riemann solvers* are used. HLLC is an example of an approximate Riemann solver and is presented in Chapter 3.

2.3. The 1D Euler equations with area change

The 1D Euler equations with area change can be used to model compressible fluid flow in nozzles, ducts and pipes with varying cross-sectional area. In the literature, the equations are referred to by many different names, amongst others we have: the Euler equations for compressible duct flow, the quasi one-dimensional Euler equations and the equations for fluid flow in nozzles with variable cross-section. We here choose to call the system *the Euler equations with area change* to make it clear what the difference between this system and the Euler equations is.

When area change is incorporated into the equations for mass, momentum and energy balance for the Euler equations, the following is obtained

$$\begin{pmatrix} \rho A \\ \rho u A \\ E A \end{pmatrix}_t + \begin{pmatrix} \rho u A \\ (\rho u^2 + p) A \\ (E + p) u A \end{pmatrix}_x = \begin{pmatrix} 0 \\ p \frac{\partial A}{\partial x} \\ 0 \end{pmatrix}. \tag{2.30}$$

where $A = A(x)$ denotes the cross-sectional area of an axisymmetric pipe. We now assume that the geometry of the system is fixed in time such that

$$\frac{\partial A}{\partial t} = 0. \tag{2.31}$$

This fourth equation is added to the system (2.30). The system can be written more compactly as

$$\boldsymbol{U}_t + \boldsymbol{F}(\boldsymbol{U})_x = \boldsymbol{S}, \tag{2.32}$$

where

$$\boldsymbol{U} = \begin{pmatrix} U_1 \\ U_2 \\ U_3 \\ U_4 \end{pmatrix} = \begin{pmatrix} \rho A \\ \rho u A \\ E A \\ A \end{pmatrix}, \quad \boldsymbol{F}(\boldsymbol{U}) = \begin{pmatrix} F_1 \\ F_2 \\ F_3 \\ F_4 \end{pmatrix} = \begin{pmatrix} \rho u A \\ (\rho u^2 + p) A \\ (E + p) u A \\ 0 \end{pmatrix}, \boldsymbol{S} = \begin{pmatrix} S_1 \\ S_2 \\ S_3 \\ S_4 \end{pmatrix} = \begin{pmatrix} 0 \\ p \frac{\partial A}{\partial x} \\ 0 \\ 0 \end{pmatrix}.$$

Here, $\boldsymbol{S}$ is a *nonlinear* source term. This system belongs to the class of *resonant* systems [18] which means that the waves which arise in this system can interact and "resonate" with each other. By expressing the system in a quasi-linear form and investigating the eigenvalues of the system, we can understand this better. We first rewrite the system (2.32) in nonconservative form such that the source term is included on the left hand side:

$$(\rho A)_t + (\rho u A)_x = 0 \tag{2.33}$$

$$(\rho u A)_t + \big((\rho u^2 + p) A\big)_x - p A_x = 0 \tag{2.34}$$

$$(E A)_t + ((E + p) u A)_x = 0 \tag{2.35}$$

$$A_t = 0. \tag{2.36}$$

If we assume a smooth solution, the system (2.33)-(2.36) can be rewritten in quasi-linear form,

$$\boldsymbol{U}_t + \boldsymbol{A}(\boldsymbol{U})\boldsymbol{U}_x = \boldsymbol{0}, \tag{2.37}$$

where $\boldsymbol{A}$ is the Jacobian matrix of the system. We assume that the pressure is given by some general equation of state (EOS), $p = p(e, \rho)$, such that the relation (2.2) holds, $dp = \left(c^2 - \Gamma\frac{p}{\rho}\right) d\rho + \Gamma\rho de$. Then $\boldsymbol{A}(\boldsymbol{U})$ can be found to be

$$\boldsymbol{A} = \begin{pmatrix} 0 & 1 & 0 & 0 \\ c^2 - u^2 - \Gamma(e + \dfrac{p}{\rho} - \dfrac{1}{2}u^2) & (2-\Gamma)u & \Gamma & p\Gamma - \rho c^2 \\ u\left(c^2 - (\Gamma+1)(e + \dfrac{1}{2}u^2 + \dfrac{p}{\rho}) + \Gamma u^2\right) & e + \dfrac{p}{\rho} + \dfrac{1}{2}u^2 - \Gamma u^2 & (\Gamma+1)u & u\left(p(\Gamma+1) - \rho c^2\right) \\ 0 & 0 & 0 & 0 \end{pmatrix}. \tag{2.38}$$

A full derivation of $\boldsymbol{A}$ can be found in Appendix D. The eigenvalues and corresponding eigenvectors of $\boldsymbol{A}$ are;

$$\lambda_0 = 0, \quad \lambda_1 = u - c, \quad \lambda_2 = u, \quad \lambda_3 = u + c, \tag{2.39}$$

and

$$\boldsymbol{r}_0 = \begin{pmatrix} 1 \\ 0 \\ e - \frac{1}{2}u^2 + \frac{u^2}{c^2}\frac{p}{\rho} \\ \frac{c^2 - u^2}{\rho c^2} \end{pmatrix}, \quad \boldsymbol{r}_1 = \begin{pmatrix} 1 \\ u - c \\ H - uc \\ 0 \end{pmatrix}, \quad \boldsymbol{r}_2 = \begin{pmatrix} 1 \\ u \\ H - \frac{c^2}{\Gamma} \\ 0 \end{pmatrix}, \quad \boldsymbol{r}_3 = \begin{pmatrix} 1 \\ u + c \\ H + uc \\ 0 \end{pmatrix}. \tag{2.40}$$

The three eigenvalues $\lambda_1, \lambda_2, \lambda_3$ are the same as for the Euler equations without area change. The eigenvalue $\lambda_0 = 0$, is associated with the area change. Note that any of the other eigenvalues λ_1, λ_2, λ_3 may coincide with λ_0. This is the cause of resonance in the system.

When λ_1 or λ_3 coincide with λ_0, the eigenvectors become linearly dependent and a parabolic degeneracy occurs [18]. Recalling the definition of a hyperbolic system,

1. The eigenvalues λ_i of $\boldsymbol{A}$ are real and distinct,
2. The eigenvectors, $\boldsymbol{r}_i$, of $\boldsymbol{A}$ are linearly independent,

the Euler equations with area change are *non-strictly hyperbolic* away from the points where $\lambda_1 = \lambda_0$ or $\lambda_3 = \lambda_0$.

As the system is not strictly hyperbolic, we cannot diagonalize $\boldsymbol{A}$ with distinct eigenvalues like we did for the Euler equations. However we can still determine which waves can arise in this system and find Riemann invariants across these waves.

2.3.1. Characteristics and Riemann invariants

In order to understand which waves can be present in the system of equations (2.32), we must determine the characteristic fields of the system. A thorough analysis on this is presented by Andrianov and Warnecke in [18]. Their results are here briefly summarized. In the following, we will assume that any change in area will be discontinuous. This is relevant as the numerical discretization presented in Chapter 3 assumes piece-wise constant data. We therefore either have no change in A or a discontinuous change in A.

When there is no change in A, the system (2.30) reduces to the familiar Euler equations (2.10). We then have the same characteristics and Riemann invariants as for the Euler equations associated with the eigenvalues $\lambda_1, \lambda_2, \lambda_3$, see Subsection 2.2.1. The Riemann invariants are, as shown earlier

$$s,\ u + \frac{2c}{\Gamma} \quad \text{across} \quad \frac{\mathrm{d}x_1}{\mathrm{d}t} = u - c \tag{2.41}$$

$$u, p \quad \text{across} \quad \frac{\mathrm{d}x_2}{\mathrm{d}t} = u \tag{2.42}$$

$$s, u - \frac{2c}{\Gamma} \quad \text{across} \quad \frac{\mathrm{d}x_3}{\mathrm{d}t} = u + c. \tag{2.43}$$

At points with discontinuous area change, there will be a wave associated with the eigenvalue $\lambda_0 = 0$, the 0-wave as it is often called. The 0-wave is a *stationary contact discontinuity* [21]. Across the 0-wave we have the following Riemann invariants as shown in [18]

$$A\rho u,\ s,\ h + \frac{1}{2}u^2, \ \text{across} \quad \frac{\mathrm{d}x_0}{\mathrm{d}t} = \lambda_0 = 0, \tag{2.44}$$

where $h = e + \frac{p}{\rho}$ is the specific enthalpy of the fluid. The invariants describe the conservation of mass flux, entropy and total enthalpy over the area change.

2.3.2. The Riemann problem for the Euler equations with area change

The Riemann problem for the 1D Euler equations with area change is the initial value problem (IVP):

$$\boldsymbol{U}_t + \boldsymbol{F}(\boldsymbol{U})_x = \boldsymbol{S}, \tag{2.45}$$

$$\boldsymbol{U}(x,0) = \begin{cases} \boldsymbol{U}_L, & \text{if } x < 0 \\ \boldsymbol{U}_R, & \text{if } x \geq 0 \end{cases}, \tag{2.46}$$

where $\boldsymbol{U}_L$ and $\boldsymbol{U}_R$ are two different constant states and $A_L \neq A_R$.

Away from the area change, we have the same waves as those which appear for the Euler equations without area change: shocks and/or rarefactions and a contact discontinuity between these. However, we also have the stationary contact discontinuity caused by the area change at $x = 0$ as introduced earlier. An example of a wave configuration for

Table 2.1.: Initial conditions for a Riemann problem with two possible solutions for the Euler equations with area change. The quantities here are dimensionless and $*_{\mathrm{ref}}$ denotes some reference value.

	p/p_{ref}	u/u_{ref}	ρ/ρ_{ref}	A/A_{ref}
Left	0.07	3.991	0.2069	0.8
Right	0.0833	-3.1666	0.1354	0.3

the Riemann problem is shown in Figure 2.2. Here the stationary wave is between a rarefaction and a contact discontiunity. This example was made in Andrianov's MATLAB program CONSTRUCT [36].

The 0-wave caused by the area change introduces two possible complications to the Riemann problem (2.45), (2.46): multiple solutions or *non-uniqueness* of the problem and *resonance*. Examples of these complications are provided below. Thorough mathematical analysis of these issues can be found in [18] and [19].

Riemann problems with non-unique solutions

In some cases it is possible to connect the left and right states, $\boldsymbol{U}_L$ and $\boldsymbol{U}_R$, in the Riemann problem with different sets of waves. This means that there are more than one solution to the problem. The initial condition for a Riemann problem with more than one solution is given in Table 2.1. This problem was proposed by Andrianov and Warnecke [18] and they show that both wave configuration A and wave configuration B as depicted in Figure 2.3 can connect the left and right states $\boldsymbol{U}_L, \boldsymbol{U}_R$. This raises the question: which wave configuration is the correct one?

Andrianov and Warnecke propose an entropy admissibility criterion which must be satisfied by *physically relevant* solutions: the solution must have the maximum increase in global entropy as compared to the other solutions. Here, they define physically relevant solutions as those which are most similar to the averaged result of 2D simulations for the same problem. The entropy admissibility criterion singles out configuration B in Figure 2.3 as the physical solution [18].

Resonant Riemann problems

In addition to the existence of more solutions than one, there are also resonant situations which can occur as one of the waves coincide with the 0-wave. An example, provided by Thanh and Kröner [19] is the following. A rarefaction to the left of the area change lasts until it resonates with the 0-wave so their speeds coincide. The interaction between the rarefaction and the 0-wave induces a shock before the contact discontinuity, and after the contact discontinuity another shock follows. A sketch of the characteristics and the density solution for this Riemann problem is shown in Figure 2.4. Details for deriving the solution of resonant states in the special case of ideal gas EOS can be found in [21].

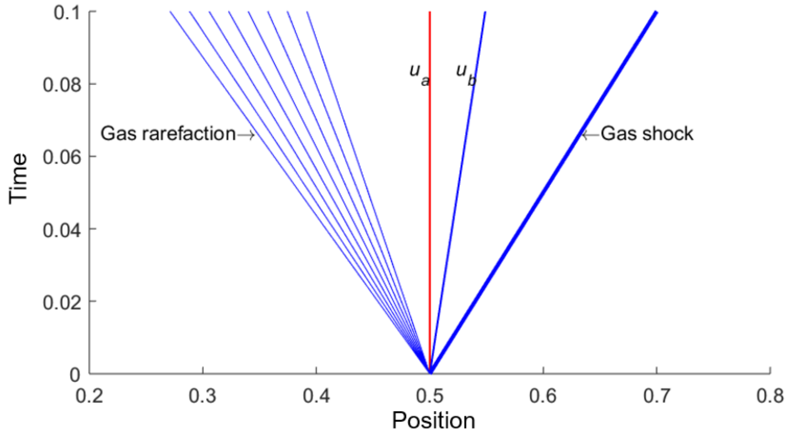

(a) Characteristics

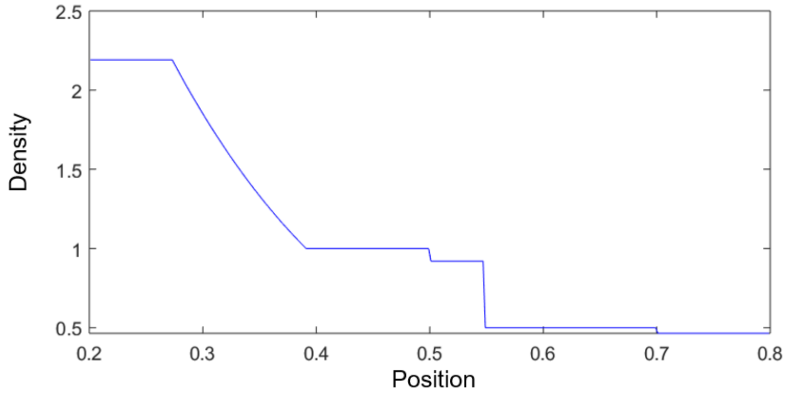

(b) Density solution for the characteristics

Figure 2.2.: The characteristics (a) and density solution (b) of a Riemann problem for the Euler equations with area change where $\rho_L > \rho_R$, $p_L > p_R$ and $A_L > A_R$, giving a rarefaction to the left, a stationary contact discontinuity, then a contact discontinuity and a shock to the right.

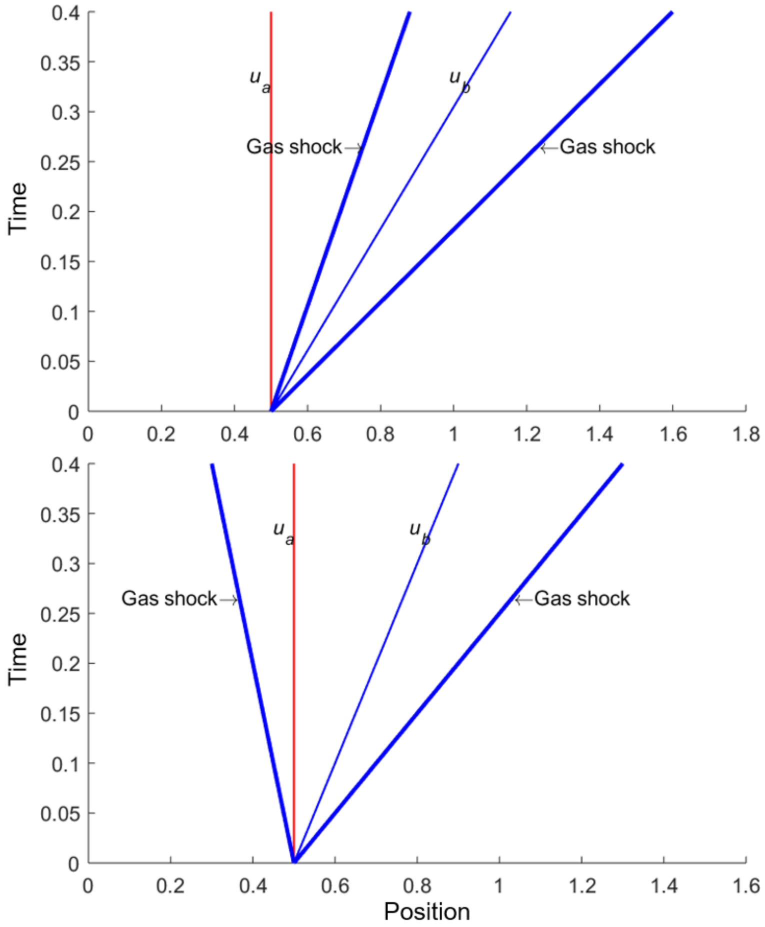

Figure 2.3.: Wave configurations A (top) and B (bottom) which are both exact solutions to the Riemann problem (2.45), (2.46) for the initial condition given in Table 2.1.

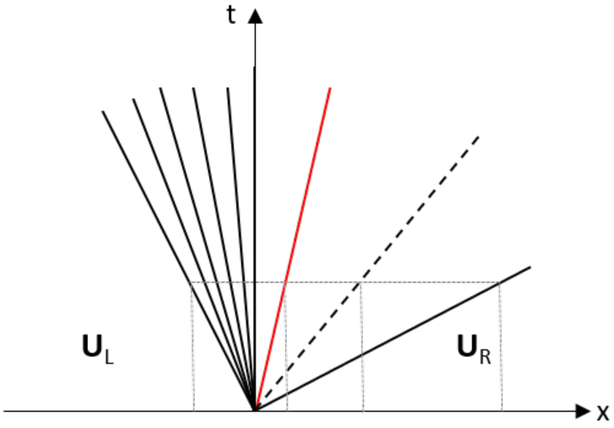

(a) Characteristics

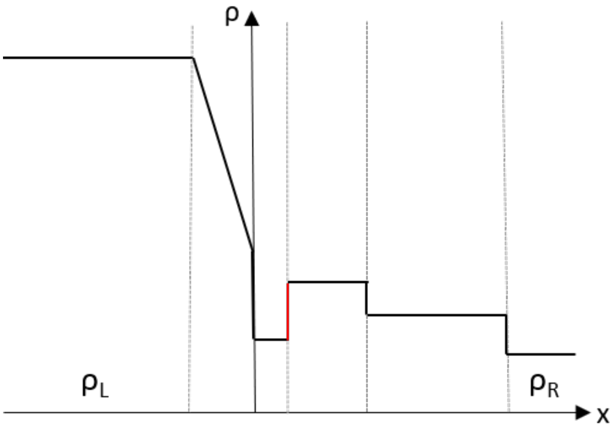

(b) Density solution

Figure 2.4.: The characteristics (a) and density solution (b) to a Riemann problem for the Euler equations with area change where a left rarefaction resonates with the stationary contact discontinuity at the area change inducing a further shock (red) before the contact discontinuity and shock to the right.

It is important that numerical solvers for this system can capture the resonant solutions in addition to non-resonant cases. This particular example of a resonant Riemann problem is shown because the solvers applied in this work, HLLC+S and HLLCS make assumptions about the wave structure in the problem and the occurrence of extra waves can affect their performance.

2.3.3. Analogy to the Baer-Nunziato equations

The Euler equations with area change can be formally obtained from the Baer-Nunziato (BN) equations which model the flow of gas and porous solid [33]. This is shown by Andrianov and Warnecke in [37] and is done by setting the solid speed in the BN equations to zero and letting the gas volume fraction take the role of the area, A.

An intuitive way of thinking about the analogy between the BN equations and the Euler equations with area change is to imagine that there are deposits of solid in the pipe being modeled causing changes in the cross-sectional area of the flow. A sketch of this is shown in Figure 2.5. The similarity between these two models means that solution methods found to work for one model can likely also be used for the other. Furthermore, complications which arise in one model will also arise in the other, such as non-uniqueness and resonance.

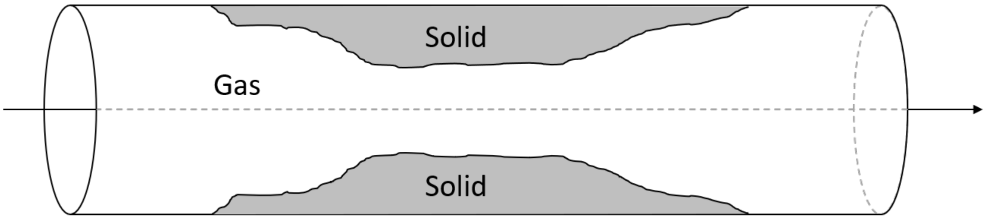

Figure 2.5.: A sketch of solid deposits causing cross-sectional area variations for the fluid flow.

2.3.4. Flow in smooth nozzles

Smooth nozzles can be used in numerous industrial and scientific applications. We will therefore outline briefly how compressible fluids flow in such nozzles, and later present tests for the numerical methods applied in this work for such a nozzle. In particular, the converging-diverging (CD) nozzle is described and used in tests.

CD nozzles are in general shaped as shown in Figure 2.6, though the length and size of the converging and diverging parts do not have to be equal. Such nozzles can be used in order to accelerate the fluid to *supersonic* flow in the diverging part of the nozzle. The section with the smallest cross-sectional area in a converging-diverging nozzle is called the throat. If the flow entering the nozzle is subsonic, the fluid flow at the throat is limited to a maximum Mach number, $M = \frac{u}{c}$ of one, i.e. choked flow. Depending on the relation between the stagnation pressure of the fluid p_0, and the back pressure p_b behind the nozzle, different types of flow can arise. These are the following, as illustrated in Figure 2.7 for flow passing a restriction:

- subsonic flow throughout the nozzle,
- flow which is exactly choked at the throat of the nozzle and then returns to subsonic,

- flow which is choked at the throat of the nozzle, becomes supersonic in the diverging part of the nozzle and returns to subsonic with a shock, and
- flow which transitions from subsonic to supersonic at the throat of the nozzle and stays supersonic through the nozzle.

If the flow entering the nozzle is supersonic, it will stay supersonic throughout the nozzle.

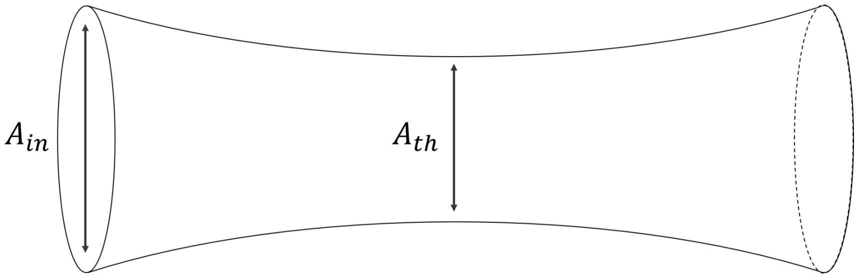

Figure 2.6.: Sketch of a converging-diverging nozzle. A_{th} is the cross-sectional area of the throat of the nozzle.

Along smooth lines of flow, the entropy is constant. This can be shown for the Euler equations with area change in a similar manner to how it is shown for the Euler equations in Appendix C. Therefore, if the fluid flow through the nozzle is smooth, i.e. there are no shocks, the relations for *isentropic* flow can be used to determine the fluid properties across the nozzle exactly. The exact solution is described in detail by for example Hansen [38] for the special case of ideal gas EOS. In Section 4.2.5 the numerical methods presented in this work are tested on a converging-diverging nozzle for ideal gas EOS and their results compared to the exact solution provided by Hansen.

2.4. Equations of state

Both for the Euler equations and the Euler equations with area change, we have one more unknown than equations. As mentioned in Section 2.1, we assume that some equation of state is given, relating the pressure to the specific internal energy and the density of the fluid. In this work, two equations of state have been used: the ideal gas EOS and the Peng-Robinson EOS.

2.4.1. Polytropic ideal gas EOS

For an ideal gas, its pressure is related to the density and internal energy by

$$p = \rho(\gamma - 1)e, \tag{2.47}$$

where γ is the *ratio of specific heats*,

$$\gamma = \frac{C_p}{C_v}, \tag{2.48}$$

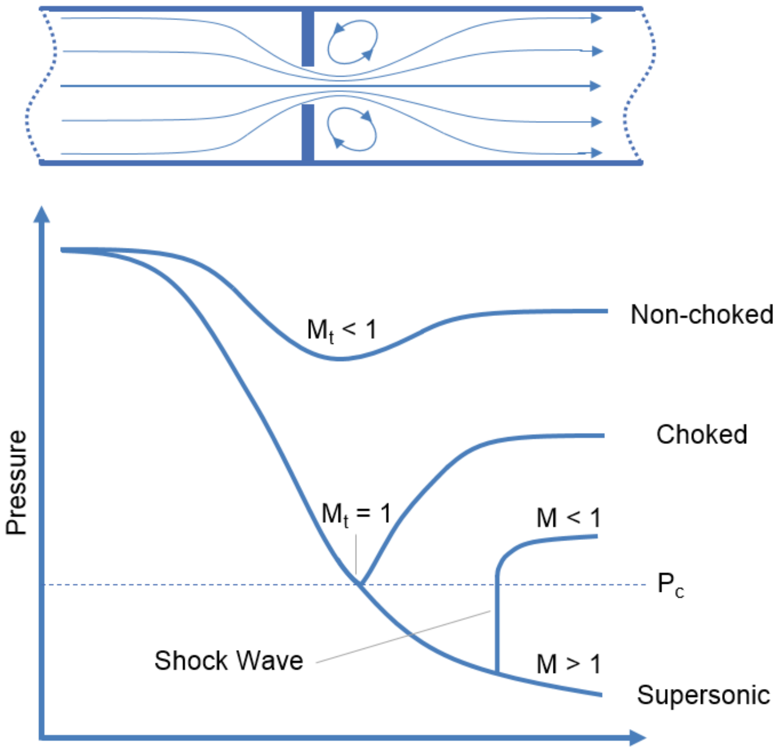

Figure 2.7.: Illustration of a fluid passing a restriction (top) and the effect on its pressure if the flow is subsonic through the restriction ($M = \frac{u}{c} < 1$) or choked ($M = 1$) (bottom). Credit: neutrium.net, created by Trevor Walker and Matthew Kidd

C_p is the specific heat at constant pressure and C_v is the specific heat at constant volume. For CO_2 at room temperature, $\gamma \approx 1.3$. For air in general, $\gamma \approx 1.4$. The latter value is often used in numerical tests in the literature and is therefore used for the numerical tests with ideal gas in Section 4.2.

The relevant variables introduced in Section 2.1, Γ and c, can be expressed with simple algebraic relations for ideal gas. Inserting the ideal gas EOS in the definition of Γ given in Section 2.1, we obtain

$$\Gamma = \frac{1}{\rho}\left(\frac{\partial p}{\partial e}\right)_\rho = \frac{1}{\rho}\left(\frac{\partial(\rho(\gamma-1)e)}{\partial e}\right)_\rho = \gamma - 1. \tag{2.49}$$

The speed of sound for ideal gas is found by inserting the EOS into Equation (2.4);

$$\begin{aligned} c^2 &= \left(\frac{\partial p}{\partial \rho}\right)_e + \frac{p}{\rho^2}\left(\frac{\partial p}{\partial e}\right)_\rho \\ &= (\gamma-1)e + \frac{p}{\rho^2}\rho(\gamma-1) \\ &= (\gamma-1)h. \end{aligned}$$

Though the ideal polytropic gas EOS is useful for initial tests, the EOS is exceedingly simple and cannot model liquids or solids.

2.4.2. Peng-Robinson EOS

The Peng-Robinson (PR) EOS [39] is a cubic EOS which allows for phase transitions between liquid and gas. With this EOS, one can study an approximation of the CO_2 in liquid form as well as in gaseous form allowing for both single-phase and two-phase flow.

The equation of state is given as follows;

$$p(T, V_m) = \frac{RT}{V_m - b} - \frac{a}{\sqrt{T}V_m(V_m + b)}, \tag{2.50}$$

where

$$a \approx 0.42748\frac{R^2 T_c^{5/2}}{p_c}, \tag{2.51}$$

and

$$b \approx 0.08664\frac{RT_c}{p_c}. \tag{2.52}$$

Here, V_m is the specific molar volume, T_c the critical temperature and p_c the critical pressure of the fluid. For CO_2, $T_c = 304.25\text{K}$ and $p_c = 7.39\text{MPa}$.

The PR EOS is implemented in SINTEF Energy Research's thermodynamics library which also includes functions to find V_m, e_m, p, T, Γ and c. Here,

$$e_m = eM_{\text{CO}_2},$$

where $M_{\mathrm{CO_2}}$ is the molar mass of $\mathrm{CO_2}$ in kg mol^{-1}, such that e is simply

$$e = \frac{e_m}{M_{\mathrm{CO_2}}}, \tag{2.53}$$

and ρ is found by

$$\rho = \frac{1}{V_m} M_{\mathrm{CO_2}}. \tag{2.54}$$

2.5. The homogeneous equilibrium two-phase flow model

As the PR EOS allows for both gas and liquid, it is important to consider how these phases flow if they are both present. Though it might be more realistic that gas flows faster than liquid, it is here assumed that the phases are *well-mixed* such that they travel at the same velocity;

$$u_{\mathrm{mix}} = u_l = u_g, \tag{2.55}$$

where l signifies liquid and g signifies gas. The density can be expressed as

$$\rho_{\mathrm{mix}} = \alpha_l \rho_l + \alpha_g \rho_g, \tag{2.56}$$

where α_l is the volume fraction of liquid and α_g the volume fraction of gas. The internal energy can be expressed by

$$e_{\mathrm{mix}} = \frac{\alpha_l \rho_l e_l + \alpha_g \rho_g e_g}{\rho_{\mathrm{mix}}}. \tag{2.57}$$

These mixture values are then used in the Euler equations or Euler equations with area change such that the mixture of liquid and gas is treated as only one fluid instead of two. It is further assumed that the liquid and gas are in equilibrium, i.e., that the phases have the same chemical potential, temperature and pressure.

The system described by the Euler equations (2.10) combined with (2.55)-(2.56) is called the homogeneous equilibrium two-phase flow model (HEM).

2.6. Determining the primitive variables

We are often interested in the primitive variables; p, u, and T, in addition to the conserved variables, ρ, ρu and E. The pressure, p, is especially important as it is needed to determine the flux vector, $\boldsymbol{F}$, in the Euler equations and Euler equations with area change. All the primitive variables can be found from the conserved variables. The velocity u is easily found by

$$u = \frac{\rho u}{\rho}. \tag{2.58}$$

In order to find p and T, e must be derived from the conserved variables:

$$e = \frac{1}{\rho}\left(E - \frac{1}{2}\rho u^2\right). \tag{2.59}$$

For the ideal gas EOS, p and T are then found from the EOS and the relation $e = C_v T$.

For the PR EOS, finding the primitive variables is more complicated since both phases (gas and liquid) might be present simultaneously. This allows for different states $(\rho_{\text{mix}}, e_{\text{mix}})$ to correspond to the same (p, T), but with different amounts of each phase present, i.e. different α_l and α_g.

The HEM assumes that the system is in thermodynamical equilibrium. For this assumption, an optimization problem (maximizing the entropy) can be solved to determine the equilibrium state (p, T) given $(\rho_{\text{mix}}, e_{\text{mix}})$. This equilibrium problem is called a “flash” and in this case a $\rho - e$ flash. In the optimization problem, the Peng-Robinson EOS must hold for p, T, and ρ_{mix}, of course.

When the system is discretized across a grid by the methods explained in the next chapter, such an optimization problem must be solved at *each* grid cell for the Peng-Robinson EOS. This is a computationally costly problem. Therefore methods with little numerical dissipation are desirable, such that rough grids can be used while still obtaining results of satisfactory accuracy. The numerical method HLLC is known for its low dissipation and it is therefore applied in this work and extended for the Euler equations with area change. The methods are described in detail in the following chapter.

3. Numerical methods

In this chapter, the numerical methods applied in this work are presented. In Section 3.1 finite volume methods (FVMs) are introduced and two different discretizations for systems with source terms are presented. The FVMs Lax-Friedrichs and HLLC are described for the Euler equations and the FVMs HLLC+S and HLLCS are proposed for the solution of the Euler equations with area change. All the HLLC-type methods need estimates of the wave speeds in the problem, and Roe average-based estimates are given in Subsection 3.1.9. In Section 3.2 the different boundary conditions applied for depressurization tests with the Euler equations are described.

3.1. Finite-volume methods

We will now introduce finite-volume methods. This introduction is largely based on the description in the preliminary work for this thesis [13] and Leveque's book [34], Chapter 4. In order to obtain numerical solutions of the Euler equations (2.10) and the Euler equations with area change (2.32), FVMs are applied. FVMs are based on discretizing the spatial domain into small control volumes or *grid cells*, Ω_j, and integrating the conservation laws across them [34], [13]. As we are working in one dimension, "volume" here means an interval along the x-axis. Assuming we are estimating flow in $x \in [a, b]$ and we subdivide this interval into N_j equally spaced grid cells, then Ω_j is the interval

$$\Omega_j = [x_{j-1/2}, x_{j+1/2}],\ \mathrm{j} = 1,\, 2, \dots N_j$$

and

$$\begin{cases} x_{j+1/2} = x_a + j\Delta x & \mathrm{j} = 1,\, 2, \dots N_j \\ x_{j-1/2} = x_a + (j-1)\Delta x & \mathrm{j} = 1,\, 2, \dots N_j \end{cases}$$

are the eastern and western faces of Ω_j. We denote the midpoints of the cells as $x_j = \frac{1}{2}(x_{j+1/2} + x_{j-1/2})$. An illustration of the setup is shown in Figure 3.1.

In FVMs, the value of an unknown in the cell Ω_j, ϕ_j, is approximated as the cell average:

$$\phi_j \approx \frac{1}{\Delta x} \int_{x_j - 1/2}^{x_j + 1/2} \phi(x)\, \mathrm{d}x, \quad \mathrm{j} = 1,\, 2, \dots N_j. \tag{3.1}$$

This gives a piecewise constant solution with discontinuities at the interfaces $x_{j-1/2}$, $x_{j+1/2}$, which allows us to use the theory of Riemann problems at the interfaces to approximate the flux passing through.

FVMs assume that the average flux across a grid face can be expressed by some *flux function* involving the values at either side of the grid face where the flux passes through.

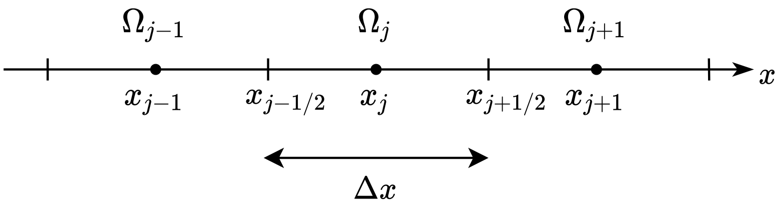

Figure 3.1.: A one dimensional interval subdivided into grid cells, Ω_j, with cell centers at x_j and faces $x_{j-1/2}$, $x_{j+1/2}$. These are the finite volumes in the finite-volume method.

In this work, two different types of FVM are used, one based on simply integrating (2.32) across the grid cell $[x_{j-1/2}, x_{j+1/2}]$ directly, and another based on incorporating the source term into the flux functions. The first approach is based on Brown et al.'s discretization [31] and yields

$$\frac{d\boldsymbol{U}_j}{dt} = -\frac{1}{\Delta x}\left(\boldsymbol{\mathcal{F}}_{j+1/2} - \boldsymbol{\mathcal{F}}_{j-1/2}\right) + \widetilde{\boldsymbol{S}}_j, \tag{3.2}$$

where $\boldsymbol{\mathcal{F}} = \boldsymbol{\mathcal{F}}(\boldsymbol{U}_L, \boldsymbol{U}_R)$ is a numerical flux function approximating the average flux $\boldsymbol{F}$ at the cell interfaces $x = x_{j-1/2}, x = x_{j+1/2}$, and $\widetilde{\boldsymbol{S}}_j$ approximates the contribution of the source term in cell j. Brown et al. use a 4-stage second order Low Storage Strong Stability Preserving Runge–Kutta method for the temporal discretization with this FVM [31]. In the present study however, an Euler time step is used, such that the full discretization becomes

$$\boldsymbol{U}_j^{n+1} = \boldsymbol{U}_j^n - \frac{\Delta t}{\Delta x}\left(\boldsymbol{\mathcal{F}}_{j+1/2} - \boldsymbol{\mathcal{F}}_{j-1/2}\right) + \Delta t \widetilde{\boldsymbol{S}}_j. \tag{3.3}$$

The second FVM is a conservative Godunov scheme which includes the source term in the numerical flux functions [26]. The FVM takes the following form

$$\boldsymbol{U}_j^{n+1} = \boldsymbol{U}_j^n - \frac{\Delta t}{\Delta x}\left(\boldsymbol{\mathcal{F}}^-_{j+1/2} - \boldsymbol{\mathcal{F}}^+_{j-1/2}\right), \tag{3.4}$$

where again an Euler time step is used for the temporal discretization. Here, $\boldsymbol{\mathcal{F}}^\pm = \boldsymbol{\mathcal{F}}^\pm(\boldsymbol{U}_L, \boldsymbol{U}_R, \boldsymbol{S})$ are numerical flux functions approximating the average flux, $\boldsymbol{F}$, *right next to* the east, $\boldsymbol{F}^-_{j+1/2}$, and west, $\boldsymbol{F}^+_{j-1/2}$, faces of the grid cells as depicted in Figure 3.2. As $\boldsymbol{S} = 0$ for the Euler equations, $\boldsymbol{\mathcal{F}}^+_{j+1/2} = \boldsymbol{\mathcal{F}}^-_{j+1/2} = \boldsymbol{\mathcal{F}}_{j+1/2}$.

Different finite-volume methods approximate the fluxes $\boldsymbol{F}_{j\pm1/2}$ in different ways. In the following, the Lax-Friedrichs FVM will be briefly introduced, we will show how the HLLC method approximates the fluxes for the Euler equations and suggest two modified HLLC-type methods to approximate the fluxes for the Euler equations with area change.

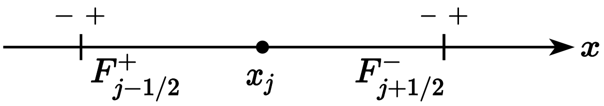

Figure 3.2.: The flux function $\mathcal{F}^+_{j-1/2}$ approximates the flux $F^+_{j-1/2}$ just to the right of the interface at $x_{j-1/2}$. The flux function $\mathcal{F}^-_{j+1/2}$ approximates the flux $F^-_{j+1/2}$ just to the left of the interface at $x_{j+1/2}$.

3.1.1. Lax-Friedrichs

A simple, robust, but very dissipative FVM is the Lax-Friedrichs (LxF) method. This method has the following numerical flux function

$$\boldsymbol{\mathcal{F}}_{j+1/2} = \frac{1}{2}\left(\boldsymbol{F}(\boldsymbol{U}_j) + \boldsymbol{F}(\boldsymbol{U}_{j+1}) - \frac{\Delta x}{\Delta t}(\boldsymbol{U}_{j+1} - \boldsymbol{U}_j)\right). \tag{3.5}$$

Due to the dissipative nature of this numerical scheme, the grid must be very fine to obtain reasonable results. This method, in addition to the HLLC method, is used to test the different boundary conditions suggested for the pipe outlet during depressurization in Section 3.2. HLLC is a less dissipative method. Its derivation is outlined below.

3.1.2. Integral relations for the Euler equations

We wish to derive an approximate solver of the cell interface Riemann problem

$$\boldsymbol{U}(x,0) = \begin{cases} \boldsymbol{U}_L, & \text{if } x < 0, \\ \boldsymbol{U}_R, & \text{if } x \geq 0. \end{cases} \tag{3.6}$$

for the Euler equations,

$$\boldsymbol{U}_t + \boldsymbol{F}_x = \boldsymbol{0}, \tag{3.7}$$

where

$$\boldsymbol{U} = \begin{pmatrix} \rho \\ \rho u \\ E \end{pmatrix}, \ \boldsymbol{F}(\boldsymbol{U}) = \begin{pmatrix} \rho u \\ \rho u^2 + p \\ (E+p)u \end{pmatrix}.$$

In order to derive a solver, we will determine some conditions the solver must satisfy which the exact solution fulfills. One such condition can be found through integral relations for the Euler equations. The following approach was proposed by Harten, Lax and van Leer in 1983 [40] when deriving the Harten-Lax-van Leer (HLL) method and is also used for the derivation of the HLLC method.

Consider the control volume $[x_L, x_R] \times [0, \Delta t]$ depicted in Figure 3.3 which contains the entire wave structure arising from the exact solution of the Riemann problem for the

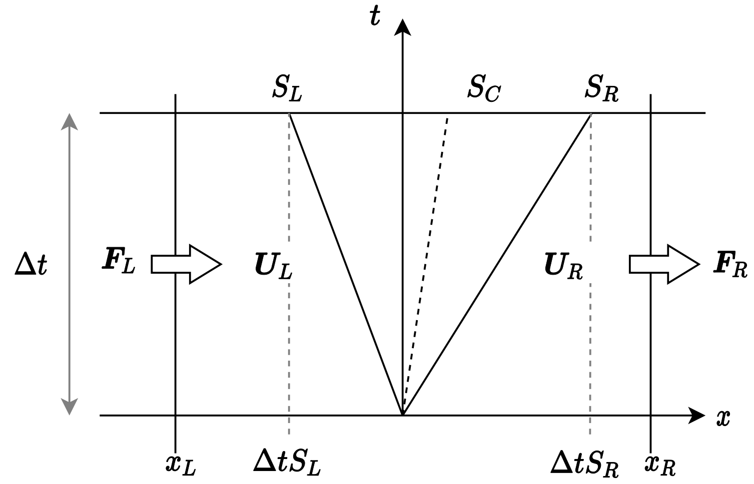

Figure 3.3.: A control volume $[x_L, x_R] \times [0, \Delta t]$ which contains the entire wave structure arising from the Riemann problem for the Euler equations. S_L and S_R are the fastest signal velocities coming from the Riemann problem.

Euler equations. We then have that

$$x_L \leq \Delta t S_L, \; x_R \geq \Delta t S_R, \tag{3.8}$$

where S_L and S_R are the fastest signal velocities arising from the initial condition of the Riemann problem, and Δt is a chosen time step.

If we integrate the conservation law (3.7) over the control volume, the following is found

$$\int_{x_L}^{x_R} \int_0^{\Delta t} \left(\frac{\partial \boldsymbol{U}}{\partial t} + \frac{\partial \boldsymbol{F}}{\partial x} \right) \mathrm{d}t \, \mathrm{d}x = 0$$

$$\int_{x_L}^{x_R} \boldsymbol{U}(x, \Delta t) - \boldsymbol{U}(x, 0) \, \mathrm{d}x + \int_0^{\Delta t} \boldsymbol{F}(x_R, t) - \boldsymbol{F}(x_L, t) \, \mathrm{d}t = 0$$

$$\Rightarrow \int_{x_L}^{x_R} \boldsymbol{U}(x, \Delta t) \, \mathrm{d}x = \int_{x_L}^{x_R} \boldsymbol{U}(x, 0) \, \mathrm{d}x - \left(\int_0^{\Delta t} \boldsymbol{F}(x_R, t) \, \mathrm{d}t - \int_0^{\Delta t} \boldsymbol{F}(x_L, t) \, \mathrm{d}t \right) \tag{3.9}$$

Computing the integrals on the right hand side of Equation (3.9) gives the following

$$\int_{x_L}^{x_R} \boldsymbol{U}(x, \Delta t) \, \mathrm{d}x = x_R \boldsymbol{U}_R - x_L \boldsymbol{U}_L - (\boldsymbol{F}_R - \boldsymbol{F}_L) \, \Delta t. \tag{3.10}$$

Equation (3.10) is referred to as the *consistency condition.* Approximate solutions to the Riemann problem must satisfy this condition.

If we choose $x_L = S_L \Delta t$ and $x_R = S_R \Delta t$, we can find a relation for the integral over the intermediate states bounded by the signal speeds S_L and S_R.

$$\int_{S_L \Delta t}^{S_R \Delta t} \boldsymbol{U}(x, \Delta t)\, \mathrm{d}x = S_R \Delta t \boldsymbol{U}_R - S_L \Delta t \boldsymbol{U}_L - \Delta t \left(\boldsymbol{F}_R - \boldsymbol{F}_L\right)$$

$$\Rightarrow \frac{1}{\Delta t (S_R - S_L)} \int_{S_L \Delta t}^{S_R \Delta t} \boldsymbol{U}(x, \Delta t)\, \mathrm{d}x = \frac{S_R \boldsymbol{U}_R - S_L \boldsymbol{U}_L - (\boldsymbol{F}_R - \boldsymbol{F}_L)}{S_R - S_L} \tag{3.11}$$

As stated by Toro [35], Equation (3.11) shows that the integral average over the intermediate states between S_L and S_R at time Δt is a known constant, provided that S_L and S_R are known. Different methods for approximating these wave speeds are presented in Section 3.1.9. In order for an approximate solution of the Riemann problem to satisfy the consistency condition, the integral average of its approximate intermediate states across a control volume must satisfy Equation (3.11).

3.1.3. HLLC approximate Riemann solver for the Euler equations

A detailed derivation of the HLLC method is given here as the same method is later used to derive an augmented version of HLLC for the Euler equations with area change. This derivation follows closely that presented in Toro's book, [35] Section 10.4.

The HLLC method proposed by Toro, Spruce and Speares [14], approximates the cell interface Riemann problem by a three-wave solution;

$$\widetilde{\boldsymbol{U}}(x/t) = \begin{cases} \boldsymbol{U}_L, & \text{if } x < S_L t, \\ \boldsymbol{U}_L^{HLLC}, & \text{if } S_L t \leq x < S_C t, \\ \boldsymbol{U}_R^{HLLC}, & \text{if } S_C t \leq x < S_R t, \\ \boldsymbol{U}_R, & \text{if } x \geq S_R t, \end{cases} \tag{3.12}$$

where

$$\boldsymbol{U}_L^{HLLC} = \frac{1}{\Delta t (S_C - S_L)} \int_{\Delta t S_L}^{\Delta t S_C} \boldsymbol{U}(x, \Delta t)\, \mathrm{d}x \tag{3.13}$$

and

$$\boldsymbol{U}_R^{HLLC} = \frac{1}{\Delta t (S_R - S_C)} \int_{\Delta t S_C}^{\Delta t S_R} \boldsymbol{U}(x, \Delta t)\, \mathrm{d}x \tag{3.14}$$

such that the consistency condition becomes

$$\left(\frac{S_C - S_L}{S_R - S_L}\right) \boldsymbol{U}_L^{HLLC} + \left(\frac{S_R - S_C}{S_R - S_L}\right) \boldsymbol{U}_R^{HLLC} = \frac{S_R \boldsymbol{U}_R - S_L \boldsymbol{U}_L - (\boldsymbol{F}_R - \boldsymbol{F}_L)}{S_R - S_L}. \tag{3.15}$$

S_C is the speed of the middle wave and S_L and S_R are approximations of the smallest and largest wave speeds at the interface $x_{j+1/2}$. A sketch of the HLLC scheme's approximate solution is given in Figure 3.4.

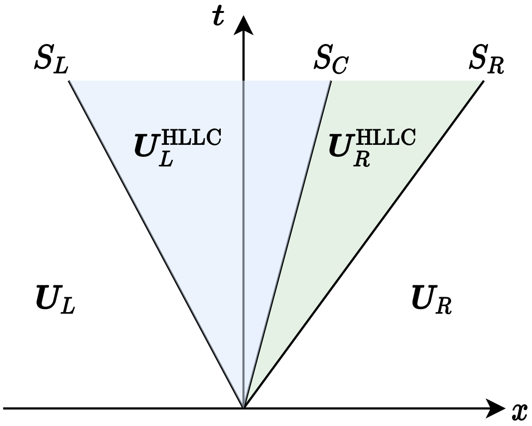

Figure 3.4.: HLLC assumes a three-wave solution, giving two intermediate states, separated by the contact wave.

This gives a numerical flux function

$$\boldsymbol{\mathcal{F}}_{j+1/2} = \begin{cases} \boldsymbol{F}_L, & \text{if } 0 < S_L, \\ \boldsymbol{F}_L^{HLLC}, & \text{if } S_L \leq 0 < S_C, \\ \boldsymbol{F}_R^{HLLC}, & \text{if } S_C \leq 0 < S_R, \\ \boldsymbol{F}_R, & \text{if } 0 \geq S_R. \end{cases} \tag{3.16}$$

The intermediate state fluxes, $\boldsymbol{F}_L^{HLLC}$ for positive subsonic flow, $S_C > 0$, and $\boldsymbol{F}_R^{HLLC}$ for negative subsonic flow, $S_C \leq 0$, are unknown. In order to determine the fluxes, Rankine-Hugoniot (RH) relations are used across the three waves associated with wave speeds S_L, S_C, and S_R. The Rankine-Hugoniot relation states that across a wave

$$\Delta \boldsymbol{F} = S \Delta \boldsymbol{U}, \tag{3.17}$$

where S is the speed of the wave, as mentioned in Section 2.2. For the wave associated with the wave speed S_L, the RH relation gives

$$\boldsymbol{F}_L^{HLLC} - \boldsymbol{F}_L = S_L(\boldsymbol{U}_L^{HLLC} - \boldsymbol{U}_L). \tag{3.18}$$

For the contact discontinuity, the RH relation is

$$\boldsymbol{F}_R^{HLLC} - \boldsymbol{F}_L^{HLLC} = S_R(\boldsymbol{U}_R^{HLLC} - \boldsymbol{U}_L^{HLLC}). \tag{3.19}$$

and for the wave associated with the wave speed S_R, the RH relation gives

$$\boldsymbol{F}_R - \boldsymbol{F}_R^{HLLC} = S_R(\boldsymbol{U}_R - \boldsymbol{U}_R^{HLLC}). \tag{3.20}$$

Manipulation of these equations gives *exactly the consistency condition* (3.10), so they are sufficient to ensure consistency.

We now have three equations for the four unknowns, $\boldsymbol{U}_L^{HLLC}$, $\boldsymbol{U}_R^{HLLC}$, $\boldsymbol{F}_L^{HLLC}$ and $\boldsymbol{F}_R^{HLLC}$. In order to close the system, more information is needed. Here, the Riemann invariants across the contact discontinuity are used.

$$\left.\begin{aligned} u_R^{HLLC} &= u_L^{HLLC} = S_C \\ p_R^{HLLC} &= p_L^{HLLC} \end{aligned}\right\} \tag{3.21}$$

We now manipulate the RH conditions and enforce the Riemann invariants to obtain $\boldsymbol{U}_L^{\text{HLLC}}$ and $\boldsymbol{U}_R^{\text{HLLC}}$.

The first component in Equation (3.18) is

$$S_C\rho_L^{HLLC} - u_L\rho_L = S_L(\rho_L^{HLLC} - \rho_L), \tag{3.22}$$

where it is enforced that $u_L^{HLLC} = S_C$. This gives that

$$\rho_L^{HLLC} = \rho_L \frac{S_L - u_L}{S_L - S_C}. \tag{3.23}$$

The second component in Equation (3.18) is

$$\rho_L^{HLLC} S_C^2 + p_L^{HLLC} - (\rho_L u_L^2 + p_L) = S_L(\rho_L^{HLLC} S_C - \rho_L u_L). \tag{3.24}$$

Inserting Equation (3.23) into (3.24) and solving for p_L^{HLLC} gives

$$\begin{aligned} p_L^{HLLC} &= \rho_L(S_L - u_L)S_C + \rho_L u_L(u_L - S_L) + p_L \\ &= p_L + \rho_L(S_L - u_L)(S_C - u_L). \end{aligned} \tag{3.25}$$

Equivalently, for the RH condition across the right wave, one finds from the first component of Equation (3.20) that

$$\rho_R^{HLLC} = \rho_R \frac{S_R - u_R}{S_R - S_C}., \tag{3.26}$$

where it is enforced that $u_R^{HLLC} = S_C$ and from the second component, using relation (3.26) that

$$p_R^{HLLC} = p_R + \rho_R(S_R - u_R)(S_C - u_R). \tag{3.27}$$

S_C is still unknown, but can be found by enforcing $p_L^{HLLC} = p_R^{HLLC}$

$$p_L + \rho_L(S_L - u_L)(S_C - u_L) = p_R + \rho_R(S_R - u_R)(S_C - u_R). \tag{3.28}$$

Solving this gives that

$$S_C = \frac{p_R - p_L + \rho_L u_L(S_L - u_L) - \rho_R u_R(S_R - u_R)}{\rho_L(S_L - u_L) - \rho_R(S_R - u_R)}. \tag{3.29}$$

The first and second components of $\boldsymbol{U}_K^{HLLC}$, $K = L, R$ are now known. The third component is found by manipulating the third component of Equation (3.18) for $\boldsymbol{U}_L^{HLLC}$ and (3.20) for $\boldsymbol{U}_R^{HLLC}$. For $\boldsymbol{U}_L^{HLLC}$,

$$S_C(E_L^{HLLC} + p_L^{HLLC}) - u_L(E_L + p_L) = S_L(E_L^{HLLC} - E_L). \tag{3.30}$$

Solving for E_L^{HLLC} and inserting the relations found above for ρ_L^{HLLC} and p_L^{HLLC} gives that

$$E_L^{HLLC} = \rho_L \left(\frac{S_L - u_L}{S_L - S_C} \right) \left(\frac{E_L}{\rho_L} + (S_C - u_L) \left(S_C + \frac{p_L}{\rho_L (S_L - u_L)} \right) \right). \tag{3.31}$$

Once again, the result is equivalent for the third component of Equation (3.20). This finally gives the intermediate state fluxes $\boldsymbol{F}_K^{HLLC}$, $K = L, R$ as

$$\boldsymbol{F}_K^{HLLC} = \boldsymbol{F}_K + S_K (\boldsymbol{U}_K^{HLLC} - \boldsymbol{U}_K), \tag{3.32}$$

where the intermediate states are approximated by

$$\boldsymbol{U}_K^{HLLC} = \rho_K \left(\frac{S_K - u_K}{S_K - S_C} \right) \begin{pmatrix} 1 \\ S_C \\ \frac{E_K}{\rho_K} + (S_C - u_K) \left(S_C + \frac{p_K}{\rho_K (S_K - u_K)} \right) \end{pmatrix}, \ K = R, L. \tag{3.33}$$

3.1.4. HLLC+S for the Euler equations with area change

Though the derivation of the HLLC method was conducted for the Euler equations, this scheme can also be used for the Euler equations with area change. Then, $\boldsymbol{U}_K^{HLLC}$, $K = L, R$ must be multiplied by the area A_K. Otherwise, the expressions for the HLLC scheme stay the same. The FVM (3.3),

$$\boldsymbol{U}_j^{n+1} = \boldsymbol{U}_j^n - \frac{\Delta t}{\Delta x} \left(\boldsymbol{\mathcal{F}}_{j+1/2} - \boldsymbol{\mathcal{F}}_{j-1/2} \right) + \Delta t \widetilde{\boldsymbol{S}}_j,$$

can be used with the HLLC numerical flux function for the Euler equations with area change. This FVM requires a representation of the source term, $\widetilde{\boldsymbol{S}}_j$. The discretization of this term requires special care to ensure numerical stability. Brown et al [31] use the following discretization

$$\widetilde{\boldsymbol{S}}_j = \frac{p_j}{\Delta x} \begin{pmatrix} 0 \\ \Delta_j A \\ 0 \\ 0 \end{pmatrix}, \tag{3.34}$$

and

$$\Delta_j A = A_{j,j+1/2} - A_{j,j-1/2} \tag{3.35}$$

where “the areas at the interfaces are taken from within the cell” [31]. It is unclear what this means as the area *within* one cell is constant which implies that $\Delta_j A = A_j - A_j = 0$.

In the present study, the following, very simple discretization is used: if the flow is in the positive direction ($u_j > 0$),

$$\widetilde{\boldsymbol{S}}_{j-1/2} = \frac{p_j}{\Delta x} \begin{pmatrix} 0 \\ A_j - A_{j-1} \\ 0 \\ 0 \end{pmatrix}, \tag{3.36}$$

and if the flow is zero or in the negative direction ($u_j \leq 0$)

$$\widetilde{\boldsymbol{S}}_j = \frac{p_j}{\Delta x} \begin{pmatrix} 0 \\ A_{j+1} - A_j \\ 0 \\ 0 \end{pmatrix}. \tag{3.37}$$

The non-disturbance relation discussed by Liou et al. [41] holds for this discretization, i.e. under steady conditions with $u = 0$ and $p = const$:

$$\frac{\partial (Ap)}{\partial x} = p \frac{\partial A}{\partial x}. \tag{3.38}$$

As will be presented in Chapter 4, this discretization works for many test cases, but it tends to overestimate the source term and is not well-balanced. It is therefore of interest to develop an augmented version of HLLC which includes the stationary wave in a more robust manner. This has not been done before and has been a main focus of this work.

3.1.5. Integral relations for the Euler equations with area change

We now wish to derive an HLLC-like method to solve the cell interface Riemann problem

$$\boldsymbol{U}(x,0) = \begin{cases} \boldsymbol{U}_L, & \text{if } x < 0, \\ \boldsymbol{U}_R, & \text{if } x \geq 0. \end{cases} \tag{3.39}$$

for

$$\boldsymbol{U}_t + \boldsymbol{F}(\boldsymbol{U})_x = \boldsymbol{S}, \tag{3.40}$$

where

$$\boldsymbol{U} = \begin{pmatrix} \rho A \\ \rho u A \\ EA \\ A \end{pmatrix}, \; \boldsymbol{F}(\boldsymbol{U}) = \begin{pmatrix} \rho u A \\ (\rho u^2 + p)A \\ (E + p)uA \\ 0 \end{pmatrix}, \boldsymbol{S} = \begin{pmatrix} 0 \\ p\frac{\partial A}{\partial x} \\ 0 \\ 0 \end{pmatrix}.$$

Once again a consistency condition is derived in a similar manner as for HLLC, however now the source term must be included in the calculations. Murillo and García-Navarro [26] have made an augmented version of HLLC, which they call "HLLCS" for the shallow-water equations including source terms. The derivation of integral relations for the Euler equations with area change is entirely equivalent to their derivation for the shallow water equations.

The system of equations (3.40) is integrated over the control volume depicted in Figure 3.3,

$$\int_{x_L}^{x_R} \int_0^{\Delta t} \left(\frac{\partial \boldsymbol{U}}{\partial t} + \frac{\partial \boldsymbol{F}}{\partial x} - \boldsymbol{S} \right) \mathrm{d}t \; \mathrm{d}x = 0. \tag{3.41}$$

This gives the following consistency condition

$$\int_{x_L}^{x_R} \boldsymbol{U}(x,\Delta t)\,\mathrm{d}x = (x_R\boldsymbol{U}_R - x_L\boldsymbol{U}_L) - (\boldsymbol{F}_R - \boldsymbol{F}_L)\Delta t + \int_{x_L}^{x_R}\int_0^{\Delta t} \boldsymbol{S}\,\mathrm{d}t\,\mathrm{d}x. \tag{3.42}$$

We further follow the approach of Murillo and García-Navarro [26] by introducing the time averaged source term $\overline{\boldsymbol{S}}$, where

$$\overline{\boldsymbol{S}} = \frac{1}{\Delta t}\int_{x_L}^{x_R}\int_0^{\Delta t} \boldsymbol{S}\,\mathrm{d}t\,\mathrm{d}x. \tag{3.43}$$

such that the consistency condition becomes

$$\int_{x_L}^{x_R} \boldsymbol{U}(x,\Delta t)\,\mathrm{d}x = (x_R\boldsymbol{U}_R - x_L\boldsymbol{U}_{\boldsymbol{L}}) - (\boldsymbol{F}_R - \boldsymbol{F}_L - \overline{\boldsymbol{S}})\Delta t. \tag{3.44}$$

Two different estimates of $\overline{\boldsymbol{S}}$ are used in this work and they are presented in Subsection 3.1.8. The integral average over the intermediate states between S_L and S_R at time Δt must be

$$\frac{1}{\Delta t(S_R - S_L)}\int_{\Delta t S_L}^{\Delta t S_R} \boldsymbol{U}(x,\Delta t)\,\mathrm{d}x = \frac{S_R\boldsymbol{U}_R - S_L\boldsymbol{U}_L - (\boldsymbol{F}_R - \boldsymbol{F}_L) + \overline{\boldsymbol{S}}}{S_R - S_L} \tag{3.45}$$

in order to satisfy the consistency condition (3.44).

3.1.6. Augmented version of HLLC, HLLCS, for the Euler equations with area change

We now derive an augmented version of HLLC for the Euler equations with area change which satisfies the integral relations derived in the previous section. Each type of flow (supersonic from the right and left, and subsonic from the right and left) is assessed in order to find the full solver. The simplest cases are for supersonic flow. This is shown first. The full method is presented in section 3.1.7.

Supersonic flow

If either $S_L > 0$ or $S_R < 0$ we have supersonic flow. A sketch of a control volume in $x-t$ space which contains the wave structure of a Riemann problem with positive supersonic flow ($S_L > 0$) is shown in Figure 3.5. In this case, the flux just to the left of the interface, $x = 0$, is simply $\boldsymbol{F}_L$, giving

$$\boldsymbol{F}_{j+1/2}^{\text{HLLCS}-} = \boldsymbol{F}_L. \tag{3.46}$$

The flow just to the right of the interface has passed the source such that

$$\boldsymbol{F}_{j+1/2}^{\text{HLLCS}+} = \boldsymbol{F}_L + \overline{\boldsymbol{S}}. \tag{3.47}$$

Similarly for negative supersonic flow, $S_R < 0$, the numerical fluxes at Δt become:

$$\boldsymbol{F}_{j+1/2}^{\text{HLLCS}-} = \boldsymbol{F}_R - \overline{\boldsymbol{S}} \tag{3.48}$$

$$\boldsymbol{F}_{j+1/2}^{\text{HLLCS}+} = \boldsymbol{F}_R. \tag{3.49}$$

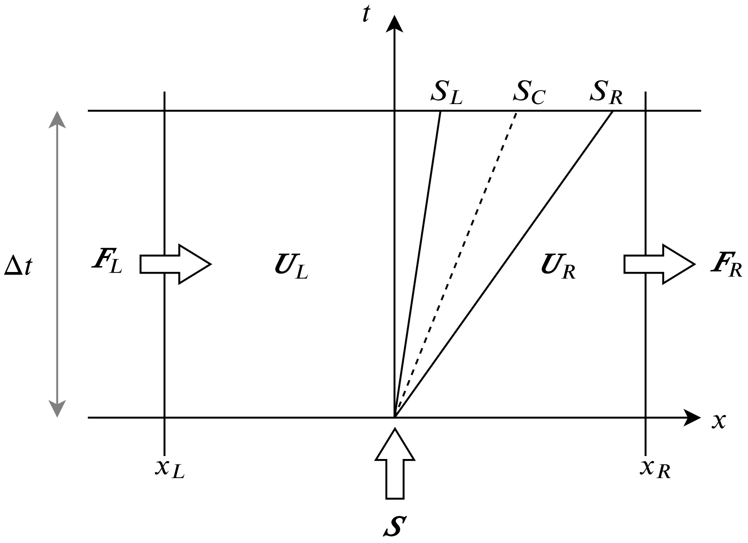

Figure 3.5.: Control volume in the $x - t$ plane containing the solution to the Riemann problem for supersonic flow from left to right.

Positive subsonic flow

The derivation for subsonic flow is more complicated. Two cases may arise, positive subsonic flow, $S_C > 0$ and negative subsonic flow, $S_C < 0$. The full derivation for $S_C > 0$ is shown below.

An illustration of a control volume containing the wave structure of a Riemann problem for positive subsonic flow is shown in Figure 3.6. In this case there are three unknown intermediate states separated by the stationary wave at $x = 0$ and the contact discontinuity, $\boldsymbol{U}_L^-$, $\boldsymbol{U}_R^+$ and $\boldsymbol{U}_R^{++}$. We approximate the intermediate states, $\boldsymbol{U}_L^-$, $\boldsymbol{U}_R^+$ and $\boldsymbol{U}_R^{++}$ by

$$\left.\begin{aligned} \boldsymbol{U}_L^- &= \frac{1}{-\Delta t S_L} \int_{\Delta t S_L}^{0} \boldsymbol{U}(x, \Delta t)\,\mathrm{d}x \\ \boldsymbol{U}_R^+ &= \frac{1}{\Delta t S_C} \int_{0}^{\Delta t S_C} \boldsymbol{U}(x, \Delta t)\,\mathrm{d}x \\ \boldsymbol{U}_R^{++} &= \frac{1}{\Delta t (S_R - S_C)} \int_{\Delta t S_C}^{\Delta t S_R} \boldsymbol{U}(x, \Delta t)\,\mathrm{d}x \end{aligned}\right\} . \tag{3.50}$$

In order to fulfill the consistency condition (3.44), we need that

$$\frac{-S_L \boldsymbol{U}_L^- + S_C \boldsymbol{U}_R^+ + (S_R - S_C)\boldsymbol{U}_R^{++}}{S_R - S_L} = \frac{S_R \boldsymbol{U}_R - S_L \boldsymbol{U}_L - (\boldsymbol{F}_R - \boldsymbol{F}_L) + \overline{\boldsymbol{S}}}{S_R - S_L}. \tag{3.51}$$

In order to estimate the intermediate fluxes, the Rankine-Hugoniot (RH) condition is applied across all the waves in the problem. The RH relations are

$$\boldsymbol{F}_L^- - \boldsymbol{F}_L = S_L(\boldsymbol{U}_L^- - \boldsymbol{U}_L), \tag{3.52}$$

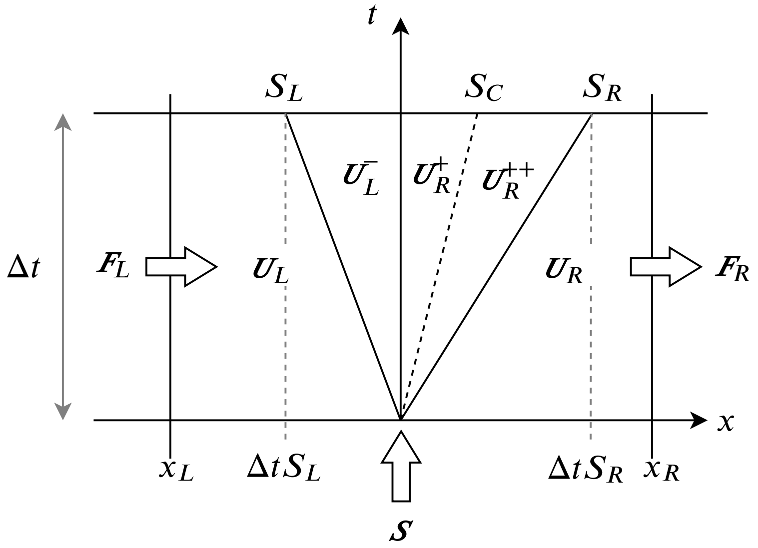

Figure 3.6.: Integration control volume $[x_L, x_R] \times [0, \Delta t]$ in the $x - t$ plane. The control volume contains the two fastest signal velocities, S_L and S_R from the Riemann problem. The solution consists of three inner states separated by the stationary wave at $x = 0$ and the contact discontinuity of positive speed, S_C.

$$\boldsymbol{F}_R^+ - \boldsymbol{F}_L^- - \overline{\boldsymbol{S}} = S(\boldsymbol{U}_R^+ - \boldsymbol{U}_L^-) = 0, \tag{3.53}$$

$$\boldsymbol{F}_R^{++} - \boldsymbol{F}_R^+ = S_C(\boldsymbol{U}_R^{++} - \boldsymbol{U}_R^+), \tag{3.54}$$

and

$$\boldsymbol{F}_R - \boldsymbol{F}_R^{++} = S_R(\boldsymbol{U}_R - \boldsymbol{U}_R^{++}). \tag{3.55}$$

Once again, the RH relations (3.52)-(3.55) are enough to ensure consistency. If we substitute $\boldsymbol{F}_R^{++}$ from Equation (3.55) into Equation (3.54)

$$\boldsymbol{F}_R - S_R(\boldsymbol{U}_R - \boldsymbol{U}_R^{++}) - \boldsymbol{F}_R^+ = S_C(\boldsymbol{U}_R^{++} - \boldsymbol{U}_R^+) \tag{3.56}$$

and further substitute $\boldsymbol{F}_R^+$ from Equation (3.56) and $\boldsymbol{F}_L^-$ from Equation (3.52) into (3.53), we get the following relation:

$$\boldsymbol{F}_R - S_R(\boldsymbol{U}_R - \boldsymbol{U}_R^{++}) - S_C(\boldsymbol{U}_R^{++} - \boldsymbol{U}_R^+) - \big(\boldsymbol{F}_L + S_L(\boldsymbol{U}_L^- - \boldsymbol{U}_L)\big) - \overline{\boldsymbol{S}} = 0. \tag{3.57}$$

Moving the known states and the source term to the right hand side gives exactly the consistency condition (3.44). (3.52)-(3.55) are four equations for the six unknowns, $\boldsymbol{U}_L^-$, $\boldsymbol{U}_R^+$, $\boldsymbol{U}_R^{++}$, $\boldsymbol{F}_L^-$, $\boldsymbol{F}_R^+$ and $\boldsymbol{F}_R^{++}$. Thus we need to impose some other conditions in addition to these to close the system. Here, our approach differs from Murillo and García-Navarro [26] as we are working with a different system of equations.

Full derivation of nonlinear system for positive subsonic flow

For positive subsonic flow, we present a full derivation of the nonlinear system which must be solved to find the unknown intermediate fluxes $\boldsymbol{F}_L^-$, $\boldsymbol{F}_R^+$ and $\boldsymbol{F}_R^{++}$. An augmented version of HLLC for the Baer-Nunziato equations has been derived by Tokareva and Toro [25]. As explained in Subsection 2.3.3, the Baer-Nunziato equations have similarities to the Euler equations with area change. Our approach therefore follows to some extent Tokareva and Toro's approach in deriving HLLCS for the Baer-Nunziato equations.

The following conditions that are satisfied by the exact solution of the Euler equations with area change are imposed. Across the contact discontinuity the Riemann invariants should hold,

$$\left.\begin{array}{l} u_R^{++} = u_R^+ = S_C \\ p_R^{++} = p_R^+ \end{array}\right\}, \tag{3.58}$$

and across the 0-wave the Riemann invariants should hold,

$$\left.\begin{array}{l} (A\rho u)_L^- = (A\rho u)_R^+ \\ s_L^- = s_R^+ \\ (\frac{u^2}{2} + h)_L^- = (\frac{u^2}{2} + h)_R^+ \end{array}\right\}. \tag{3.59}$$

Similarly to HLLC for the Euler equations, the RH condition across the wave associated with the wave speed S_L gives

$$\rho_L^- = \rho_L \frac{S_L - u_L}{S_L - u_L^-}, \tag{3.60}$$

$$p_L^- = p_L + \rho_L(S_L - u_L)(u_L^- - u_L), \tag{3.61}$$

$$E_L^- = \rho_L \left(\frac{S_L - u_L}{S_L - u_L^-}\right) \left(\frac{E_L}{\rho_L} + (u_L^- - u_L)\left(u_L^- + \frac{p_L}{\rho_L(S_L - u_L)}\right)\right), \tag{3.62}$$

and the RH condition across the wave associated with the wave speed S_R gives

$$\rho_R^{++} = \rho_R \frac{S_R - u_R}{S_R - u_R^{++}}, \tag{3.63}$$

$$p_R^{++} = p_R + \rho_R(S_R - u_R)(u_R^{++} - u_R), \tag{3.64}$$

$$E_R^{++} = \rho_R \left(\frac{S_R - u_R}{S_R - u_R^{++}}\right) \left(\frac{E_R}{\rho_R} + (u_R^{++} - u_R)\left(u_R^{++} + \frac{p_R}{\rho_R(S_R - u_R)}\right)\right). \tag{3.65}$$

Equations (3.60)-(3.62)and (3.26)-(3.65) together with the Riemann invariants constitute a nonlinear system which can be solved iteratively. Tokareva and Toro have a similar, but larger system of equations which must be solved. Both for the Euler equations with area change and the Baer-Nunziato equations, either the pressures p_L^-, $p_R^+ = p_R^{++}$ or the velocities u_L^-, $u_R^+ = u_R^{++}$ can be chosen as independent variables to solve the system.

As Tokareva and Toro state in [25], there is no difference between these two approaches from a theoretical point of view as the two representations of the system are mathematically equivalent. However, they point out that in practice, the iterations in terms of pressures is more robust for severe test problems with very low pressures or densities. Iteration in terms of velocities fail to compute such test cases, as there is no mechanism to control pressure positivity [25]. In light of this observation, we choose p_L^- and p_R^+ as the independent variables.

We now use equation 3.61 to express the speed u_L^- as a function of p_L^-

$$u_L^-(p_L^-) = u_L + \frac{p_L^- - p_L}{\rho_L(S_L - u_L)}, \tag{3.66}$$

such that $\rho_L^- = \rho_L^-(p_L^-)$ and $E_L^- = E_L^-(p_L^-)$. If p_L^- is known, the state $\boldsymbol{U}_L^-$ is fully determined.

Similarly, we use Equation (3.64) to express the speed u_R^{++} as a function of the pressure $p_R^+ = p_R^{++}$

$$u_R^{++}(p_R^+) = u_R + \frac{p_R^+ - p_R}{\rho_R(S_R - u_R)},. \tag{3.67}$$

Enforcing the Riemann invariant $u_R^+ = u_R^{++} = S_C$, we get that

$$u_R^+(p_R^+) = u_R^{++}(p_R^+) = u_R + \frac{p_R^+ - p_R}{\rho_R(S_R - u_R)}, \tag{3.68}$$

such that $\rho_R^{++} = \rho_R^{++}(p_R^+)$ and $E_R^{++} = E_R^+(p_R^+)$.

From the relations across the 0-wave, we know that

$$s_L^- = s_R^+ = s. \tag{3.69}$$

The state $\boldsymbol{U}_L^-$ is determined by the pressure p_L^-, so $s_L^- = s_L^-(p_L^-)$ such that

$$s = s(p_L^-). \tag{3.70}$$

$s_R^+ = s$ is thus known, and the state $\boldsymbol{U}_R^+$ is determined by p_R^+, s_R^+. The density ρ_R^+ and the enthalpy h_R^+ can then be computed using the equation of state.

The relation for mass flux then gives the following equation

$$A_L \rho_L^-(p_L^-) u_L^-(p_L^-) - A_R \rho_R^+\left(p_R^+, s(p_L^-)\right) u_R^+(p_R^+) = 0. \tag{3.71}$$

Furthermore, the relation for total enthalpy,

$$\frac{(u_L^-)^2}{2} + h_L^- = \frac{(u_R^+)^2}{2} + h_R^+ \tag{3.72}$$

gives the following equation

$$h_R^+\left(p_R^+, s(p_L^-)\right) + \frac{1}{2}\left(u_R^+(p_R^+)\right)^2 - \left[h_L^-\left(p_L^-, s(p_L^-)\right) + \frac{1}{2}\left(u_L^-(p_L^-)\right)^2\right] = 0. \tag{3.73}$$

Equations (3.71) and (3.73) are two equations for our two unknown parameter pressures p_L^- and p_R^+. This set of equations can be solved iteratively by Newton-Raphson's method.

$$\boldsymbol{p}_{k+1} = \boldsymbol{p}_k - d\boldsymbol{f}^{-1}\boldsymbol{f}, \tag{3.74}$$

where

$$\boldsymbol{p} = \begin{pmatrix} p_L^- \\ p_R^+ \end{pmatrix}, \tag{3.75}$$

$$\boldsymbol{f} = \begin{pmatrix} A_L \rho_L^-(p_L^-) u_L^-(p_L^-) - A_R \rho_R^+\left(p_R^+, s(p_L^-)\right) u_R^+(p_R^+) \\ h_R^+\left(p_R^+, s(p_L^-)\right) + \frac{1}{2}\left(u_R^+(p_R^+)\right)^2 - \left[h_L^-\left(p_L^-, s(p_L^-)\right) + \frac{1}{2}\left(u_L^-(p_L^-)\right)^2\right] \end{pmatrix}, \tag{3.76}$$

and

$$d\boldsymbol{f} = \begin{pmatrix} \dfrac{\partial \boldsymbol{f}_1}{\partial p_L^-} & \dfrac{\partial \boldsymbol{f}_1}{\partial p_R^+} \\ \dfrac{\partial \boldsymbol{f}_2}{\partial p_L^-} & \dfrac{\partial \boldsymbol{f}_2}{\partial p_R^+} \end{pmatrix}. \tag{3.77}$$

A full derivation of the Jacobian matrix, $d\boldsymbol{f}$ can be found in Appendix E. The inverse of the Jacobian is

$$d\boldsymbol{f}^{-1} = \frac{1}{\dfrac{\partial \boldsymbol{f}_2}{\partial p_R^+}\dfrac{\partial \boldsymbol{f}_1}{\partial p_L^-} - \dfrac{\partial \boldsymbol{f}_1}{\partial p_R^+}\dfrac{\partial \boldsymbol{f}_2}{\partial p_L^-}} \begin{pmatrix} \dfrac{\partial \boldsymbol{f}_2}{\partial p_R^+} & -\dfrac{\partial \boldsymbol{f}_1}{\partial p_R^+} \\ -\dfrac{\partial \boldsymbol{f}_2}{\partial p_L^-} & \dfrac{\partial \boldsymbol{f}_1}{\partial p_L^-} \end{pmatrix}. \tag{3.78}$$

In order to find an initial guess for the parameter pressures p_L^-, p_R^+ an approximate Riemann solver for the Euler equations without area change is used. Toro provides a FORTRAN code for this solver in Section 4.9 of his book, page 156 [35]. The solver outputs an estimate of the intermediate state pressure p^* which is used as the initial guess for the pressures,

$$(p_L^-)_0 = p^*, \tag{3.79}$$

$$(p_R^+)_0 = p^*. \tag{3.80}$$

Once p_L^- and p_R^+ are found, the state $\boldsymbol{U}_L^-$ can be calculated using Equations (3.66), (3.60) and (3.62). With this we can finally find the unknown fluxes $\boldsymbol{F}_L^-$ and $\boldsymbol{F}_R^+$. We have from Equation (3.52) that

$$\boldsymbol{F}_L^- = \boldsymbol{F}_L + S_L(\boldsymbol{U}_L^- - \boldsymbol{U}_L) \tag{3.81}$$

and from Equation (3.53) that

$$\boldsymbol{F}_R^+ = \boldsymbol{F}_L^- + \overline{\boldsymbol{S}}. \tag{3.82}$$

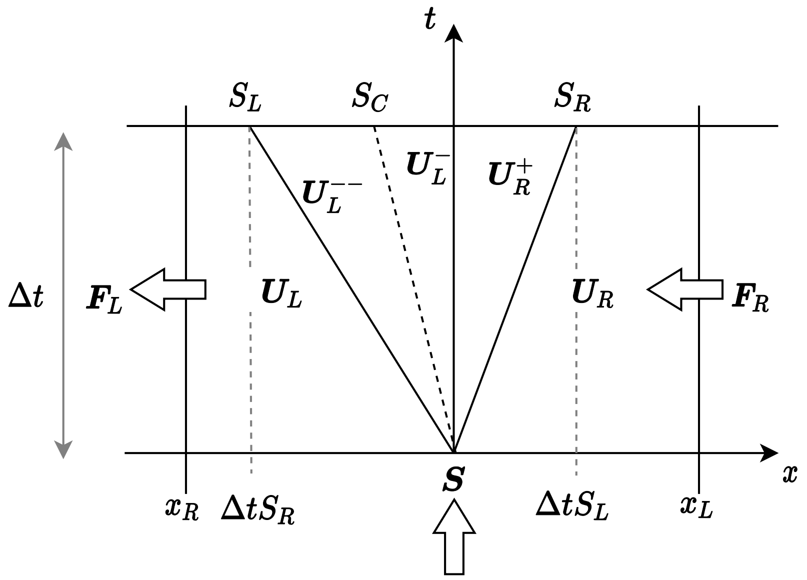

Figure 3.7.: Integration control volume $[x_L, x_R] \times [0, \Delta t]$ in the $x - t$ plane. The control volume contains the two fastest signal velocities S_L, S_R from the Riemann problem. The solution consists of three inner states separated by the stationary wave at $x = 0$ and the contact discontinuity of negative speed, S_C.

Negative subsonic flow

For negative subsonic flow, we now have the states $\boldsymbol{U}_L^{--}$, $\boldsymbol{U}_L^{-}$ and $\boldsymbol{U}_R^{+}$ as illustrated in Figure 3.7. The states are defined in the following way

$$\left.\begin{aligned} \boldsymbol{U}_L^{--} &= \frac{1}{-\Delta t(S_L - S_C)} \int_{\Delta t S_L}^{\Delta t S_C} \boldsymbol{U}(x, \Delta t)\,\mathrm{d}x \\ \boldsymbol{U}_L^{-} &= \frac{1}{-\Delta t S_C} \int_{\Delta t S_C}^{0} \boldsymbol{U}(x, \Delta t)\,\mathrm{d}x \\ \boldsymbol{U}_R^{+} &= \frac{1}{\Delta t(S_R)} \int_{0}^{\Delta t S_R} \boldsymbol{U}(x, \Delta t)\,\mathrm{d}x \end{aligned}\right\}. \tag{3.83}$$

and the integral average across the intermediate states,

$$\int_{\Delta t S_L}^{\Delta t S_R} \boldsymbol{U}(x, \Delta t)\,\mathrm{d}x = -\Delta t(S_L - S_C)\boldsymbol{U}_L^{--} - \Delta t S_C \boldsymbol{U}_L^{-} + \Delta t S_R \boldsymbol{U}_R^{+} \tag{3.84}$$

must satisfy the consistency condition (3.44).

Once again RH relations across the four waves are used to estimate the intermediate fluxes, $\boldsymbol{F}_L^{--}$, $\boldsymbol{F}_L^{-}$ and $\boldsymbol{F}_R^{+}$. The relations are

$$\boldsymbol{F}_L^{--} - \boldsymbol{F}_L = S_L(\boldsymbol{U}_L^{--} - \boldsymbol{U}_L), \tag{3.85}$$

$$\boldsymbol{F}_L^- - \boldsymbol{F}_L^{--} = S_C(\boldsymbol{U}_L^- - \boldsymbol{U}_L^{--}), \tag{3.86}$$

$$\boldsymbol{F}_R^+ - \boldsymbol{F}_L^- - \overline{\boldsymbol{S}} = 0. \tag{3.87}$$

and

$$\boldsymbol{F}_R - \boldsymbol{F}_R^+ = S_R(\boldsymbol{U}_R - \boldsymbol{U}_R^+). \tag{3.88}$$

It can be shown that these relations satisfy the consistency condition. The following conditions are imposed in addition to the relations above: across the contact discontinuity

$$\left.\begin{aligned} u_L^{--} &= u_L^- = S_C \\ p_L^{--} &= p_L^- \end{aligned}\right\}, \tag{3.89}$$

and across the stationary wave

$$\left.\begin{aligned} &(A\rho u)_L^- = (A\rho u)_R^+ \\ &s_L^- = s_R^+ \\ &(\tfrac{u^2}{2} + h)_L^- = (\tfrac{u^2}{2} + h)_R^+ \end{aligned}\right\}. \tag{3.90}$$

Manipulation of the RH conditions (3.85) and (3.88) in addition to enforcing the relations above give an analogous system of equations as the system for positive subsonic flow, (3.76).

$$\boldsymbol{g} = \begin{pmatrix} A_L\rho_L^-\left(p_L^-, s(p_R^+)\right)u_L^-(p_L^-) - A_R\rho_R^+\left(p_R^+\right)u_R^+(p_R^+) \\ h_R^+\left(p_R^+, s(p_R^+)\right) + \frac{1}{2}\left(u_R^+(p_R^+)\right)^2 - \left[h_L^-\left(p_L^-, s(p_R^+)\right) + \frac{1}{2}\left(u_L^-(p_L^-)\right)^2\right] \end{pmatrix} \tag{3.91}$$

This can once again be solved iteratively. We now have the state $\boldsymbol{U}_L^{--}$ instead of $\boldsymbol{U}_R^{++}$ as for positive subsonic flow, however, the equations are analogous because they are simply mirror images. One can technically “flip” the left and right states from the positive subsonic flow case,

$$\boldsymbol{U}_L^- \to \boldsymbol{U}_R^+, \tag{3.92}$$

$$\boldsymbol{U}_R^+ \to \boldsymbol{U}_L^-, \tag{3.93}$$

$$\boldsymbol{U}_R^{++} \to \boldsymbol{U}_L^{--}, \tag{3.94}$$

solve the nonlinear equations defined for this system, (3.76), and obtain the solution for negative subsonic flow.

Once $\boldsymbol{U}_R^+$ is calculated, $\boldsymbol{F}_R^+$ can be found by Equation (3.88)

$$\boldsymbol{F}_R^+ = \boldsymbol{F}_R - S_R(\boldsymbol{U}_R - \boldsymbol{U}_R^+), \tag{3.95}$$

and $\boldsymbol{F}_L^-$ can be found from Equation (3.87)

$$\boldsymbol{F}_L^- = \boldsymbol{F}_R^+ - \overline{\boldsymbol{S}}. \tag{3.96}$$

3.1.7. The full HLLCS solver

The HLLCS method for the Euler equations with area change approximates the flux functions $\boldsymbol{\mathcal{F}}^-_{j+1/2}$ and $\boldsymbol{\mathcal{F}}^+_{j-1/2}$ in the FVM (3.4)

$$\boldsymbol{U}_j^{n+1} = \boldsymbol{U}_j^n - \frac{\Delta t}{\Delta x}\left(\boldsymbol{\mathcal{F}}^-_{j+1/2} - \boldsymbol{\mathcal{F}}^+_{j-1/2}\right)$$

as

$$\boldsymbol{\mathcal{F}}^-_{j+1/2} = \begin{cases} \boldsymbol{F}_L, & \text{if } 0 < S_L, \\ \boldsymbol{F}_L^-, & \text{if } S_L \leq 0 < S_C, \\ \boldsymbol{F}_R^+ - \overline{\boldsymbol{S}}, & \text{if } S_C \leq 0 < S_R, \\ \boldsymbol{F}_R - \overline{\boldsymbol{S}}, & \text{if } 0 \geq S_R. \end{cases} . \tag{3.97}$$

and

$$\boldsymbol{\mathcal{F}}^+_{j+1/2} = \begin{cases} \boldsymbol{F}_L + \overline{\boldsymbol{S}}, & \text{if } 0 < S_L, \\ \boldsymbol{F}_L^- + \overline{\boldsymbol{S}}, & \text{if } S_L \leq 0 < S_C, \\ \boldsymbol{F}_R^+, & \text{if } S_C \leq 0 < S_R, \\ \boldsymbol{F}_R, & \text{if } 0 \geq S_R. \end{cases} \tag{3.98}$$

where S_C approximates the speed of the contact discontinuity and S_L and S_R are approximations of the smallest and largest wave speeds at the interface $x_{j+1/2}$.

For subsonic flow, HLLCS approximates the cell interface Riemann problem by a four-wave solution;

$$\widetilde{\boldsymbol{U}}(x/t) = \begin{cases} \boldsymbol{U}_L, & \text{if } x < S_L t, \\ \begin{cases} \boldsymbol{U}_L^{--}, & \text{if } S_L t \leq x < S_C t, \\ \boldsymbol{U}_L^-, & \text{if } S_C t \leq x < 0, \\ \boldsymbol{U}_R^+, & \text{if } 0 \leq x < S_R t, \end{cases} & \text{if } S_C t \leq 0 \\ \begin{cases} \boldsymbol{U}_L^-, & \text{if } S_L t \leq x < 0, \\ \boldsymbol{U}_R^+, & \text{if } 0 \leq x < S_C t, \\ \boldsymbol{U}_R^{++}, & \text{if } S_C t \leq x < S_R t, \end{cases} & \text{if } S_C t > 0 \\ \boldsymbol{U}_R, & \text{if } x \geq S_R t, \end{cases} \tag{3.99}$$

as sketched in Figure 3.8. The intermediate states $\boldsymbol{U}_L^-$, $\boldsymbol{U}_R^+$, $\boldsymbol{U}_R^{++}$ for positive subsonic flow or $\boldsymbol{U}_L^{--}$, $\boldsymbol{U}_L^-$, $\boldsymbol{U}_R^+$ for negative subsonic flow are found by solving the system of equations (3.76) for positive subsonic flow or (3.91) for negative subsonic flow iteratively using the Newton-Rhapson's method. S_C is solved for in the iterative Newton solver. For each Newton step, the sign of S_C is checked such that the correct equations are used in the solver, (3.76) if $S_C \geq 0$ and (3.91) if $S_C < 0$. A full algorithm for the HLLCS solver is given below:

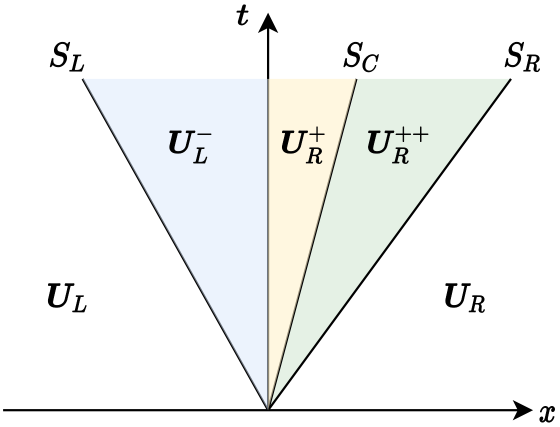

Figure 3.8.: HLLCS assumes a four-wave solution, giving three intermediate states, separated by the stationary wave at the cell interface and the contact wave.

Algorithm 1: The HLLCS solver. If subsonic flow is identified, the Newton-Rhapson solver is called. The Newton-Rhapson solver checks at each step whether the equations for positive (3.76) or negative subsonic flow (3.91) should be solved and returns S_C and the intermediate states $\boldsymbol{U}_L^-$, $\boldsymbol{U}_R^+$ and $\boldsymbol{U}_L^{--}$ or $\boldsymbol{U}_R^{++}$.

```
Result: Fluxes for the HLLCS solver, $\boldsymbol{F}_R^+$ and $\boldsymbol{F}_L^-$.
if $S_L > 0$ then
    $\boldsymbol{F}_L^- = \boldsymbol{F}_L$
    $\boldsymbol{F}_R^+ = \boldsymbol{F}_L^- + \overline{\boldsymbol{S}}$
end
if $S_L \leq 0$ and $S_R > 0$ then
    call Newton-Rhapson solver, returning $S_C$ and intermediate states;
    if $S_C \geq 0$ then
        $\boldsymbol{F}_L^- = \boldsymbol{F}_L + S_L(\boldsymbol{U}_L^- - \boldsymbol{U}_L)$
        $\boldsymbol{F}_R^+ = \boldsymbol{F}_L^- + \overline{\boldsymbol{S}}$
    else
        $\boldsymbol{F}_R^+ = \boldsymbol{F}_R - S_R(\boldsymbol{U}_R - \boldsymbol{U}_R^+)$
        $\boldsymbol{F}_L^- = \boldsymbol{F}_R^+ - \overline{\boldsymbol{S}}$
    end
end
if $S_R \leq 0$ then
    $\boldsymbol{F}_R^+ = \boldsymbol{F}_R$
    $\boldsymbol{F}_L^- = \boldsymbol{F}_R^+ - \overline{\boldsymbol{S}}$
end
```

3.1.8. The source term for HLLCS

In this work, two source terms are tested for the HLLCS solver: the Roe average-based source term which is always applied for supersonic flow, but can also be applied for subsonic flow, and the flux-based source term which can only be applied for subsonic flow.

The Roe average-based source term

In general, the following approximate source term is applied in the HLLCS solver,

$$\overline{\boldsymbol{S}}_{\mathrm{RS}} = \begin{pmatrix} 0 \\ \hat{p}\,(A_R - A_L) \\ 0 \\ 0 \end{pmatrix}, \tag{3.100}$$

where $\hat{p}$ is the Roe-averaged pressure on the cell interface between the left and right states, $\boldsymbol{U}_L$ and $\boldsymbol{U}_R$. Details on the Roe average are given in Section 3.1.9. We therefore call this source term the Roe average-based source term (RS). RS is always applied for supersonic flow, and can also be applied for subsonic flow. However, for subsonic flow, the nonlinear system of equations determining the approximate intermediate states $\boldsymbol{U}_L^-$, $\boldsymbol{U}_R^+$ and either $\boldsymbol{U}_L^{--}$ or $\boldsymbol{U}_R^{++}$ is solved. The source term is then given implicitly by the Rankine-Hugoniot conditions.

The flux-based source term

For positive subsonic flow, the Rankine-Hugoniot conditions give that

$$\boldsymbol{F}_R^+ - \boldsymbol{F}_L^- = \overline{\boldsymbol{S}}, \tag{3.101}$$

$$\boldsymbol{F}_R^{++} = \boldsymbol{F}_R - S_R(\boldsymbol{U}_R - \boldsymbol{U}_R^{++}), \tag{3.102}$$

$$\boldsymbol{F}_R^+ = \boldsymbol{F}_R^{++} - S_C(\boldsymbol{U}_R^{++} - \boldsymbol{U}_R^+), \tag{3.103}$$

where $\boldsymbol{U}_L^-$, $\boldsymbol{U}_R^+$, $\boldsymbol{U}_R^{++}$ and $\boldsymbol{F}_L^-$ are known from the solution of the nonlinear system (3.76). Consequently, the source term must be

$$\overline{\boldsymbol{S}}_{\mathrm{FS+}} = \boldsymbol{F}_R^{++} - S_C(\boldsymbol{U}_R^{++} - \boldsymbol{U}_R^+) - \boldsymbol{F}_L^-. \tag{3.104}$$

Similarly for negative subsonic flow, we get that the source term must be

$$\overline{\boldsymbol{S}}_{\mathrm{FS\text{-}}} = \boldsymbol{F}_R^+ - \boldsymbol{F}_L^{--} + S_C(\boldsymbol{U}_L^- - \boldsymbol{U}_L^{--}), \tag{3.105}$$

where $\boldsymbol{U}_L^-$, $\boldsymbol{U}_L^{--}$, $\boldsymbol{F}_R^+$ and $\boldsymbol{F}_L^{--}$ are known from the solution of the nonlinear system (3.91). As the source term includes the approximate fluxes, we call it the flux-based source term (FS). Note however that FS needs a valid solution of the nonlinear system, (3.76) for positive subsonic flow or (3.91) for negative subsonic flow, otherwise the equations do not hold. If the flow is subsonic, but the Newton-Rhapson solver fails to converge for the system with a large error, FS should not be applied. We have not derived a similar FS estimate for supersonic flow.

3.1.9. Wavespeed estimates

In order to compute the numerical flux in the HLLC-type methods, estimates for the wave speeds S_L and S_R are needed. There are several different approaches to estimate these wave speeds, some of which are outlined in [35], Section 10.5. In this work, the Roe average wave speed estimate is used.

Both Davis [42] and Einfeldt [43] suggest using the Roe averaged eigenvalues [44] for the wave speeds;

$$S_{L,j+1/2} = \min\left(\lambda_1(\boldsymbol{U}_j), \lambda_1(\widehat{\boldsymbol{U}}_{j+1/2})\right),\ S_{R,j+1/2} = \max\left(\lambda_3(\boldsymbol{U}_{j+1}), \lambda_3(\widehat{\boldsymbol{U}}_{j+1/2})\right), \tag{3.106}$$

where $\widehat{\boldsymbol{U}}$ is the Roe average of the conserved variables. This method has been reported to be very robust [35, 45]. Both for the Euler equations and the Euler equations with area change, (3.106) becomes

$$S_{L,j+1/2} = \min\left(u_j - c_j, \hat{u}_{j+1/2} - \hat{c}_{j+1/2}\right),\ S_{R,j+1/2} = \max\left(u_{j+1} + c_{j+1}, \hat{u}_{j+1/2} + \hat{c}_{j+1/2}\right), \tag{3.107}$$

where $\hat{u}$ is the Roe averaged particle speed and $\hat{c}$ is the Roe averaged sound speed. The Roe averaged variables can be found by the Roe averaged matrix $\widehat{\boldsymbol{A}}(\boldsymbol{U}_L, \boldsymbol{U}_R)$ [44].

Averages for the Euler equations

For the Euler equations, the Roe averaged matrix, $\widehat{\boldsymbol{A}}(\boldsymbol{U}_L, \boldsymbol{U}_R)$ must satisfy the following conditions:

R1: $\widehat{\boldsymbol{A}}(\boldsymbol{U}_L, \boldsymbol{U}_R)(\boldsymbol{U}_L - \boldsymbol{U}_{\boldsymbol{R}}) = \boldsymbol{F}(\boldsymbol{U}_R) - \boldsymbol{F}(\boldsymbol{U}_L)$,
R2: $\widehat{\boldsymbol{A}}(\boldsymbol{U}_L, \boldsymbol{U}_R)$ is diagonalizable with real eigenvalues, and
R3: $\widehat{\boldsymbol{A}}(\boldsymbol{U}_L, \boldsymbol{U}_R) \to \dfrac{\partial \boldsymbol{F}}{\partial \boldsymbol{U}}$ smoothly as $\boldsymbol{U}_L, \boldsymbol{U}_R \to \boldsymbol{U}$.

A study on how to obtain Roe averaged variables for the Euler equations with a general equation of state was conducted in the project work leading up to this master's thesis, [13]. The following averages were found which satisfy the conditions R1-R3 for a general equation of state:

$$\hat{\rho} = \frac{\rho_L + \rho_R}{2}, \tag{3.108}$$

$$\hat{u} = \frac{\sqrt{\rho_L} u_L + \sqrt{\rho_R} u_R}{\sqrt{\rho_L} + \sqrt{\rho_R}}, \tag{3.109}$$

$$\hat{H} = \frac{\sqrt{\rho_L} H_L + \sqrt{\rho_R} H_R}{\sqrt{\rho_L} + \sqrt{\rho_R}}. \tag{3.110}$$

All other averaged variables can be calculated based on these, using

$$\hat{h} = \hat{H} - \frac{1}{2}\hat{u}^2 \tag{3.111}$$

giving $\hat{p} = \hat{p}(\hat{\rho}, \hat{h})$, $\hat{c} = \hat{c}(\hat{\rho}, \hat{h})$. The averaged internal energy becomes

$$\hat{e} = \hat{H} - \frac{\hat{p}}{\hat{\rho}} - \frac{1}{2}\hat{u}^2. \tag{3.112}$$

Averages for the Euler equations with area change

The Jacobi matrix $\boldsymbol{A}$ for the Euler equations with area change was determined by including the source term in its formulation. Therefore, the source term must also be incorporated in the conditions which the Roe averaged Jacobi matrix $\widehat{\boldsymbol{A}}$ must satisfy. The following new set of conditions for the Roe averaged matrix $\widehat{\boldsymbol{A}}$ are proposed;

RS1: $\widehat{\boldsymbol{A}}(\boldsymbol{U}_L, \boldsymbol{U}_R)(\boldsymbol{U}_R - \boldsymbol{U}_L) = \boldsymbol{F}(\boldsymbol{U}_R) - \boldsymbol{F}(\boldsymbol{U}_L) - \widehat{\boldsymbol{S}}$, where

$$\widehat{\boldsymbol{S}} = \begin{pmatrix} 0 \\ \hat{p}(\boldsymbol{U}_L, \boldsymbol{U}_R)(A_R - A_L) \\ 0 \\ 0 \end{pmatrix}, \tag{3.113}$$

RS2: $\widehat{\boldsymbol{A}}(\boldsymbol{U}_L, \boldsymbol{U}_R)$ has real eigenvalues and is *not* diagonalizable, and
RS3: $\widehat{\boldsymbol{A}}(\boldsymbol{U}_L, \boldsymbol{U}_R) \to \boldsymbol{A}(\boldsymbol{U})$ smoothly as $\boldsymbol{U}_L, \boldsymbol{U}_R \to \boldsymbol{U}$.

$\widehat{\boldsymbol{A}}$ can be determined by finding a special average of the state vectors $\boldsymbol{U}_L$ and $\boldsymbol{U}_R$, $\widehat{\boldsymbol{U}}(\boldsymbol{U}_L, \boldsymbol{U}_R)$ such that $\widehat{\boldsymbol{A}} = \boldsymbol{A}(\widehat{\boldsymbol{U}})$. A set of averages satisfying RS1-RS3 have been found in this work by testing averages inspired by the Roe averages for the Euler equations without area change. These averages are:

$$\widehat{\rho A} = \frac{\rho_L A_L + \rho_R A_R}{2}, \tag{3.114}$$

$$\hat{A} = \frac{A_L + A_R}{2}, \tag{3.115}$$

$$\hat{u} = \frac{\sqrt{\rho_L A_L} u_L + \sqrt{\rho_R A_R} u_R}{\sqrt{\rho_L A_L} + \sqrt{\rho_R A_R}}, \tag{3.116}$$

$$\hat{H} = \frac{\sqrt{\rho_L A_L} H_L + \sqrt{\rho_R A_R} H_R}{\sqrt{\rho_L A_L} + \sqrt{\rho_R A_R}}. \tag{3.117}$$

All other averaged variables can be calculated based on these, using

$$\hat{h} = \hat{H} - \frac{1}{2}\hat{u}^2 \tag{3.118}$$

and

$$\hat{\rho} = \frac{\widehat{\rho A}}{\hat{A}}, \tag{3.119}$$

giving $\hat{p} = \hat{p}(\hat{\rho}, \hat{h})$, $\hat{c} = \hat{c}(\hat{\rho}, \hat{h})$. The averaged internal energy becomes

$$\hat{e} = \hat{H} - \frac{\hat{p}}{\hat{\rho}} - \frac{1}{2}\hat{u}^2. \tag{3.120}$$

3.1.10. Summary

In this section we have introduced the numerical solvers which are applied in this work. All the solvers are finite-volume methods. For solving the Euler equations, LxF and HLLC are introduced. Two new methods are suggested for solving the Euler equations with area change, HLLC+S and HLLCS. HLLC+S simply adds a source term to HLLC which satisfies the non-disturbance relation discussed by Liou et al. [41].

For the HLLC solver, we assume there are three waves in the solution. However, for the Euler equations with area change, there will be four waves present. We therefore introduce an HLLC-type solver, HLLCS, which includes the fourth stationary wave across the area change. Our approach in deriving HLLCS is similar to that of Murillo and García-Navarro [26] for the shallow-water equations, and Tokareva and Toro for the Baer-Nunziato equations [25]. The addition of the fourth wave leads to a nonlinear system for subsonic flow which must be solved for example by the Newton-Rhapson method at each grid cell. We suggest two possible source terms to be applied with HLLCS, RS and FS. RS is applied for supersonic flow, but can also be applied for subsonic flow. FS can only be applied for subsonic flow as it is based on the fluxes found from the nonlinear system for subsonic flow. FS can provide poor estimates if the Newton-Rhapson iterations do not converge and the error is large.

HLLC, HLLC+S and HLLCS all need estimates of the wavespeeds for the waves in the problem. In this work Roe averaged wavespeeds are applied. We introduce valid Roe averages for the Euler equations satisfying the conditions R1-R3 given by Roe [44]. For the Euler equations with area change, we propose the new conditions RS1-RS3 which take into account the source term, and give averages which satisfy these conditions.

3.2. Boundary treatment for depressurization with the Euler equations

We will now focus on the boundary conditions of the domain and in particular in the case of depressurization. For numerical benchmark tests it is common to use transmissive boundary conditions (BCs)

$$\begin{aligned}\mathbf{U}_0^{n+1} &= \mathbf{U}_1^{n+1},\\ \mathbf{U}_{N_j+1}^{n+1} &= \mathbf{U}_{N_j}^{n+1}.\end{aligned}$$

This was used in the introductory work for this master thesis [13], and is also used here for benchmark tests of HLLC+S and HLLCS presented in Section 4.2. When studying pipe depressurization to ambient air, there will be a boundary to the outside. It is important to model this accurately in order to capture the acceleration of fluid at the pipe outlet due to the large pressure difference between the fluid in the pipe and the ambient air.

In the following subsections, three different BCs for outflow and a BC for a solid wall are outlined. These BCs are applied for the Euler equations, meaning that we assume

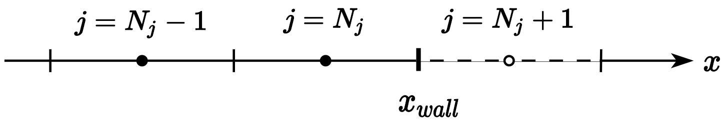

Figure 3.9.: A ghost cell (dotted lines) is introduced at the end of the domain, next to the solid wall.

the cross-sectional area is constant. We here choose the outlet to be at the left end of the domain and the wall at the right end of the domain so the flow will be in the *negative direction.* This choice is motivated by the experimental data which we compare our results to in Section 4.4 being set up this way.

3.2.1. Wall

The simplest boundary condition is for the wall. No permeability is assumed so $u(x_{\text{wall}}) = 0$. To ensure this, a fictitious "ghost cell" is introduced next to the last cell in the domain. This is depicted in Figure 3.9. In this ghost cell,

$$u_{N_j+1} = -u_{N_j} \tag{3.121}$$

is set. Otherwise the state is the same as in the neighboring cell,

$$\begin{aligned}\rho_{N_j+1} &= \rho_{N_j}\\ E_{N_j+1} &= E_{N_j}.\end{aligned}$$

This boundary condition allows for the complete reflection of waves at the wall.

3.2.2. Outflow

At an outflow boundary, the information coming from the outside must be set by boundary conditions. Similarly to the solid wall boundary, a ghost cell is introduced next to the boundary as illustrated in Figure 3.10. Note that in the following discussion we will take outflow to be flow in the *negative* x-direction. At the boundary between the inside of the pipe and the ghost cell we should either have subsonic or sonic flow. We

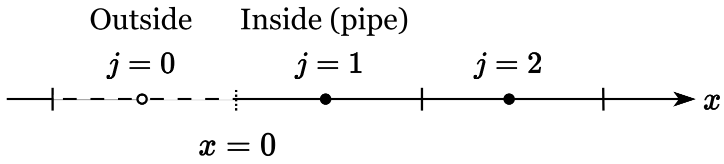

Figure 3.10.: A ghost cell (dotted lines) is introduced outside the pipe, before the computational domain.

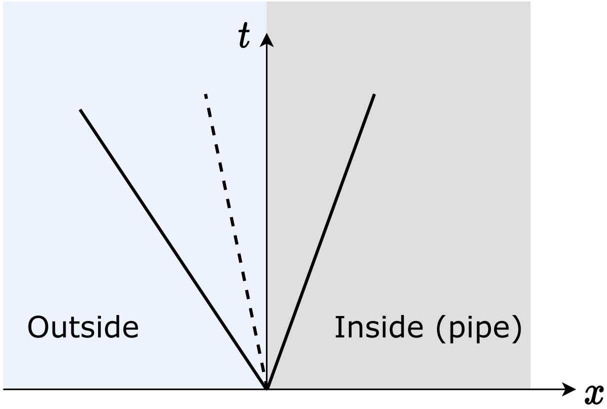

Figure 3.11.: In the case of subsonic outflow, one characteristic is entering the pipe. Therefore, pressure-information from outside is propagated into the pipe.

approximate the fluid speed at the boundary by the fluid speed at the cell center of the first cell within the computational domain,

$$u_{\text{boundary}} \approx u_{j=1}. \tag{3.122}$$

As sonic flow is at the transition between subsonic and supersonic flow, a good boundary condition for subsonic flow (or equivalently supersonic flow) should also work for the limiting sonic case.

At subsonic speeds, $|u_{\text{boundary}}| < c_{\text{boundary}}$, one characteristic is entering the pipe, the other two are exiting the pipe as illustrated in Figure 3.11. Therefore, one variable must be prescribed at the ghost-cell outside the computational domain, and two others must be determined based on information from the inside. For depressurization, it is natural to prescribe the ambient pressure at the ghost cell,

$$p_0 = p_{\text{amb}}. \tag{3.123}$$

This is called a *pressure BC*. For two of the BCs which are introduced below, Naive BC and Bernoulli BC, the pressure in the ghost cell is always the ambient pressure. For the last, more refined BC, the Characteristic BC, the pressure in the ghost cell is set near its local choke pressure if sonic flow is reached. This is further described when the Characteristic BC is explained below. In addition to setting the pressure at the boundary we assume that the entropy is constant between the first cell inside the pipe and the ghost cell outside,

$$s_0 = s_1. \tag{3.124}$$

For depressurization, the wave entering the pipe will be a rarefaction. Extrapolating the entropy is therefore reasonable, because s is constant through a rarefaction as shown in Appendix C. So we can “reach the outside state by crossing the rarefaction”.

As p, s in the ghost cell is then known, the full thermodynamic state of the ghost cell is determined. The final unknown in the ghost cell is the fluid speed, u_{out}. We present three methods to find u_{out} of increasing complexity: simple extrapolation, using Bernoulli's principle or computing u_{out} using the characteristic associated with the rarefaction.

Naive BC

The simplest estimate of the fluid speed in the ghost cell is to simply extrapolate the speed from the neighboring cell inside the pipe,

$$u_0 = u_1. \tag{3.125}$$

This estimate is a bit inaccurate as it can give supersonic flow at the outlet as seen in Section 4.4.

Bernoulli BC

A more accurate approximation is to use a steady-state flow assumption and applying Bernoulli's principle which takes the following form for compressible flow,

$$h_0 + \frac{1}{2}u_0^2 = h_1 + \frac{1}{2}u_1^2. \tag{3.126}$$

Bernoulli's principle also assumes isentropic flow. h_0 can be found from p_0 and s_0. Equation (3.126) can then be used to determine u_0:

$$u_0 = \pm\sqrt{2\left(h_1 - h_0 + \frac{1}{2}u_1^2\right)}. \tag{3.127}$$

The sign of u_0 depends on whether the flow is in the positive or negative x-direction. For the setup used in this work, the negative sign must be chosen. This estimate can also give supersonic flow at the pipe outlet as shown in Section 4.4.

A further step which can be taken to improve this BC is to limit the flow in the ghost cell to sonic speeds such that if this estimate gives $u_0 > c_0$, u_0 is set to c_0 and the corresponding choke pressure in the ghost cell for s_1, c_0 is set instead of the ambient pressure. This method is described by Munkejord and Hammer in [11].

Characteristic BC

The theoretically correct method is to determine the speed in the ghost cell by using the characteristic associated with the rarefaction entering the pipe. For the setup used here, where outflow is in the *negative* x-direction, this is the characteristic associated with the eigenvalue $\lambda_3 = u + c$ of the Euler equations.

$$\partial w_3 = 0 \Leftrightarrow \partial p + \rho c \partial u = 0 \tag{3.128}$$

As we have isentropic flow, (3.128) can be rewritten as

$$\mathrm{d}p + \rho c \,\mathrm{d}u = 0. \tag{3.129}$$

The speed u_0 can be found by rearranging and integrating (3.129) as shown below.

$$\int_{u_1}^{u_0} \mathrm{d}u = -\int_{p_1}^{p_0=p_{\mathrm{atm}}} \frac{1}{\rho c}\,\mathrm{d}p \tag{3.130}$$

$$u_0 - u_1 = -\int_{p_1}^{p_{\mathrm{atm}}} \frac{1}{\rho c}\,\mathrm{d}p \tag{3.131}$$

$$u_0 = u_1 - \int_{p_1}^{p_{\mathrm{atm}}} \frac{1}{\rho c}\,\mathrm{d}p \tag{3.132}$$

The integral $\int_{p_1}^{p_{\mathrm{atm}}} \frac{1}{\rho c} dp$ is difficult to evaluate for a general EOS. A simple, general method is to integrate this numerically. Then a *ps*-flash, a *p*-*s* optimization problem, must be solved for each step in the integration to obtain the values of ρ and c along the pressure path. In this work, the trapezoidal method with $n = 20$ steps is used.

In the numerical integration it is fairly easy to restrict the speed in the ghost cell, u_0. At each step i of the integration it is checked whether

$$u = u_1 - \int_{1}^{\frac{p_1 - p_{\mathrm{atm}}}{n} i} \frac{1}{\rho c} dp \geq c\left(\frac{p_1 - p_{\mathrm{atm}}}{n} i, s_1\right)\ , i = 1, \cdots, n \tag{3.133}$$

If this is the case, the integration is stopped and the state in the ghost cell is set to the state reached in the integration step i such that $p_0 := \frac{p_1 - p_{\mathrm{atm}}}{n} i, s_0 = s_1, u_0 = c_0$.

3.2.3. Summary

A full summary of the boundary treatment in this work is presented in Algorithm 2. Here, the index $j = 0$ refers to the ghost cell outside the pipe and the index $j = N_j + 1$ refers to the ghost cell next to the back wall of the pipe.

Algorithm 2: Overview of the boundary treatment for depressurization with the Euler equations.

```
Result: Boundary conditions for depressurization are set.

Wall:
$\rho_{N_j+1} = \rho_{N_j}$ ;
$(\rho u)_{N_j+1} = -(\rho u)_{N_j}$ ;
$E_{N_j+1} = E_{N_j}$ ;

Outflow:
$p_0 = p_{amb}$ ;
$s_0 = s_1$ ;
Calculate $e_0, \rho_0$ given $p_0, s_0$ (ps-flash) ;
Determine $u_0$ either by simple extrapolation (3.125), by using Bernoulli's
  principle (3.127) or by integrating across the rarefaction wave (3.132) and
  stopping the integration if (3.133) is true;
```

4. Numerical tests

In the following, the results of numerical tests are presented. The purpose of the tests is to describe the accuracy and robustness of the methods. First, HLLCS and its nonlinear system for subsonic flow is investigated for local Riemann problems in Section 4.1 In Section 4.2, HLLC+S and HLLCS are compared to the exact solution on numerous benchmark tests for ideal gas EOS. HLLC+S is further tested on two-phase problems with the Peng-Robinson EOS for a converging-diverging nozzle and on tests proposed by Brown et al. [31]. Lastly, the results of LxF and HLLC for a depressurization test with different outflow BCs are compared to experimental data in Section 4.4.

For benchmark tests with the ideal gas EOS it is common to use nondimensional variables. We will therefore operate with the nondimensional quantities ρ/ρ_{ref}, p/p_{ref}, x/x_{ref}, etc. with the ideal gas EOS. Here, $*_{\mathrm{ref}}$ signifies a reference value of the respective variable. For brevity we will still call ρ/ρ_{ref} density and not dimensionless density, p/p_{ref} for pressure and not dimensionless pressure, and so on.

4.1. Investigation of the HLLCS approximate Riemann solver for local Riemann problems

If subsonic flow is identified in the HLLCS scheme, a nonlinear system is solved by the Newton-Rhapson method in order to determine the unknown intermediate states and thereby the fluxes, see Subsection 3.1.7. It is therefore important to study the convergence of the Newton-Rhapson solver, and to investigate the nonlinear system for different Riemann problems.

4.1.1. Convergence of the Newton-Rhapson solver

In this work, the Newton-Rhapson solver in the HLLCS scheme is limited to a maximum of 7 iteration steps, and the relative error tolerance is set to 10^{-6}. With these parameters, the Newton-Rhapson solver tends to converge for the systems (3.76) or (3.91) within 4 iterations. However, for some cases, the solver might not converge at all as we will come back to in the next subsection.

In the HLLCS method for the BN equations, Tokareva and Toro [25] report that 1-2 iterations are sufficient for convergence of Newton's method for all the test cases studied. This behaviour is not seen in our HLLCS solver for the Euler equations with area change. However, it is difficult to make comparisons to the convergence of Tokareva and Toro's solver as the tolerance used in their Newton solver is not stated. Due to the similarity

Table 4.1.: The left and right states for the Sod shock tube problem.

	p/p_{ref}	u/u_{ref}	ρ/ρ_{ref}	A/A_{ref}
Left	1.0	0.0	1.0	1.0
Right	0.1	0.0	0.125	1.0

between the Euler equations with area change and the BN equations, see Subection 2.3.3, HLLCS should behave similarly for both systems.

4.1.2. Local Riemann problems

We will now investigate the nonlinear system for positive subsonic flow, (3.76), for different versions of the Sod shock tube problem: the Sod shock tube problem with no area change $A_L = A_R$, with $A_L > A_R$ and with $A_L < A_R$. For the case with no area change, the solutions of the system are compared to the solution of the HLLC solver. In all these tests the ideal gas EOS is used. The system for positive subsonic flow is

$$\boldsymbol{f} = \begin{pmatrix} A_L \rho_L^- u_L^- - A_R \rho_R^+ u_R^+ \\ h_R^+ + \frac{1}{2}\left(u_R^+\right)^2 - \left[h_L^- + \frac{1}{2}\left(u_L^-\right)^2\right] \end{pmatrix} = \mathbf{0}, \tag{4.1}$$

where $\boldsymbol{f}$ is a function of the pressures p_L^- and p_R^+.

Sod's shock tube, $A_L = A_R$

Sod's shock tube test problem is a common test for approximate Riemann solvers. It is a Riemann problem whose solution consists of a left rarefaction, a contact discontinuity and a right shock, see Section 10.8 in Toro [35]. The left and right states for the Sod shock tube problem are given in Table 4.1.

In Figure 4.1a, the values of p_L^-, p_R^+ for which each of the components of $\boldsymbol{f}$ is equal to zero are plotted for the Sod shock tube problem. Here, $A_L \rho_L^- u_L^- = A_R \rho_R^+ u_R^+$ is shown in blue and $h_R^+ + \frac{1}{2}\left(u_R^+\right)^2 = h_L^- + \frac{1}{2}\left(u_L^-\right)^2$ is shown in red. When the lines cross, there is a solution to the system $\boldsymbol{f} = \mathbf{0}$. The red and blue lines appear to be overlapping along a short interval. Here, the lines cross twice, once for $p_L^- = p_R^+ \approx 0.1976$, and once for $p_L^- = 0.2136$, $p_R^+ = 0.2002$. The first solution of p_L^-, p_R^+, HLLCS 1, gives the same intermediate states as HLLC whereas the second solution, HLLCS 2, gives slightly different intermediate states. The intermediate states for HLLC, HLLCS 1 and HLLCS 2 are given in Table 4.2. With the initial guess provided by the Adaptive Approximate Riemann solver from Section 4.9 in [35], the Newton iterations converge to the second solution, $p_L^- = 0.2136$, $p_R^+ = 0.2002$, with 6 steps and an error of magnitude 10^{-7}.

Modified Sod's shock tube, $A_L > A_R$

We now introduce a modified version of the Sod shock tube problem where the area in the left state is larger than that for the right state. For the test we take $A_L/A_{\mathrm{ref}} =$

Table 4.2.: Comparison of HLLC's intermediate states to HLLCS' two possible intermediate states for the local Sod shock tube problem. HLLCS 1 corresponds to the solution $p_L^- = p_R^+ = 0.1976$ and HLLCS 2 corresponds to the solution $p_L^- = 0.2136$ and $p_R^+ = 0.2002$.

	HLLC	HLLCS 1	HLLCS 2
ρ_L^-	0.6357	0.6357	0.6403
$(\rho u)_L^-$	0.4311	0.4311	0.4256
E_L^-	1.5172	1.5172	1.5240
ρ_R^+	0.6357	0.6357	0.6113
$(\rho u)_R^+$	0.4311	0.4311	0.4256
E_R^+	1.5172	1.5172	1.4588
ρ_R^{++}	0.3039	0.3039	0.3159
$(\rho u)_R^{++}$	0.2061	0.2061	0.2199
E_R^{++}	0.8907	0.8907	0.9376

1.0, $A_R/A_{\text{ref}} = 0.9$. Figure 4.1b shows where $f_1(p_L^-, p_R^+) = 0$ and $f_2(p_L^-, p_R^+) = 0$ for this problem. Here, there are two clear solutions to the problem, one for which $p_L^- = 0.1225 < p_R^+ = 0.1876$ and one for which $p_L^- = 0.3366 > p_R^+ = 0.2212$. As $p_L/p_{\text{ref}} > p_R/p_{\text{ref}}$, the correct solution should be for $p_L^- > p_R^+$.

With the initial guess provided by the Approximate Riemann solver given in [35], Section 4.9, the Newton iterations for the HLLCS scheme converge to the correct solution with 4 steps and a residual error of magnitude 10^{-10}. One should note, however, that a different choice of initial guess can cause the solver to converge to the *incorrect* solution.

Modified Sod's shock tube, $A_L < A_R$

Finally we introduce a modified Sod's shock tube problem where the area in the left state is smaller than that of the right state. For the test we take $A_L/A_{\text{ref}} = 1.0$, $A_R/A_{\text{ref}} = 1.1$. Figure 4.1c shows where $f_1(p_L^-, p_R^+) = 0$ and $f_2(p_L^-, p_R^+) = 0$ for this shock tube problem. It is clear that there is no solution for the system $\boldsymbol{f} = \boldsymbol{0}$ as the lines $f_1(p_L^-, p_R^+) = 0$ and $f_2(p_L^-, p_R^+) = 0$ do not cross. As the separation between the two lines is greater than the tolerance of the Newton solver (10^{-6}), the iterations do not converge.

Further investigation shows that this problem is *resonant.* The solution to this problem has a similar structure to the resonant case introduced in Subsection 2.3.2, where an "extra" shock is induced between the 0-wave and the contact discontinuity. This means that HLLCS' assumption about the wave structure in the problem is incorrect. For all the resonant cases tested in this work, none had a solution for the nonlinear system which is solved in HLLCS. The flux-based source term for HLLCS depends on the convergence of the method, so it cannot be used for resonant problems. Despite the non-convergence of the system, the HLLCS solver shows promising results for resonant test problems when the Roe average-based source term is applied as is shown in Subsection 4.2.4.

4.1.3. Summary

In this section, the nonlinear system in the HLLCS solver has been investigated for three local Sod shock tube problems with $A_L = A_R$, $A_L > A_R$ and $A_L < A_R$. For $A_L \geq A_R$, the nonlinear system has two solutions, but the separation between the solutions is much larger for $A_L > A_R$ than for $A_L = A_R$. For $A_L < A_R$, the problem is resonant and no solutions exist for the nonlinear system. If two solutions exist, the Newton-Rhapson solver can converge to the incorrect solution when a bad initial guess is used. With the initial guess given by the Approximate Riemann Solver from Section 4.9 in [35], the HLLCS scheme works well for the tests studied. The Newton-Rhapson solver applied in this work is limited to a maximum of 7 iterations steps, and the relative error tolerance is set to 10^{-6}.

4.2. Assessment of HLLCS and HLLC+S-based finite-volume methods for tests with ideal gas EOS

In this section a number of selected benchmark tests for the Euler equations with area change and the ideal gas EOS are used to test the performance of the HLLCS method derived in Subsection 3.1.6 and the HLLC+S method suggested in Subsection 3.1.4. For all these tests, unless otherwise stated, the number of grid cells are set to $N_j = 100$, the CFL number is set to $C = \frac{\max(\lambda)\Delta t}{\Delta x} = 0.9$ and extrapolation is used at the boundaries. As mentioned in Section 2.4, $\gamma = 1.4$ in the ideal gas EOS.

4.2.1. Steady-state

First two steady-state tests, Test 1 and Test 2, are applied on HLLCS and HLLC+S in order to determine whether the methods are well-balanced i.e. whether they can capture stationary waves exactly. For HLLCS both the Roe average-based source term (RS) and the flux-based source term (FS) are tested.

Test 1

Test 1 is taken from Tokareva and Toro [25] and the solution is a stationary contact discontinuity located exactly at the area change. The initial condition for Test 1 is given in Table 4.3. For this test, the computational domain is $x/x_{\text{ref}} \in [0, 1]$ and the separation between the left and right states is at $x/x_{\text{ref}} = 0.5$. The density solutions for HLLC+S and HLLCS at $t/t_{\text{ref}} = 0.2$ are plotted in Figure 4.2a. Both HLLC+S and HLLCS with FS capture the stationary contact discontinuity exactly. HLLCS with RS captures it fairly well, but not exactly, showing that HLLCS with RS is not well-balanced.

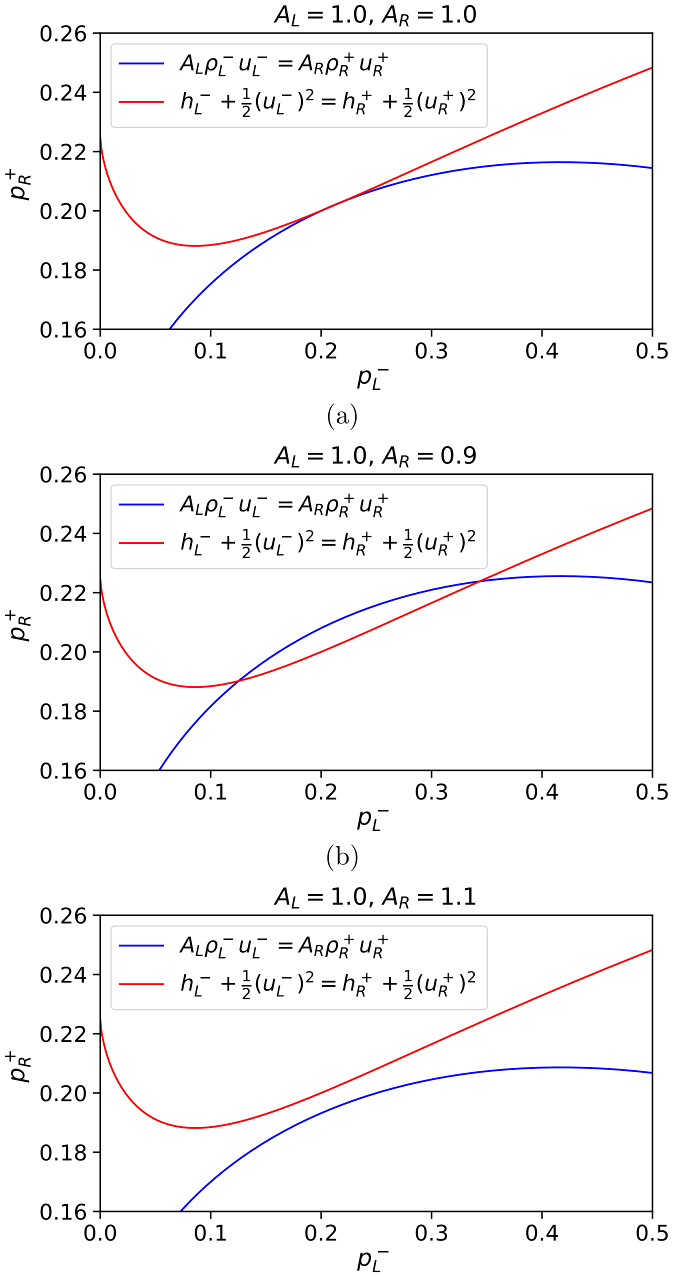

(a)

(b)

(c)

Figure 4.1.: The graph shows for which values of p_L^-, p_R^+ each component of the function $\boldsymbol{f}$ are zero for the Sod's shock tube problem (a), and two modified versions of the problem where $A_L = 0.9$, $A_R = 1.0$ (b) and $A_L = 1.0$, $A_R = 1.1$ (c). If the lines cross, $\boldsymbol{f} = \boldsymbol{0}$ has a solution.

Table 4.3.: The left and right states for Test 1.

	p/p_{ref}	u/u_{ref}	ρ/ρ_{ref}	A/A_{ref}
Left	1.0	0.0	1.4	0.4
Right	1.0	0.0	1.0	0.7

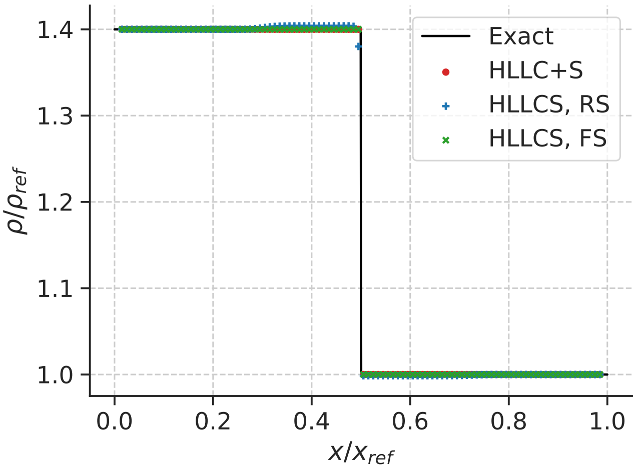

(a) Test 1, at $t/t_{\mathrm{ref}} = 0.2$.

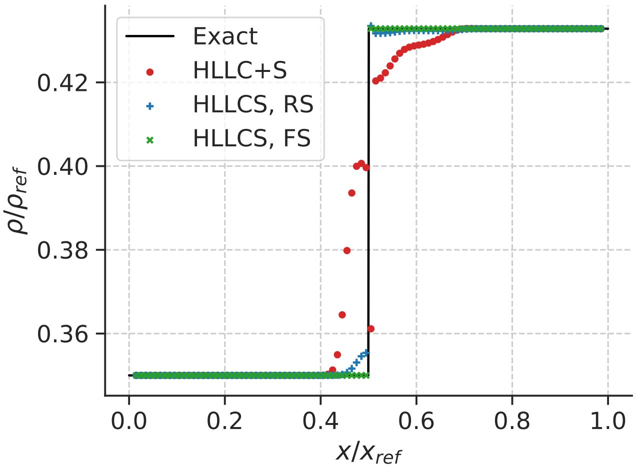

(b) Test 2, at $t/t_{\mathrm{ref}} = 0.02$.

Figure 4.2.: Comparison of the exact density solution (black line) and the solutions of HLLC+S (red circles), HLLCS with RS (blue plus signs) and HLLCS with FS (green crosses) for Test 1 and Test 2.

Table 4.4.: The left and right states for Test 2.

	p/p_{ref}	u/u_{ref}	ρ/ρ_{ref}	A/A_{ref}
Left	10.0	5.0	0.35	1.0
Right	13.462929846413655	2.695480449295447	0.432823271625514	1.5

Test 2

Test 2 is taken from Cuong and Thanh [23], and satisfies the conditions for a stationary wave across the area change. The initial condition for Test 2 is given in Table 4.4. For this test, the computational domain is across $x/x_{\text{ref}} \in [-1, 1]$ and the separation between the left and right states is at $x/x_{\text{ref}} = 0$. The solutions for HLLC+S and HLLCS at $t/t_{\text{ref}} = 0.02$ are plotted in Figure 4.2a.

Test 2 shows that HLLC+S is not well-balanced as the stationary state is not conserved with this scheme. This is caused by the inaccurate discretization of the source term, given in Subsection 3.1.4, page 32. HLLCS with RS does not conserve the steady-state either, however, the solution is not very inaccurate. HLLCS with FS conserves the steady-state in both cases. Therefore, HLLCS with FS is likely well-balanced. This is key in formulating consistent and stable solutions to problems with non-conservative source terms. We further investigate the performance of HLLCS, and HLLC+S as a reference, on two straightforward Riemann problem tests.

4.2.2. Straightforward Riemann problems

We will now study two “straightforward” Riemann problems, to see how the FVM schemes behave for a fairly uncomplicated case. These problems have unique solutions and no resonance. Both of the tests are designed to give Sod-shock-tube-like wave configurations, with an additional stationary wave from the area change. Though these Riemann problems are simple in a mathematical sense, they can still be tough for the FVM schemes due to the presence of the source term across the area change. We therefore investigate two cases, one with a fairly weak source term, Test 3, and one with a stronger source term, Test 4. Both tests give subsonic flow so HLLCS can be tested for both RS and FS The exact solutions for the tests are produced using CONSTRUCT [36], and the configuration data needed to obtain the solution is given in Appendix F.

Test 3, weak source term

In the following, we present Test 3 which includes a weak source term.The initial condition for Test 3 is given in Table 4.5, and the separation between the left and right states is at $x/x_{\text{ref}} = 0.5$. As the difference between the left and right areas is only 14% and the pressure difference is small, the source term is weak. The density and pressure solutions for HLLC+S, HLLCS with RS and HLLCS with FS at $t/t_{\text{ref}} = 0.1$ are shown in Figures 4.3 and 4.4 together with the exact solution.

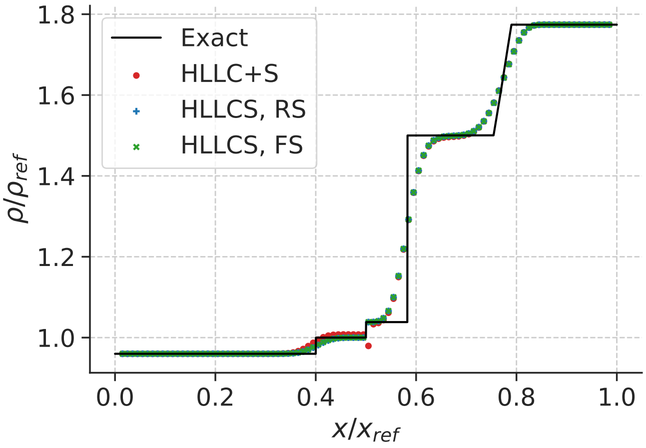

Figure 4.3.: Comparison of the exact density solution (black line) and the solutions of HLLC+S (red circles), HLLCS with RS (blue plus signs) and HLLCS with FS (green crosses) for Test 3 at $t/t_{\mathrm{ref}} = 0.1$.

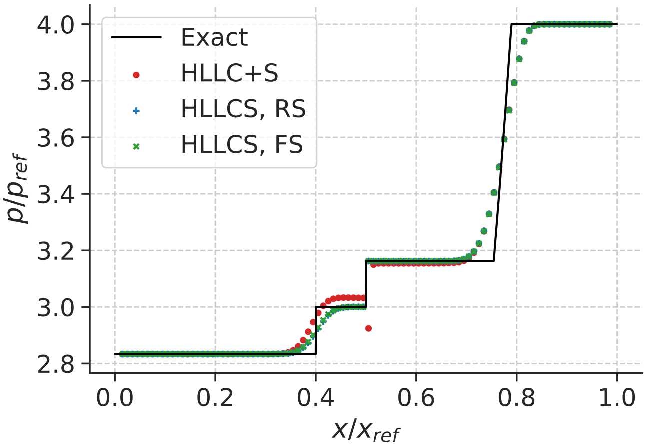

Figure 4.4.: Comparison of the exact pressure solution (black line) and the solutions of HLLC+S (red circles), HLLCS with RS (blue plus signs) and HLLCS with FS (green crosses) for Test 3 at $t/t_{\mathrm{ref}} = 0.1$.

Table 4.5.: The left and right states for Test 3.

	p/p_{ref}	u/u_{ref}	ρ/ρ_{ref}	A/A_{ref}
Left	2.833334	1.083333	0.96	0.6
Right	4.0	2.228730	1.774130	0.7

Based on the density and pressure results, we see that HLLC+S is struggling even for a small source term, giving an undershoot for both density and pressure at the area change in addition to the density and pressure levels being too high between the stationary wave and the shock wave. Otherwise, HLLC+S performs similarly to HLLCS. HLLCS appears to perform equally well with both source terms, RS and FS, for this test. For all the schemes there is numerical dissipation across the contact discontinuity and the rarefaction.

We further present a convergence study for this test. The grids used for the convergence study have tripling numbers of grid cells, N_j, such that cell centers will overlap for all the grids, as shown in [13], Section 4.1. We calculate the 1-norm of error for the density, the density error, by

$$E_{1,\rho}(\Delta x) = \Delta x \sum_{j=1}^{N_j} |\rho_j^{\text{exact}} - \rho_j^{\text{approx}}|,$$

where Δx is the grid spacing, and the convergence rate, l, for tripling N_js by

$$l = \frac{1}{\log(3)} \log\left(\frac{E_{1,\rho}(\Delta x)}{E_{1,\rho}(\frac{\Delta x}{3})}\right).$$

The density error of HLLC+S, HLLCS with RS and HLLCS with FS is shown in Figure 4.5a and the convergence rates for the schemes is shown in Figure 4.5b. The results of the convergence test indicates that HLLC+S settles towards a slightly incorrect solution as its density error appears to flatten for larger N_js. The convergence rate of HLLC+S therefore falls for an increasing N_j. HLLCS' error does not flatten and the scheme with either source term reaches a convergence rate of approximately 0.56. Both HLLCS with RS and HLLCS with FS perform very similarly.

Test 4, strong source term

We now present Test 4, which includes a strong source term. The initial conditions for Test 4, is given in Table 4.6.

For Test 4, there is an 80% difference between the left area and the right area in the problem and a large pressure difference between the left and right states. This creates a strong source term across the area change. The numerical solvers therefore have great smearing near the area change, so a rather fine grid of $N_j = 1000$ is used to resolve the problem to see clearly how the solvers perform. The density and pressure solutions

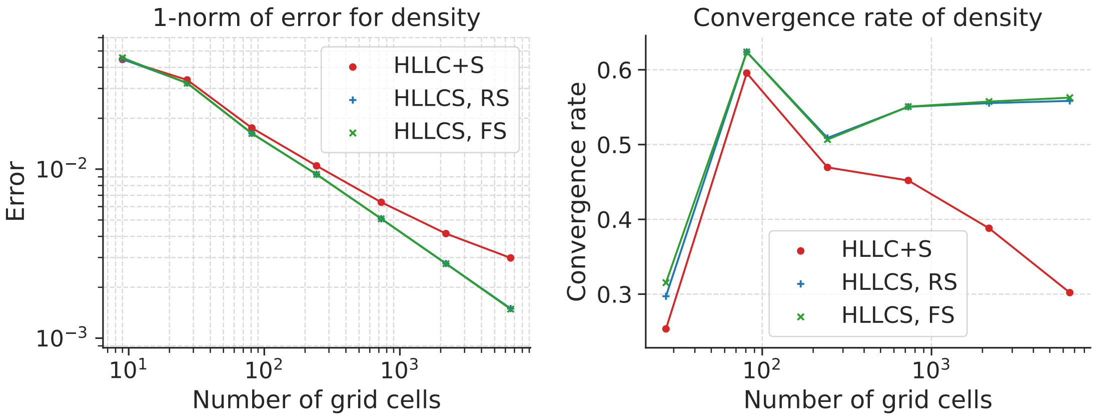

(a) (b)

Figure 4.5.: Results of the convergence test for HLLCS with RS (blue line with plus signs) and HLLCS with FS (green line with crosses) for Test 3.

Table 4.6.: The left and right states for Test 4.

	p/p_{ref}	u/u_{ref}	ρ/ρ_{ref}	A/A_{ref}
Left	3.0	-0.905324246	2.191799866	0.9
Right	0.802900206	0.373720874	0.4645422106	0.2

for HLLC+S and HLLCS with both FS and RS are compared to the exact solution at $t/t_{\text{ref}} = 0.1$ in Figures 4.6 and 4.7, respectively.

For this test, HLLC+S produces unsatisfactory results. The behaviour near the area change does not approximate the exact solution well. The density and pressure after the area change become much too low as compared to the exact solution. Both HLLCS with FS and with RS has numerical smearing between the area change and the contact discontinuity, but appears to approximate the solution well otherwise. HLLCS with RS does not approximate the location of the right shock perfectly, but performs similarly to HLLCS with FS otherwise.

When the grid number is increased, HLLCS' smearing is reduced as is shown in Figure 4.8 where the density results for the schemes with $N_j = 5000$ are compared to the exact solution. HLLC+S' result does not improve as it is converging towards an incorrect solution. HLLCS with RS also improves its location of the right shock for the finer grid. Below, we present a full convergence study for the different numerical schemes on this test problem.

The density error for the solvers is shown in Figure 4.9a and the convergence rate for their density solution is shown in Figure 4.9b. It is clear that HLLCS outperforms HLLC+S. HLLC+S' error settles at approximately 0.02, and its convergence rate falls

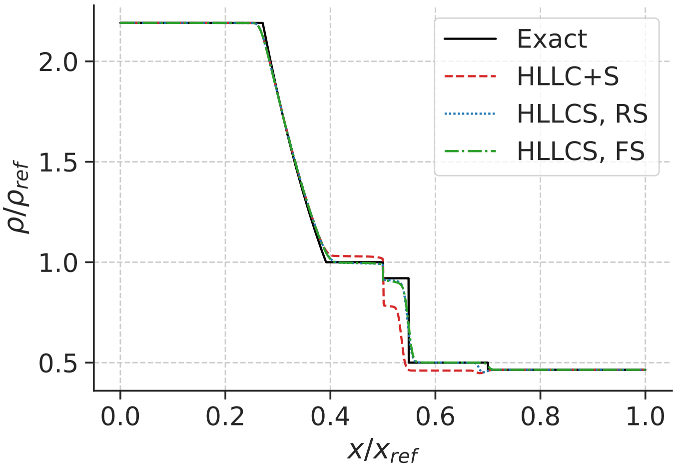

Figure 4.6.: Density solution of HLLC+S (red dashed line), HLLCS with RS (blue dotted line) and HLLCS with FS (green dashdotted line) compared to the exact solution (black line) for Test 4 at $t/t_{\mathrm{ref}} = 0.1$, with $N_j = 1000$.

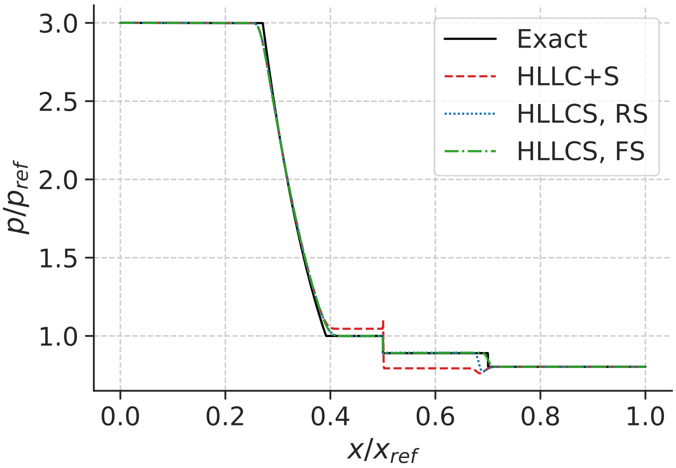

Figure 4.7.: Pressure solution of HLLC+S (red dashed line), HLLCS with RS (blue dotted line) and HLLCS with FS (green dashdotted line) compared to the exact solution (black line) for Test 4 at $t/t_{\mathrm{ref}} = 0.1$, with $N_j = 1000$.

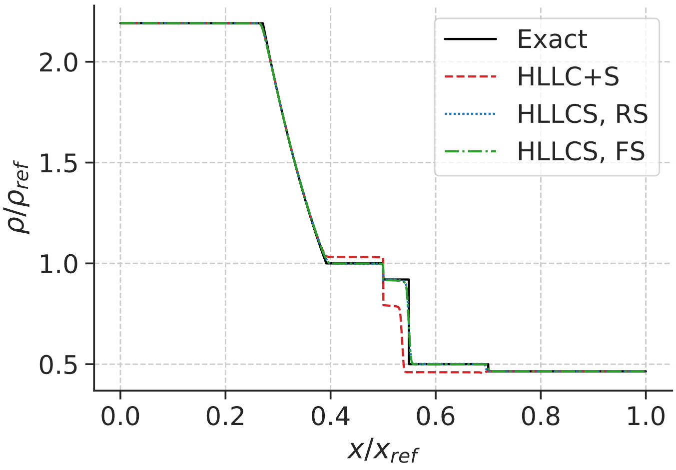

Figure 4.8.: Density solution of HLLC+S (red dashed line), HLLCS with RS (blue dotted line) and HLLCS with FS (green dashdotted line) compared to the exact solution (black line) for Test 4 at $t/t_{\mathrm{ref}} = 0.1$, with $N_j = 5000$.

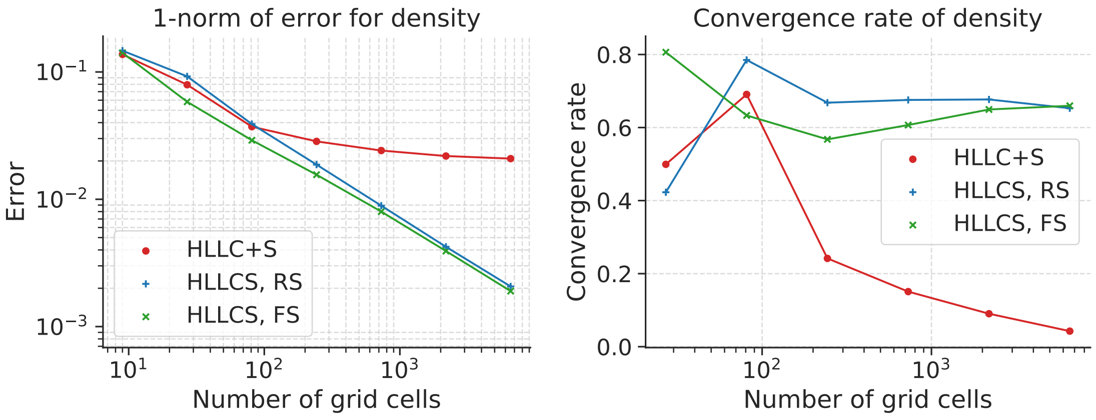

(a)

(b)

Figure 4.9.: Results of the convergence test for HLLC+S (red line with circles), HLLCS with FS (green line with crosses) and HLLCS with RS (blue line with plus signs) for Test 4.

below 0.2. The density error for HLLCS with either RS or FS keeps falling for increasing numbers of grid cells. We see that HLLCS with FS has lower error than HLLCS with RS for all the grids. The convergence rates for HLLCS with both source terms settle towards approximately 0.66.

The results show that HLLC+S does not perform well for strong source terms. The solver does not converge to the exact solution with significant error. Both HLLCS with FS and RS converge towards the exact solution, however, there is numerical smearing between the stationary wave across the area change and the contact discontinuity even with a grid of $N_j = 1000$ cells. HLLCS with FS is the most accurate solver.

4.2.3. Riemann problems with multiple solutions

The tests presented here are based on the work of Andrianov and Warnecke [18], where two Riemann problems with non-unique solutions are presented. Both Riemann problems have two possible solutions, where one is clearly picked out by 2D simulations to be the physically relevant solution. For both tests, the exact solutions were found using CONSTRUCT [36] using the configuration data listed in Appendix F.

Test 5

We first consider Test 5 whose initial condition is presented in Table 4.7. The test involves two converging flows from the left and right with different cross-sectional areas. The domain used is $x/x_{\text{ref}} = [0, 2]$ and the separation of the left and right states for the initial condition is placed at $x/x_{\text{ref}} = 0.5$. The density solution for HLLC+S and HLLCS is plotted at $t/t_{\text{ref}} = 0.4$ and compared to the two possible exact solutions in Figure 4.10.

Table 4.7.: The left and right states for Test 5.

	p/p_{ref}	u/u_{ref}	ρ/ρ_{ref}	A/A_{ref}
Left	0.07	3.991	0.2069	0.8
Right	0.0833	-3.1666	0.1354	0.3

For this test, the physically relevant solution is Configuration B. As can be seen in Figure 4.10, both HLLC+S and HLLCS with FS approximate the physical solution. In addition, HLLCS with FS approximates the solution more accurately than HLLC+S. However, HLLCS with RS approximates the unphysical solution, Configuration A.

This test serves as a cautionary tale regarding the choice of source term. As the test involves converging flows, the pressure builds along the streamlines. This is not reflected well with the Roe averaged source term as the averaged pressure $\hat{p}$ will be somewhere between the left and right pressures, $p_L/p_{\text{ref}}, p_R/p_{\text{ref}}$ early in the simulation. For the very first time-step in the simulation, FS gives $\overline{\boldsymbol{S}}_2 \approx -1.64$, whereas RS gives only $\overline{\boldsymbol{S}}_2 \approx -0.19$ across the area change. After this first timestep, HLLCS with FS finds that the flow is subsonic across the area change, whereas HLLCS with RS finds that it

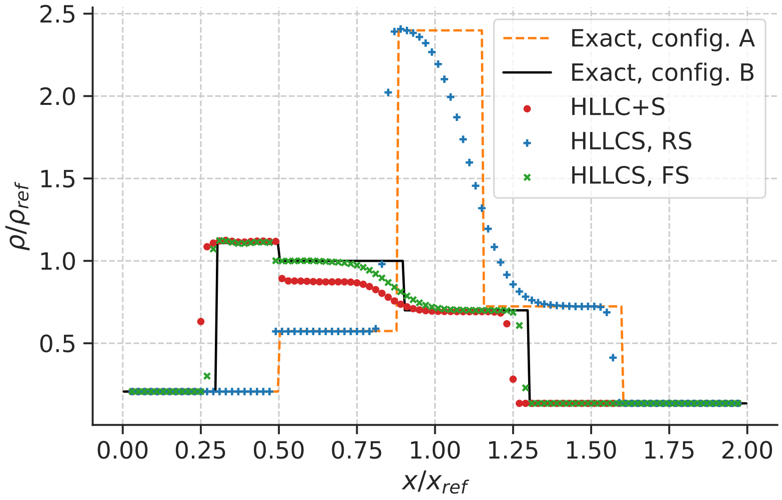

Figure 4.10.: Comparison of the two exact density solutions and the solutions of HLLC+S (red circles), HLLCS with RS (blue plus signs) and HLLCS with FS (green crosses) for Test 5 at $t/t_{\text{ref}} = 0.4$. HLLC+S and HLLCS with FS approximate the physical solution, Configuration B.

is supersonic and it consequently converges to the unphysical solution with supersonic flow.

Test 6

The initial condition for the second test with multiple solutions, Test 6, is presented in Table 4.8. This test is run on the domain $x/x_{\text{ref}} \in [0, 1]$ and the left and right states are separated at $x/x_{\text{ref}} = 0.7$. The density solution for HLLC+S, HLLCS with RS and HLLCS with FS is plotted at $t/t_{\text{ref}} = 0.2$ and compared to the two possible exact solutions in Figure 4.11. Also for this test the physically relevant solution is Configuration B. For this test, all the schemes approximate the physical solution. HLLC+S and HLLCS with RS perform very similarly, both failing to determine the position of the left shock accurately. HLLCS with FS is most accurate and approximates the exact solution well. Once again RS gives a too small source term early in the simulation, but despite its error the flow is still identified as subsonic throughout the simulation and the correct solution

Table 4.8.: The left and right states for Test 6.

	p/p_{ref}	u/u_{ref}	ρ/ρ_{ref}	A/A_{ref}
Left	1.0	3.3	0.2	0.3
Right	0.07	-4.0	0.2	0.8

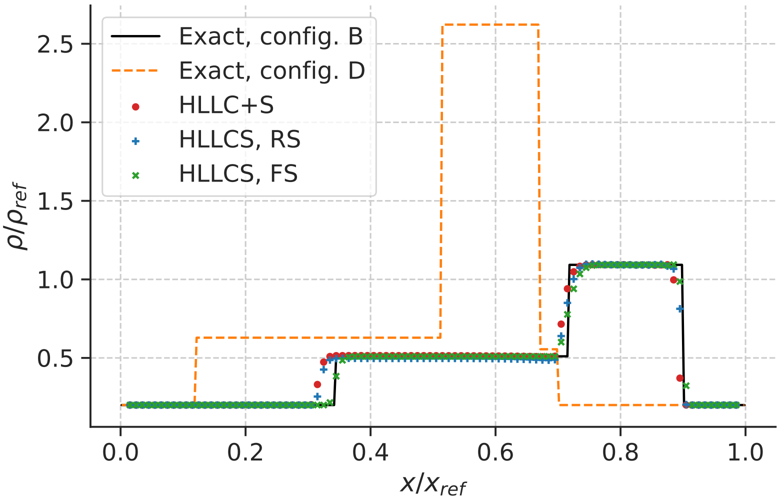

Figure 4.11.: Comparison of the two exact density solutions and the solutions of HLLC+S (red circles), HLLCS with RS (blue plus signs) and HLLCS with FS (green crosses) for Test 6. The solution is plotted at $t/t_{\text{ref}} = 0.2$. All solvers, HLLC+S, HLLCS with FS and HLLCS with RS approximate the physical solution, Configuration B.

is approximated.

4.2.4. Riemann problems with resonant solutions

Here, two resonant tests are presented. These tests are used by Thanh and Kröner [19] to evaluate their Lax-Friedrichs scheme equipped with a computing corrector to capture resonant states, and they are further used by Brown et al. [31] to test their AUSM+-up scheme. As briefly discussed in Section 4.1, the nonlinear equation system used to find the fluxes in the HLLCS approximate Riemann solver does not have a solution for resonant states. Therefore the flux-based source term FS cannot be used and the Roe average-based source term RS is used instead.

Test 7

The first resonant test, Test 7, has the initial condition given in Table 4.9. The test was suggested by Thanh and Kröner [19], and involves the interaction between a rarefaction to the left and a resonant surface which further induces an “extra” shock in the wave configuration. The computational domain for this test is within $x/x_{\text{ref}} \in [0, 2]$ and the the left and right states of the initial condition are separated at $x/x_{\text{ref}} = 1$. In the literature, the test is run with 1000 computational cells [19, 31], so $N_j = 1000$ is also used here. The solutions for density and velocity are given in Figures 4.12 and 4.13

Table 4.9.: The left and right states for Test 7.

	p/p_{ref}	u/u_{ref}	ρ/ρ_{ref}	A/A_{ref}
Left	8.0	0.5	5.0	1.0
Right	1.0	0.8	1.0	1.2

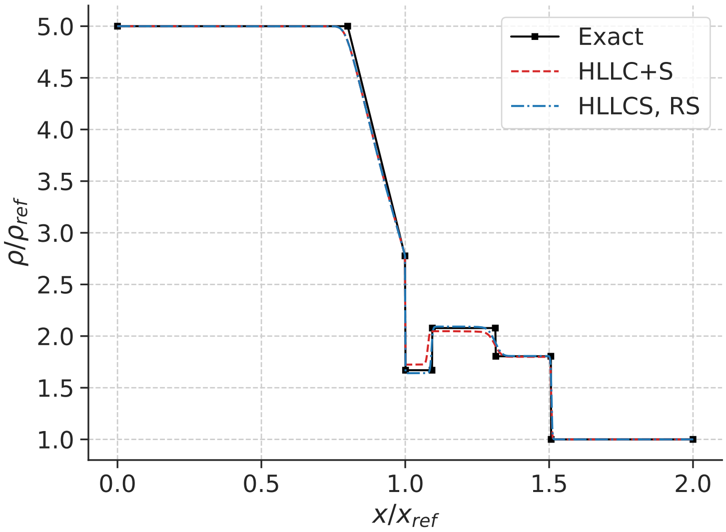

Figure 4.12.: Comparison of exact solution points (black squares) and the density solutions of HLLC+S (red dashed line), and HLLCS with RS (blue dashdotted line) on Test 7 for density at $t/t_{\text{ref}} = 0.2$, $N_j = 1000$.

respectively for HLLC+S and HLLCS with RS at $t/t_{\text{ref}} = 0.2$ together with points of the exact solution listed in Table 1 in [19].

Both HLLC+S and HLLCS resolve the problem well and there is no sign of instability as often occurs for solvers applied on resonant cases [19]. HLLCS approximates the solution better than HLLC+S, which is particularly evident for the density between the stationary wave and the additional shock, for $x/x_{\text{ref}} \in [1, 1.1]$ and further between the additional shock and the contact discontinuity, $x/x_{\text{ref}} \in [1.1, 1.3]$. It can be seen that HLLCS overestimates the velocity of the fluid in the area between the stationary wave and the additional shock. Thanh and Kröner's LxF scheme with the computational corrector does not obtain such an overshoot [19]. Brown et al. however get a similar overshoot for their AUSM+-up scheme for this test [31].

One may note that this case produces a similar result as that for the modified Sod shock tube problem, where $A_L < A_R$, which was discussed briefly in Subsection 4.1. The iterative solver in HLLCS cannot converge for these cases, yet HLLCS with RS still produces a satisfactory result for this particular test.

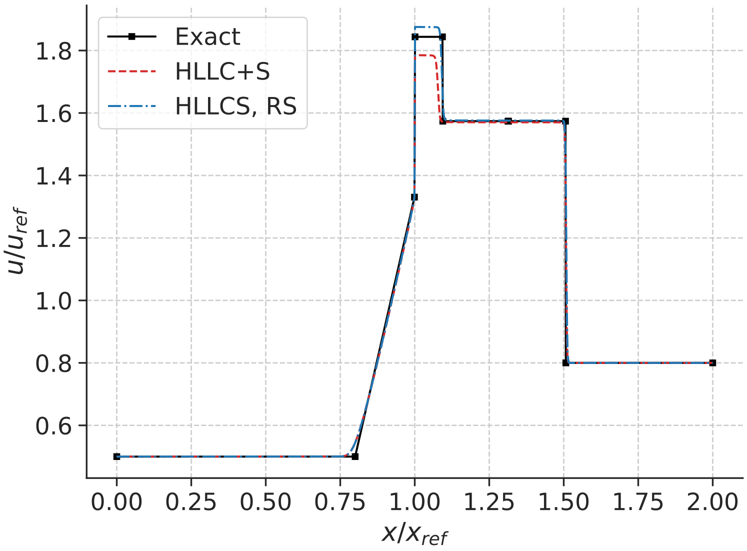

Figure 4.13.: Comparison of exact solution points (black squares) and the velocity solutions of HLLC+S (red dashed line), and HLLCS with RS (blue dashdotted line) on Test 7 for velocity at $t/t_{\mathrm{ref}} = 0.2$, $N_j = 1000$.

Test 8

The second resonant test, Test 8, was first suggested by Rochette et al. [46], where the authors compared the exact solution with 1D and 3D models. For this test, the Riemann solution contains three co-located stationary waves. In Table 4.10 the initial condition is given. For this test the flow is supersonic throughout the domain, so HLLCS with RS is used. The computational domain for this test is $x/x_{\mathrm{ref}} \in [0, 2]$ and the separation between the left and right states of the initial condition is at $x/x_{\mathrm{ref}} = 0.8$. The solutions for density and velocity are given in Figure 4.14 for HLLC+S and HLLCS with RS at $t/t_{\mathrm{ref}} = 0.2$. The results are compared to known points of the exact solution as given in Table 17 in [46].

The structure of the exact solution for Test 8 is described in the following way by Thanh and Kröner [19]: The exact Riemann solution starts by a stationary wave from $\boldsymbol{U}_L$ to $\boldsymbol{U}_1$, followed by a shock with zero speed from $\boldsymbol{U}_1$ to $\boldsymbol{U}_2$, then followed by another stationary wave from $\boldsymbol{U}_2$ to $\boldsymbol{U}_3$. It is attached by a rarefaction wave from $\boldsymbol{U}_3$ to $\boldsymbol{U}_4$,

Table 4.10.: The left and right states for Test 8.

	p/p_{ref}	u/u_{ref}	ρ/ρ_{ref}	A/A_{ref}
Left	1.0	2.0	1.3	1.0
Right	1.0	3.675948	2.363115	0.7

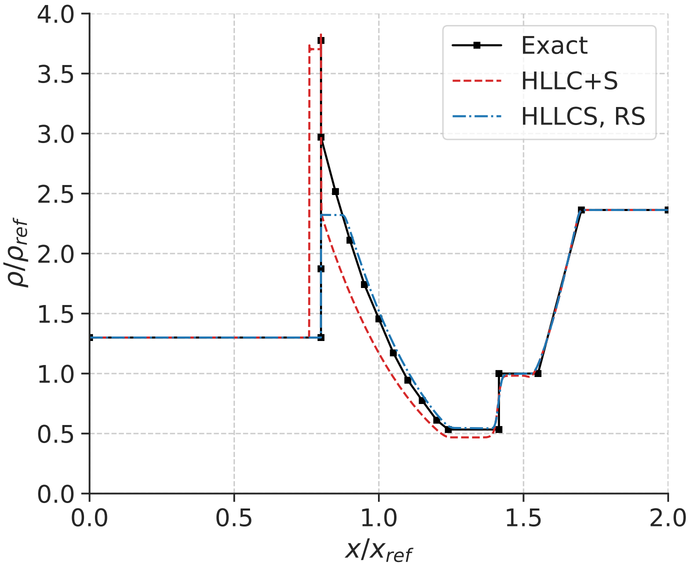

(a) Density

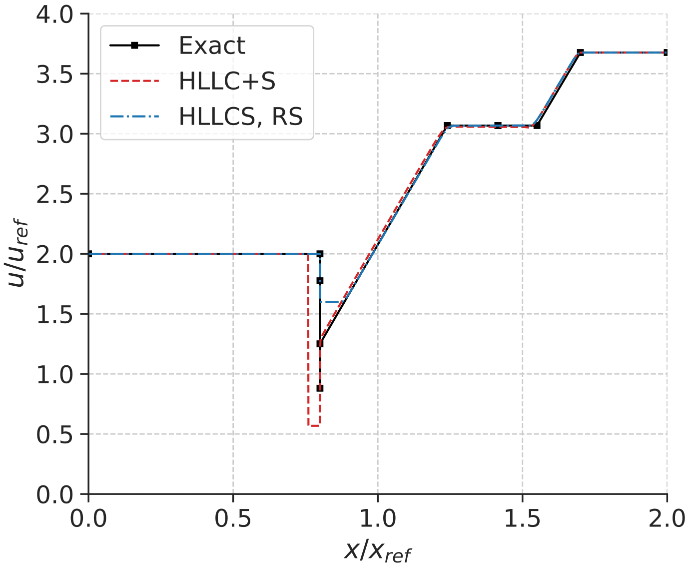

(b) Velocity

Figure 4.14.: Comparison of exact solution points (black squares) and the solutions of HLLC+S (red dashed line), and HLLCS with RS (blue dashdotted line) on Test 7 for density (a) and velocity (b). The solution is plotted at $t/t_{\text{ref}} = 0.2$ and the number of grid cells used are $N_j = 6000$.

Table 4.11.: The densities of the intermediate states occurring for Test 8

ρ_1/ρ_{ref}	ρ_2/ρ_{ref}	ρ_3/ρ_{ref}	ρ_4/ρ_{ref}	ρ_5/ρ_{ref}
1.872903	3.775791	2.969906	0.533582	1.0

and it continues with a contact discontinuity from $\boldsymbol{U}_4$ to $\boldsymbol{U}_5$, and finally it reaches $\boldsymbol{U}_R$ by a shock. The densities corresponding to the different states $\boldsymbol{U}_1, \boldsymbol{U}_2, \boldsymbol{U}_3, \boldsymbol{U}_4$, and $\boldsymbol{U}_5$ are given in Table 4.11.

The results for this test are rather interesting. HLLC+S is trying to capture the stationary shock with the highest density, whereas HLLCS with RS is approximating something in-between the densities of the two stationary waves and is further approximating the following rarefaction rather well. The result of HLLC+S is most similar to the results of the 1D and 3D models of Rochette et al. [46]. Though HLLC+S reaches the maximum density, its approximation of the following rarefaction is poor. On the other hand, the result of HLLCS is similar to that of Thanh and Kröner's LxF scheme [19] and Brown et al.'s AUSM+-up scheme [31]. All these methods smear the extrema at $x = 0.8$, but capture the rest of the wave structure well. HLLCS also smears the extrema marginally less than the LxF scheme and significantly less than the AUSM+-up scheme.

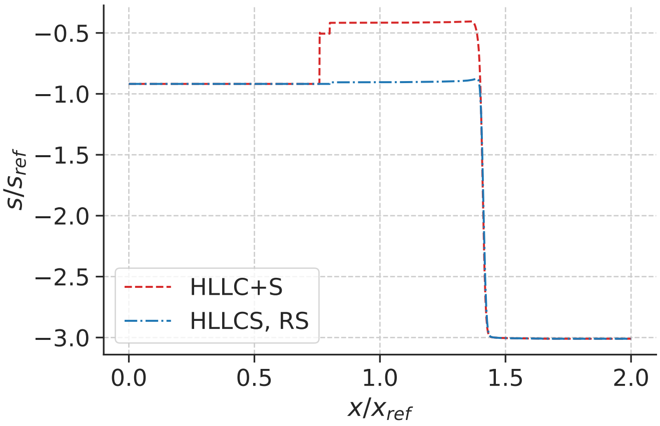

Figure 4.15.: Comparison of HLLC+S' (red dashed line) and HLLCS' (blue dashdotted line) approximation of the specific entropy across the computational domain at $t/t_{\text{ref}} = 0.2$.

Though different numerical results are found for this test in the literature, either similar to the result of HLLC+S or HLLCS, the authors do not comment whether or not their solutions seem physical [46, 19, 31]. We will briefly try to assess which solution is most physical by inspecting the entropy production in the two solutions. The specific entropy for the two schemes HLLC+S and HLLCS at $t/t_{\text{ref}} = 0.2$ is shown in Figure 4.15. Here, HLLC+S has clearly produced more entropy than HLLCS. HLLCS appears to "ignore” the stationary shock at $x = 0.8$, missing the entropy production here. This might suggest that HLLC+S’ result is the most physical, even though it does not approximate the rarefaction after the stationary waves well.

4.2.5. Converging-diverging nozzle tests

It is interesting to explore how HLLC+S and HLLCS perform for smooth nozzles in addition to how they perform on discontinuous problems. For the tests presented below, the following geometry is used

$$A(x) = A_{th} + (A_i - A_{th}) \left(1 - \frac{x}{5}\right)^2 , \tag{4.2}$$

giving a smooth converging-diverging (CD) nozzle where $A_i = 2.035$ is the inlet area and $A_{th} = 1$ is the throat area. Several authors have used this geometry to test their finite-volume methods [47, 48, 49]. The full length of the nozzle is 10 units. An illustration of the geometry is presented in Figure 4.16. HLLC+S and HLLCS with FS have been tested on this nozzle for different inflow Mach numbers and their results compared to the exact solution for ideal gas EOS. In this work, the MATLAB code provided by Hansen in [38], Appendix A.2, for computing the exact solution has been used.

For these tests, the initial condition is given by the left input pressure p_0 and temperature T_0 with $u = 0$, i.e. fluid at rest. For subsonic inflow, we set the stagnation condition in the ghost cell next to the computational domain: p_0, T_0 and $u = 0$, defining the energy available for the flow. This was done to ensure a stable build up to steady-state flow in the nozzle, though it is more common to extrapolate p at the inlet, and setting $u = u_0$ rather than setting the stagnation condition. The common BC method was however found to be unstable for a build-up from fluid at rest, so it must likely be used with a different initial condition. At the outlet, the pressure p_{N_j+1} is set at the ghost cell and all other variables are extrapolated. For supersonic flow, all the variables p, T, u are set at the inflow boundary and extrapolated at the outflow boundary. An overview of the boundary values used for the tests presented below are given in Appendix G.

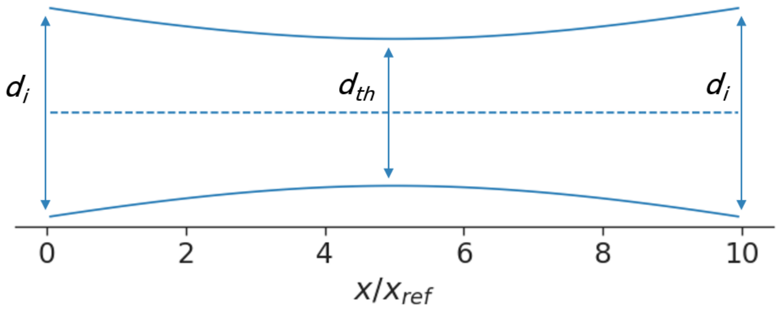

Figure 4.16.: A sketch of the geometry for the converging-diverging nozzle. Here $d_i = 2\sqrt{\frac{A_i}{\pi}}$ and $d_{th} = 2\sqrt{\frac{A_{th}}{\pi}}$ are the diameters of the inlet/outlet areas and the throat area respectively.

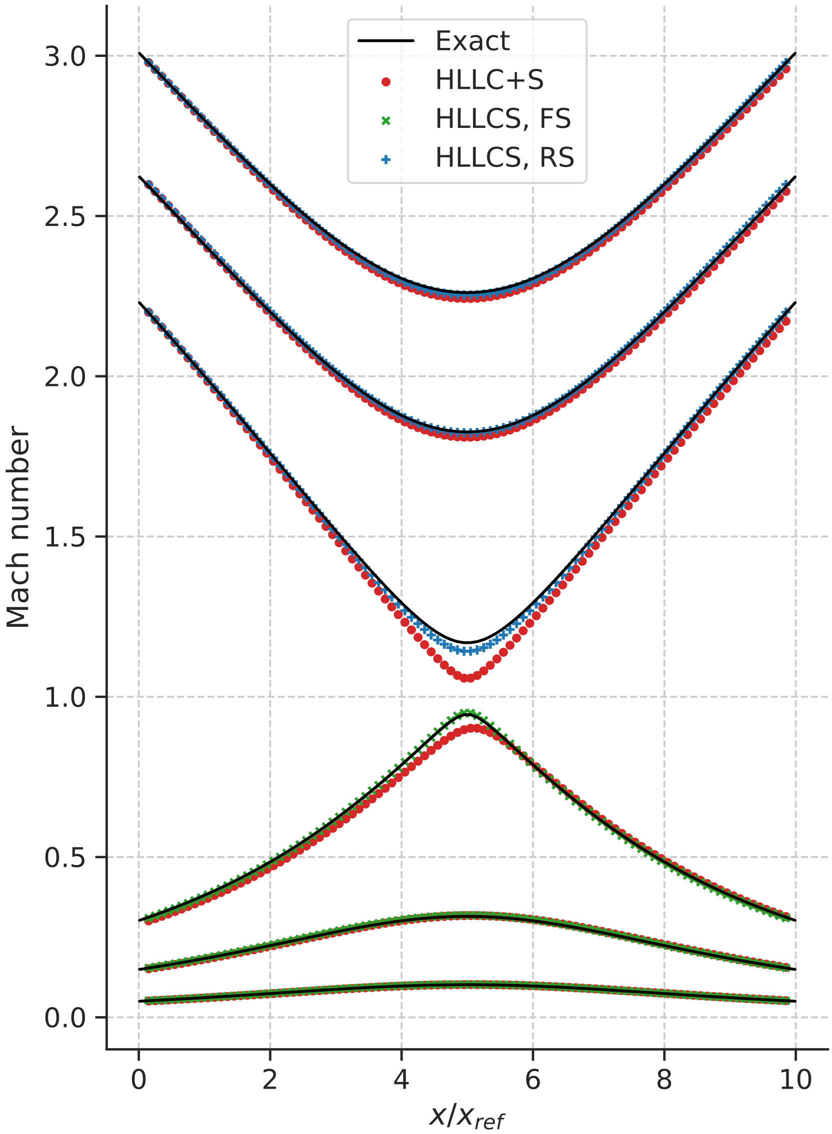

Figure 4.17.: The distribution of Mach number across the converging-diverging nozzle described by Equation (4.2) for HLLC+S (red circles) and HLLCS (green crosses) compared to the exact solution (black line).

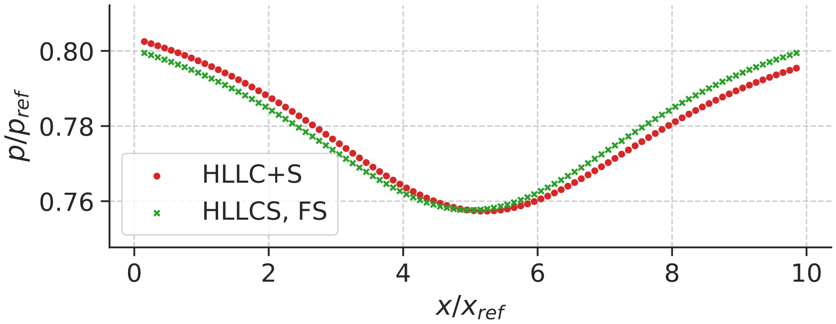

Figure 4.18.: Pressure across the nozzle with an inlet Mach≈ 0.15 for HLLC+S (red circles) and HLLCS with FS (green crosses).

In Figure 4.17 the results of HLLC+S and HLLCS for inlet flows with Mach numbers $0.05, 0.15, 0.3, 2.28, 2.6$ and 3.0 are plotted with the exact solution. HLLC+S and HLLCS produce fairly similar results when the Mach number at the throat of the nozzle is far away from Mach $= 1$. However, when the flow approaches Mach $= 1$, HLLC+S and HLLCS differ much more. HLLCS' result is clearly closer to the exact solution than the result of HLLC+S. In addition, for the case with an inlet Mach number of 0.3, HLLC+S' result is very clearly skewed towards the right with respect to the center of the nozzle. This skewness is also present at other Mach numbers for HLLC+S though it is not quite as obvious. This is not the case for HLLCS. The results found in the literature for this test nozzle are comparable to those achieved by HLLCS. However some skewness can be observed for the schemes presented in the literature as well, an AUSM+-up-based scheme and a modified SIMPLE-type algorithm[47, 48].

We further inspect the simulated pressure and entropy for two inlet Mach numbers, $M = 0.8$ and $M = 2.6$ for HLLC+S and HLLCS. The simulated pressures are presented in Figure 4.18 for $M = 0.8$ and Figure 4.19 for $M = 2.6$. For the subsonic flow, the pressure decreases as the nozzle area decreases and the pressure increases as the nozzle area increases. For the supersonic flow, the opposite happens. This is consistent with theory. Once again, it is clear that HLLC+S' result is skewed. The specific entropy is plotted across the nozzle for HLLC+S and HLLCS in Figures 4.20a and 4.20b for $M = 0.8$ and $M = 2.6$, respectively. Note that we expect constant entropy as the flow is smooth as discussed in Subsection 2.3.4. HLLC+S has a significantly increasing entropy along the nozzle. This can explain the observed skewness of Mach number and pressure across the nozzle for HLLC+S. It appears that the entropy production is greater for greater area change as the specific entropy varies the most at the ends of the nozzle and flattens towards the middle of the nozzle, where the area change $\frac{\mathrm{d}A}{\mathrm{d}x}$ approaches 0.

If we zoom in enough, we can also see small variations in the specific entropy across the pipe for HLLCS with RS. This is shown in Figure 4.20c for an inlet Mach number of 2.6. The variation in specific entropy is symmetric, so there is a clear connection between

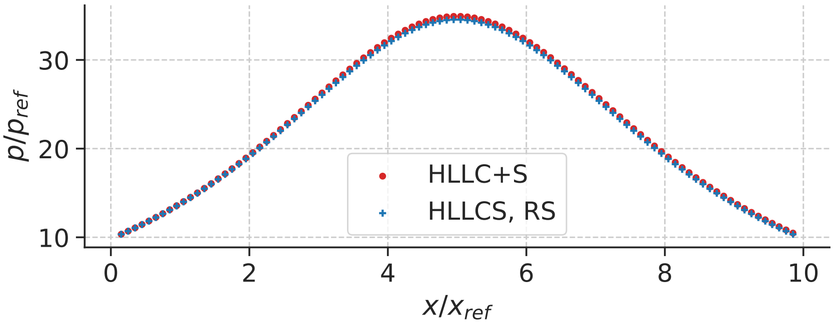

Figure 4.19.: Pressure across the nozzle with an inlet Mach≈ 2.6 for HLLC+S (red circles) and HLLCS with RS (blue plus signs)

the geometry of the nozzle and the error in specific entropy when RS is applied. Note that the entropy is reduced within the geometry and restored and the edges. Though the entropy reduction is very small this is worrying as entropy should always increase or stay constant for such a system an never decrease. For subsonic flow, where HLLCS with FS is used, the variations in entropy are within the error allowed in the Newton solver and are likely caused by rounding errors. This means that for smooth subsonic flow, the entropy is preserved for HLLCS with FS.

The CD nozzle tests show that both HLLC+S and HLLCS perform fairly well for smooth nozzles. HLLCS is more accurate than HLLC+S, especially near Mach = 1. When conducting these test however, different BCs were tested for subsonic flow, where some BCs gave unstable flow. For unstable flow, HLLCS would obtain negative internal energy and the simulation would crash whereas HLLC+S did not have this problem. This suggests that though HLLCS is most accurate, HLLC+S is more robust.

4.2.6. Summary

In this section, a number of benchmark tests with ideal gas EOS have been conducted for the HLLC+S and HLLCS solvers. Recall that HLLCS with FS approximates the source at cell interfaces by RH relations for subsonic flow, using the solution of the nonlinear system derived from the RH relations. We have not derived a similar source term for supersonic flow. HLLCS with RS approximates the source at cell interfaces by the Roe average of the states to the left and right of the interface. Lastly, HLLC+S approximates the contribution of the source at cell centers by the source term defined in Subsection 3.1.4.

We first summarize the results for the non-resonant Riemann problems. Steady-state tests show that only HLLCS with FS is well-balanced, i.e. it conserves the stationary waves exactly. HLLCS with RS and HLLC+S do not conserve the steady-state, but HLLCS with RS is closer than HLLC+S. The straightforward Riemann problem tests further show that HLLC+S is less accurate than HLLCS. HLLC+S does not converge

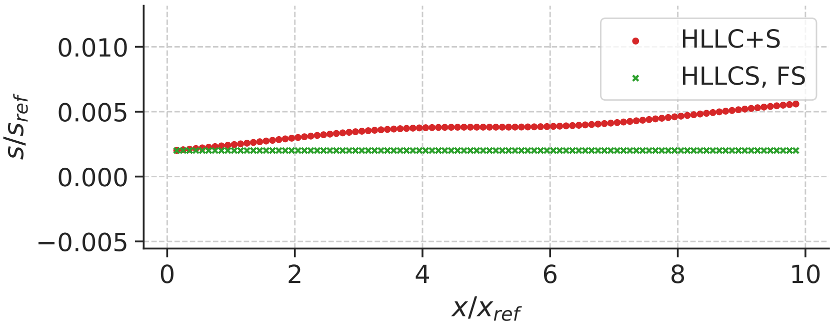

(a) Inlet Mach ≈ 0.15

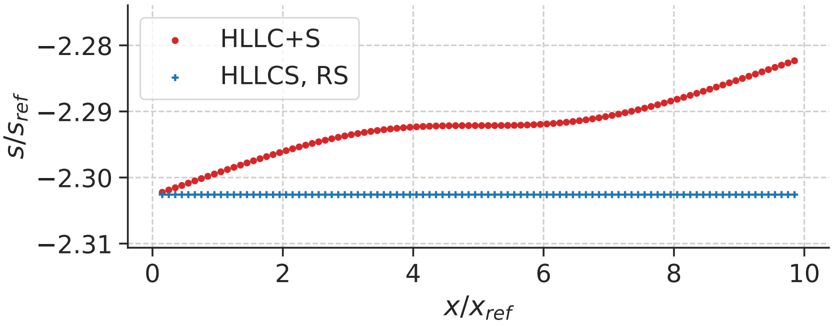

(b) Inlet Mach ≈ 2.6

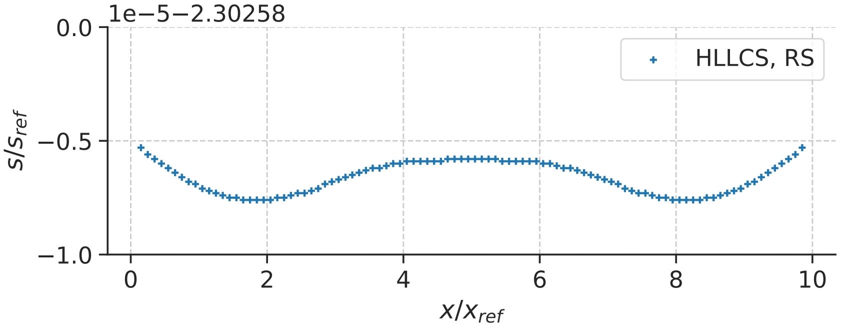

(c) Inlet Mach ≈ 2.6

Figure 4.20.: Plots of simulated specific entropy across the nozzle for an inlet Mach of 0.15 (a) and 2.6 (b), and a zoomed in plot for HLLCS with RS for an inlet Mach of 2.6 (c).

to the exact solution and the error becomes large for strong source terms. Both HLLCS with FS and RS converge to the exact solution, but HLLCS with RS converges slower. For Riemann problems with multiple solutions, it is found that HLLCS with RS can converge to an unphysical solution. This is not found for HLLCS with FS or HLLC+S.

Moving on to resonant cases, i.e. cases where waves resonate with the area change possibly inducing further waves, we find that both HLLC+S and HLLCS with RS can resolve such problems well. HLLCS with FS cannot be applied here. For Test 7, we see once again that HLLCS is more accurate than HLLC+S. For Test 8, HLLC+S and HLLCS approximate different parts of the exact solution and it is unclear which solution is the most correct. The solution involves a stationary shock and entropy production across the shock which HLLCS misses. HLLC+S includes the shock and thus the most entropy production which might suggest that its solution is most physical.

Lastly, HLLC+S and HLLCS were tested for flow in a converging-diverging (CD) nozzle for a range of inlet Mach numbers. For subsonic flow, HLLCS with FS is used since it has been shown to be the most accurate method. HLLCS with RS is used for supersonic flow. We find that HLLCS is once again more accurate than HLLC+S. The exact solution for flow in converging-diverging nozzles has constant entropy. However, HLLC+S has significant entropy production which increases for increasing $\frac{\mathrm{d}A}{\mathrm{d}x}$. HLLCS with RS also has small variations in entropy that are symmetric with respect to the center of the nozzle. Some of the variation involves entropy reduction, this is unphysical and is therefore worrying even though the variations are very small. HLLCS with FS conserves the entropy exactly. Note that we tested some unstable BCs for the CD nozzle and HLLCS would crash for these whereas HLLC+S did not. This indicates that HLLCS is less robust than HLLC+S.

Based on these results, HLLCS with FS is found to be the most promising solver due to its superior accuracy especially for strong source terms. The solver needs, however, extension for supersonic and resonant flow and modification to increase robustness. We list some approaches to achieve this in the section for further work, 5.2.

4.3. Two-phase CO_2 tests for HLLC+S

HLLC+S is implemented for a general EOS, and can readily be tested for two-phase flow. Below, we test HLLC+S for flow in a converging-diverging nozzle, and two Riemann problems suggested by Brown et al. [31] in order to determine whether the method is robust enough to be applied to such problems.

4.3.1. Converging-diverging nozzle tests

In the following, we present three converging-diverging nozzle tests with two-phase CO_2 flow modeled by the HEM with the PR EOS and solved by the HLLC+S method. All the tests have subsonic flow at the inlet. We have chosen the boundary conditions such that we get

Test 9: two-phase flow throughout the nozzle,

Test 10: liquid flow which becomes saturated in the nozzle, and
Test 11: gas flow which becomes saturated in the nozzle.

The purpose of these tests is to investigate both how HLLC+S performs for two-phase flow, and how the HEM models nozzle flow near and on the saturation line for CO_2. The nozzle has the same geometry as for the ideal gas test, given in Equation (4.2), where we now use $A_{th} = 1.0\,\mathrm{cm}^2$, $A_i = 2.035\,\mathrm{cm}^2$, and the length of the nozzle is 10 cm. We use $N_j = 100$ and the same kind of BCs are applied as for the ideal gas tests, i.e. we set the stagnation condition at the inlet ghost cell and the pressure in the outlet ghost cell. The values for the BCs are given in Table 4.12. The stagnation values – $p = p_0, T = T_0, u = 0$ – are used as the initial condition across the domain.

Table 4.12.: Boundary conditions for the two-phase converging-diverging nozzle tests. At the inlet ghost cell $j = 0$, we set the stagnation condition so $u_0 = 0\,\mathrm{ms}^{-1}$ for all cases.

Test	p_0 (MPa)	T_0 (K)	p_{N_j+1} (MPa)
9	9.0	290	3.4
10	20	288	4.5
11	3.0	275	2.5

Test 9

We first present Test 9, which gives two-phase flow throughout the nozzle. In Figures 4.21, 4.22 and 4.23, the steady-state pressure, Mach number and mass fraction of gas found by HLLC+S is plotted. The test gives subsonic two-phase flow which becomes choked at the throat of the nozzle and then becomes supersonic in the diverging part of the nozzle until a shock brings the flow back to subsonic as shown in Figure 4.22. Figure 4.21 shows that the pressure decreases smoothly throughout the nozzle until the shock gives an abrupt pressure-rise. Similarly the amount of gas increases until the shock causes an abrupt decrease, see Figure 4.23. The simulated $p - T$ path of the fluid is shown in Figure 4.24. All the (p, T)-points lie perfectly on the saturation line for the PR EOS.

Results of a similar form for a two-phase converging-diverging nozzle test are found in [50], Case Study 2, where a 7-equation two-phase flow model is applied and strong phase interactions and pressure relaxation are included. The phases are modelled by the stiffened gas EOS. In the case study, there is also subsonic two-phase flow at the inlet, the flow becomes choked at the throat and returns to subsonic by a shock. The steady-state solutions for pressure and mass fraction of gas in [50] have the same general form as we find for the two-phase CO_2 test. The physical modelling in [50] tends to equilibrium conditions, so it is not surprising that the results take a similar form to those produced by the HEM. The similar results further suggest that HLLC+S works well for solving two-phase flow in smooth nozzles with the HEM.

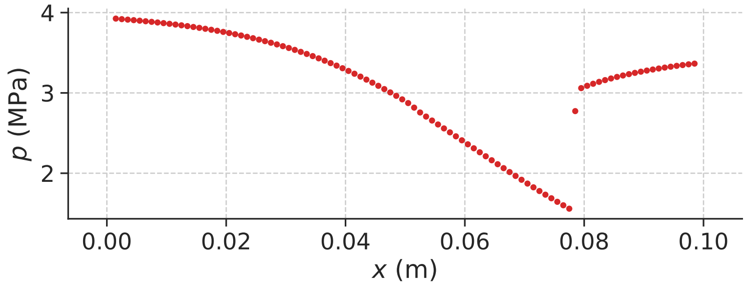

Figure 4.21.: HLLC+S' steady-state pressure solution across the converging-diverging nozzle for Test 9, $N_j = 100$.

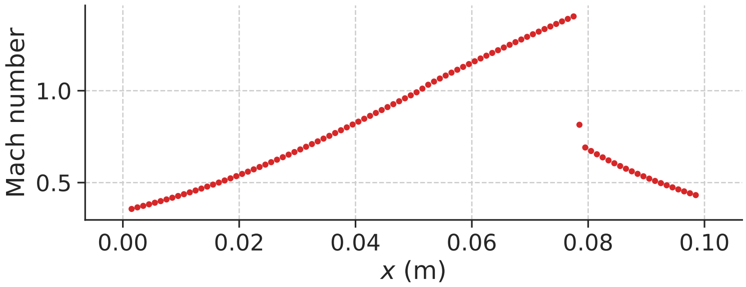

Figure 4.22.: HLLC+S' steady-state Mach number solution across the converging-diverging nozzle for Test 9, $N_j = 100$.

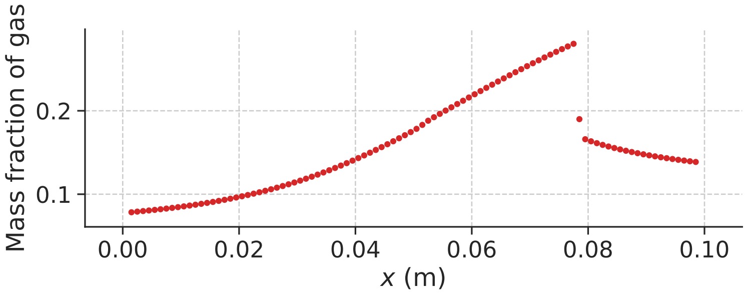

Figure 4.23.: HLLC+S' steady-state solution for the mass fraction of gas across the converging-diverging nozzle for Test 9, $N_j = 100$.

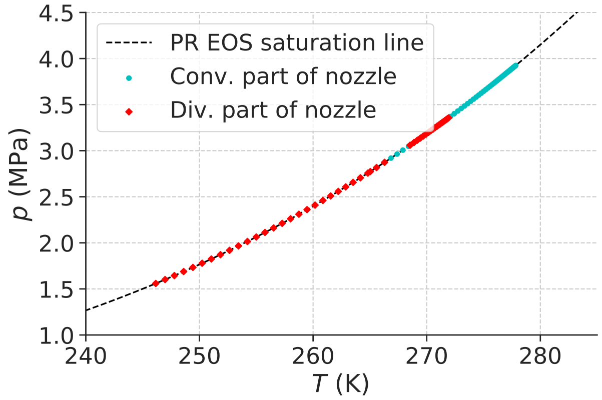

Figure 4.24.: The $p-T$ path of Test 9 for CO_2 flow modeled by the HEM with the PR EOS and solved by the HLLC+S solver.

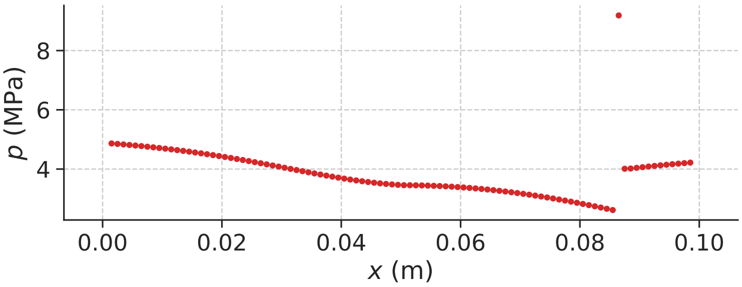

Figure 4.25.: HLLC+S' steady-state solution for the pressure across the converging-diverging nozzle for Test 10, $N_j = 100$.

Test 10

For Test 10 we have liquid flow at the nozzle inlet and the flow reaches saturation within the nozzle. In Figures 4.25, 4.26 and 4.27, HLLC+S' solution for the steady-state pressure, Mach number and mass fraction of gas are plotted. As we see for the Mach number and mass fraction of gas, plotted in Figures 4.26 and 4.27, Test 10 gives subsonic flow until the throat is reached, where the flow becomes two-phase and supersonic. The flow returns to subsonic with a shock. We see for the pressure, plotted in Figure 4.25, that there is an outlier pressure-point just at the shock. Presumably, this is induced by the numerical solver, HLLC+S, and not by the physical modelling as there is no clear reason why the pressure should be so large at just one point. This raises some doubt regarding HLLC+S' accuracy in resolving strong steady shocks. However, the outlier pressure point appears to have little impact on the simulated flow as a whole. The $p-T$ path is shown in Figure 4.28. Once the flow reaches saturation at the throat

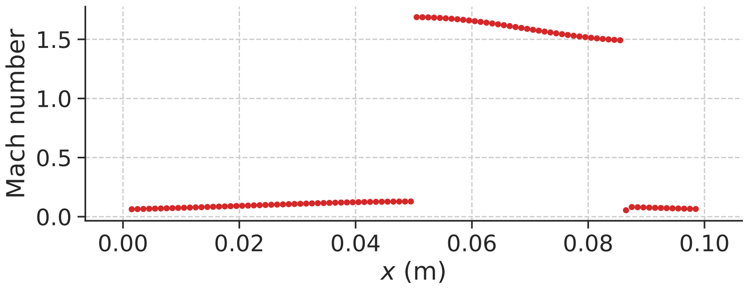

Figure 4.26.: HLLC+S' steady-state solution for the Mach number across the converging-diverging nozzle for Test 10, $N_j = 100$.

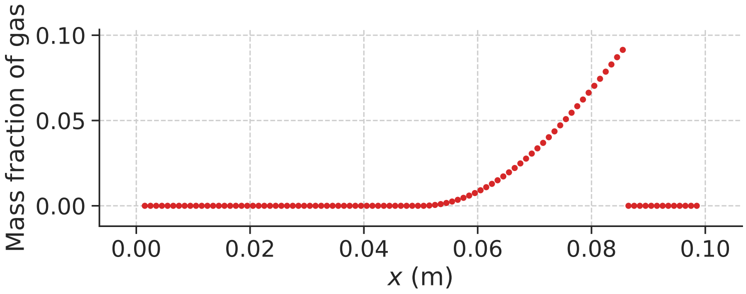

Figure 4.27.: HLLC+S' steady-state solution for the mass fraction of gas across the converging-diverging nozzle for Test 10, $N_j = 100$.

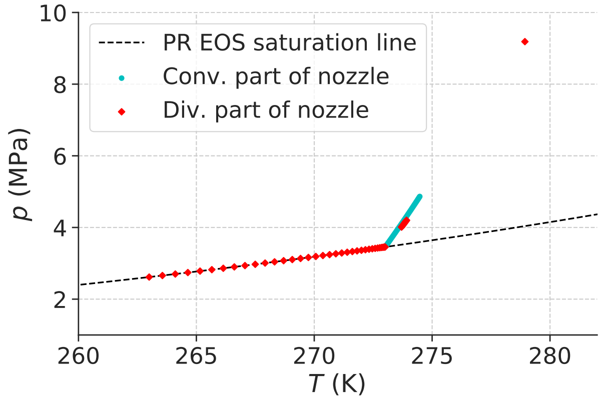

Figure 4.28.: The $p-T$ path of Test 10 for CO_2 flow modeled by the HEM with the PR EOS and solved by the HLLC+S solver.

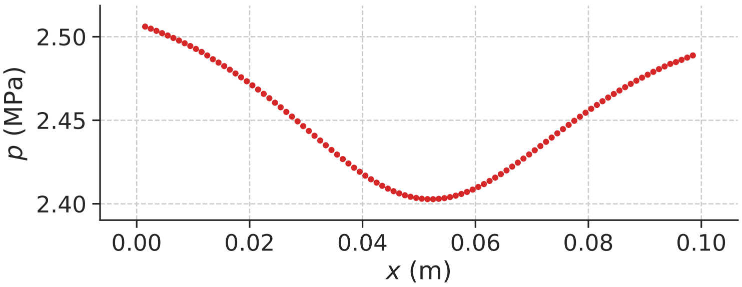

Figure 4.29.: HLLC+S' steady-state solution for the pressure across the converging-diverging nozzle for Test 11, $N_j = 100$.

of the nozzle, the flow follows the saturation line. The shock brings the flow back to single-phase liquid.

Test 11

Finally, we present Test 11 where we have gas flow at the inlet of the nozzle and the flow reaches saturation within the nozzle. In Figures 4.29, 4.30 and 4.31, the HLLC+S solution for the steady-state pressure, Mach number and mass fraction of gas are shown. The flow stays subsonic throughout the nozzle as seen in the plot for the Mach number in Figure 4.30. We see that the flow transitions in and out of the two-phase area in Figure 4.31. This is reflected in the Mach number which is discontinuous at the points of transition. The pressure solution is smooth, and the pressure is not restored at the nozzle outlet due to the phase change along the saturation line, see Figure 4.29. In Figure 4.32, the $p-T$ path for Test 11 is shown. Again, the flow follows the saturation

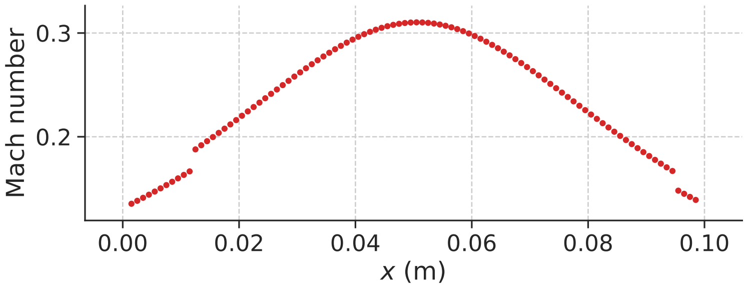

Figure 4.30.: HLLC+S' steady-state solution for the Mach number across the converging-diverging nozzle for Test 11, $N_j = 100$.

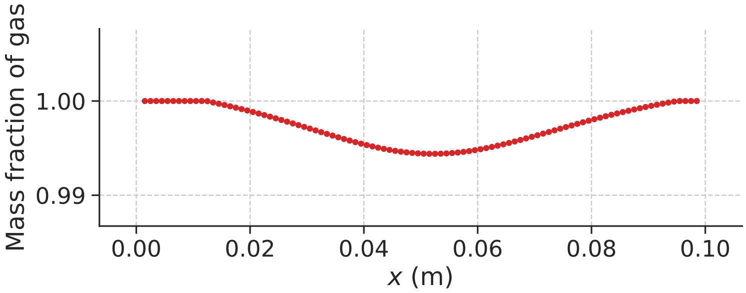

Figure 4.31.: HLLC+S' steady-state solution for the mass fraction of gas across the converging-diverging nozzle for Test 11, $N_j = 100$.

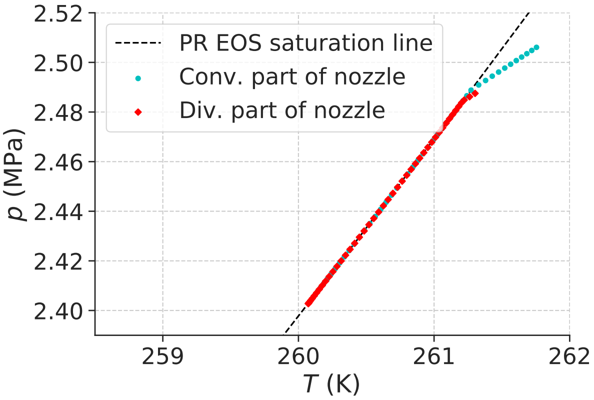

Figure 4.32.: The $p - T$ path of Test 11 for CO_2 flow modeled by the HEM with the PR EOS and solved by the HLLC+S solver.

line once it becomes two-phase.

Remarks on the results

We observe an interesting trend for all the tests: once the flow in the nozzle reaches the saturation line, it becomes “locked” to saturation. The same trend is found by Zanzi [51], see Figure 6.13 therein, for two-phase flow modeled by the HEM in a converging-diverging nozzle, simulated with ANSYS CFX. This “locking” to the saturation line is caused by the equilibrium assumption of the HEM, forcing phase change to keep the flow saturated. If we had single-phase flow, the $p-T$ path in the converging-diverging nozzle would follow a different curve governed by the shape of the nozzle and the boundary conditions, similarly to the flow for ideal gas.

Though the results are consistent with results in the literature where equilibrium [51] or near-equilibrium [50] is imposed for the physical modelling of the system, experiments suggest that the phase-change of CO_2 in nozzles is a nonequilibrium process [51, 52, 53]. Zanzi [51] notes that a simple nonequilibrium model implemented in ANSYS Fluent, the Lee model, fits experimental results better than the HEM. We also see in nozzle experiments that the flow tends to pass the saturation line before condensation or evaporation occurs [52, 53]. This suggests that nonequilibrium models should be applied for two-phase converging-diverging nozzle simulations.

4.3.2. Tests from Brown et al.

We will here conduct similar tests to those presented by Brown et al. in [31] for two-phase flow with the PR EOS and a discontinuous cross-sectional area, Test 12 and Test 13. For Test 12, the same test is also run for the ideal gas EOS and the result of HLLC+S is compared to that of HLLCS with FS to determine how reliable HLLC+S is for resolving such tests.

Test 12

This test is similar to Test 6 presented by Brown et al. [31] for the HEM with the PR EOS and a discontinuous cross-sectional area. The initial conditions for the test is given in Table 4.13, where α_g is the volume fraction of gas. Here, the temperatures and α_g are chosen to match the initial conditions given for the two-phase tests by Brown et al. [31], $p_L = 5\,\mathrm{MPa}$, $p_R = 4\,\mathrm{MPa}$, $\rho_L = 829.1\,\mathrm{kg\,m^{-3}}$, $\rho_R = 126.8\,\mathrm{kg\,m^{-3}}$. We use the same parameters as Brown et al. provide for their test, $x \in [0, 1]\mathrm{m}$, the discontinuity is at $x = 0.6\,\mathrm{m}$, the CFL number is 0.3 and $N_j = 1000$.

Before we show the results of the test, some discussion is needed regarding the initial conditions presented by Brown et al. [31]. Here, they set $\alpha_{g,R} = 0.9$. As two phases are present at the right hand side in the initial condition, the flow must be saturated here. The PR EOS gives a gas density of $116.5\,\mathrm{kg\,m^{-3}}$ and a liquid density of $865.3\,\mathrm{kg\,m^{-3}}$ for

Table 4.13.: Initial conditions for Test 12.

	p (MPa)	u (ms^{-1})	T (K)	A (m^3)	α_g (-)
Left	5	0	283.547	1	0.0
Right	4	0	278.565	0.5	0.986

the saturation pressure of 4 MPa[1]. If we use Brown et al.'s volume fraction, we get that

$$\rho_R = 0.9 \cdot 116.5\,\mathrm{kg\,m^{-3}} + 0.1 \cdot 865.3\,\mathrm{kg\,m^{-3}} = 191.38\,\mathrm{kg\,m^{-3}} \neq 126.8\,\mathrm{kg\,m^{-3}},$$

so their initial condition is inconsistent. $\alpha_{g,R}$ must be ≈ 0.986 to get the density of $\rho_R \approx 126.8\,\mathrm{kg\,m^{-3}}$ as we have set in our initial condition. It seems like there may be some error in Brown et al.'s two-phase implementation, giving $\rho = 126.8\,\mathrm{kg\,m^{-3}}$ for a too low α_g. Due to this error, the results obtained here can only be compared to those of Brown et al. [31] qualitatively.

HLLC+S' solutions for pressure, density, velocity, Mach number, entropy and *mass* fraction of gas are shown in Figures 4.33a, 4.33b, 4.33c, 4.34a, 4.34b and 4.34c, respectively, at the times $t = 0.1$ ms, 0.7 ms and 1.2 ms. Here, earlier times than those shown in Brown et al. [31] were chosen to ensure that the waves stay within the computational domain. Similarly to their results, we get a shock to the right followed by a slower contact-discontinuity and a rarefaction to the left.

The shock can be seen most clearly in the pressure and velocity plots at the positions $x \approx 0.62$ m, $x \approx 0.72$ m, and $x \approx 0.82$ m for the different times. The shock is accompanied with an evaporation jump for the same positions as seen in Figure 4.34c. We see the contact discontinuity in the density plot at the positions $x \approx 0.6$ m, $x \approx 0.605$ m, and $x \approx 0.61$ m. The entropy increases at the contact discontinuity, as it should. There is further evaporation to the left of the area change as can be seen in the mass fraction of gas in $x \in [0.52, 0.6]$m, see Figure 4.34c. Due to this, there is a "splitting" of the rarefaction wave as the pure liquid and liquid-gas mixture have different speeds of sound. We see in the pressure and velocity plots that the pure liquid rarefaction has travelled ≈ 0.56 m reaching $x \approx 0.04$ m, whereas the two-phase rarefaction has only travelled ≈ 0.08 m reaching $x \approx 0.52$ m at $t = 1.2$ ms. The same splitting effect of the rarefaction wave can be observed in the depressurization test presented in Section 4.4. Such a splitting is not present for Brown et al. [31] and their rarefaction appears to travel at the two-phase speed of sound only. Lastly, both HLLC+S and the AUSM+-up scheme in [31] get a spike in the density at $x = 0.6$ m. A spike is also present for the pressure at $x = 0.6$ m.

As no reference solution exists for this problem, we present a convergence study for HLLC+S . In Figures 4.35a, 4.35b and 4.35c we present the pressure, velocity and gas mass fraction solutions obtained at $t = 1$ ms for $N_j = 100$, 500, 1000 and 10000 grid cells. Based on these plots, it seems like the solution of HLLC+S has indeed converged.

---

[1] For reference, the Span-Wagner EOS specifically designed for CO_2 gives $\rho_{\mathrm{sat},g} = 115.7\,\mathrm{kg\,m^{-3}}$ and $\rho_{\mathrm{sat},l} = 894.0\,\mathrm{kg\,m^{-3}}$ for $p_{\mathrm{sat}} = 4$ MPa, where $*_{\mathrm{sat}}$ denotes saturation. This can be found in various online CO_2 calculators. We have used `https://www.peacesoftware.de/einigewerte/co2_e.html`.

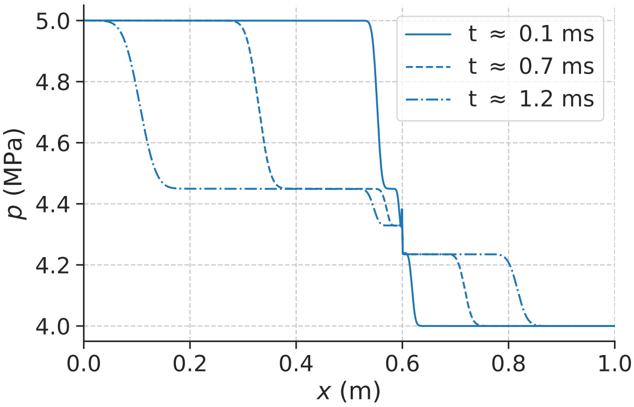

(a) Pressure

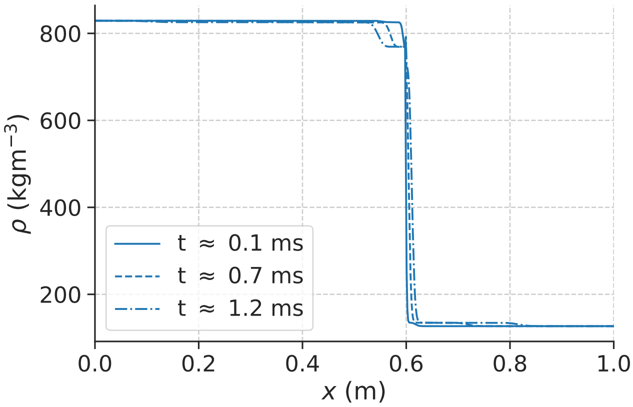

(b) Density

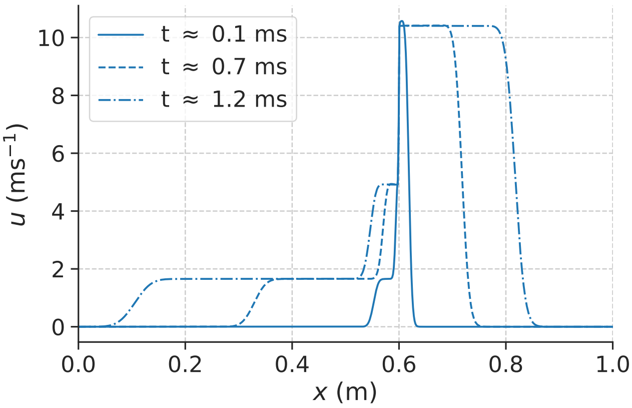

(c) Velocity

Figure 4.33.: HLLC+S' solution for pressure (a), density (b) and velocity (c) for Test 12.

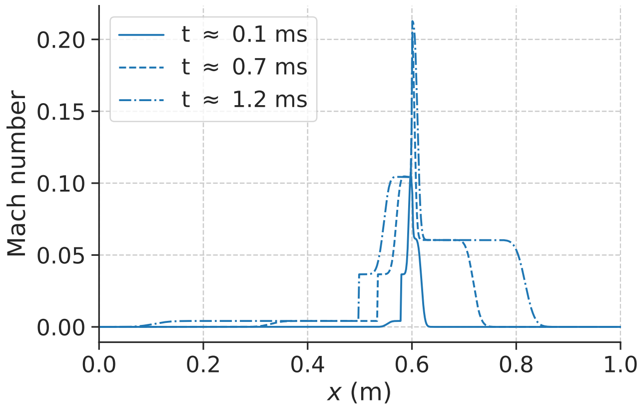

(a) Mach number

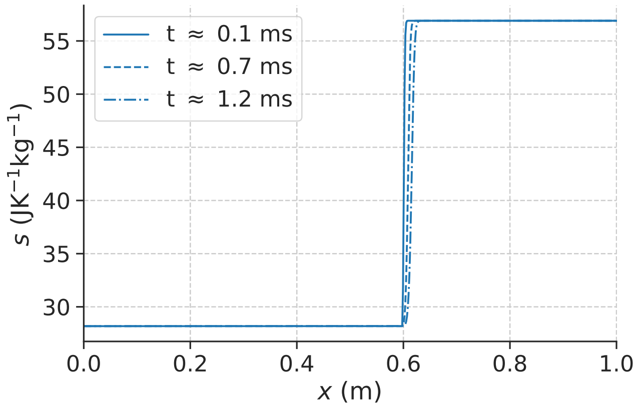

(b) Entropy

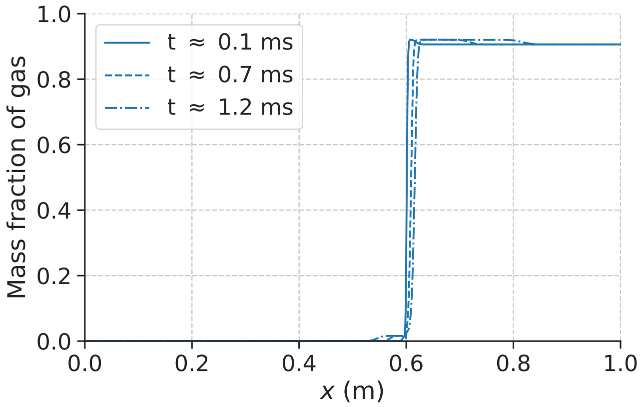

(c) Mass fraction of gas

Figure 4.34.: HLLC+S' solution for Mach number (a), entropy (b) and mass fraction of gas (c) for Test 12.

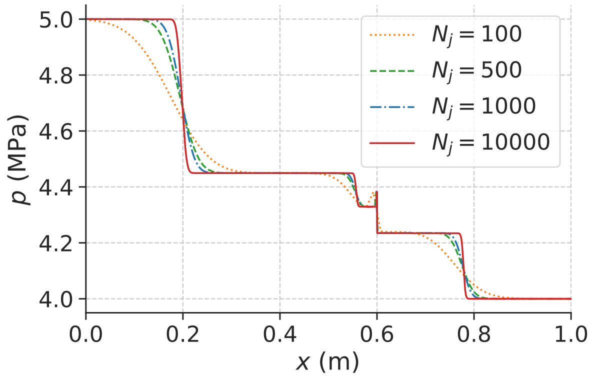

(a) Pressure

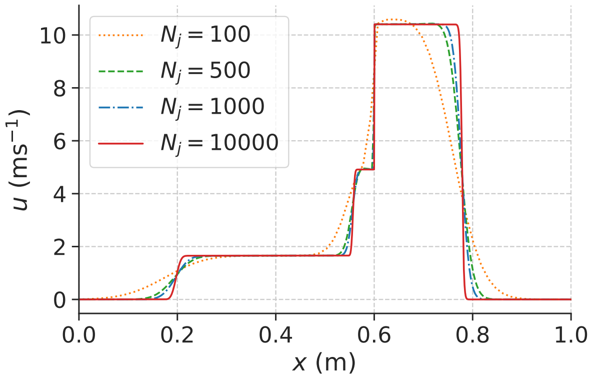

(b) Velocity

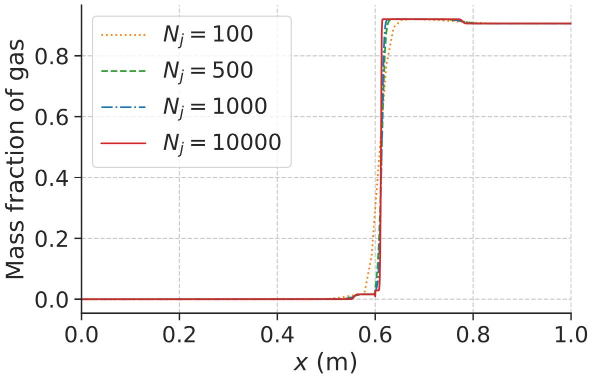

(c) Mass fraction of gas

Figure 4.35.: HLLC+S' solution for pressure (a), velocity (b) and mass fraction of gas (c) at $t = 1\,\text{ms}$ for Test 12 with grid refinement.

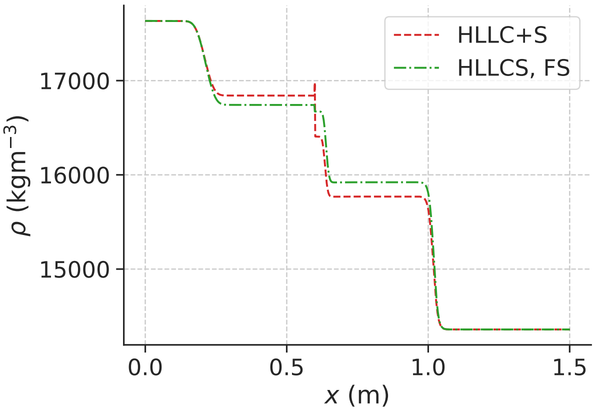

Figure 4.36.: Density solution for HLLC+S (red dashed line) and HLLCS with FS (green dashdotted line) at $t = 0.02\,\mathrm{s}$ for Test 12 with *ideal gas EOS*.

Finally, we study the same test case with ideal gas EOS and compare the solution of HLLC+S to HLLCS' solution in order to see how accurate HLLC+S is for tests like Test 12. In Figure 4.36 the density solution of HLLC+S and HLLCS is shown at $t = 0.02\,\mathrm{s}$ across $x \in [0, 1.5]\mathrm{m}$. Both solutions contain a shock followed by a slow-moving contact discontinuity, the stationary wave across the area change and a rarefaction. Here there is no splitting of the rarefaction wave because we have single-phase flow. The results of HLLC+S and HLLCS differ significantly in the area between the left rarefaction and the right shock. Based on previous results it is likely that HLLCS approximates the exact solution. HLLC+S is likely inaccurate for this test due to the strong source term across the area change.

Note that for both the two-phase test and the ideal gas test, HLLC+S has a spike in its density near the area change. HLLCS does not have this for the ideal gas test. The test case is somewhat similar to the strong source Riemann test in Subsection 4.2.2. Here HLLC+S has a spike in its pressure solution at the area change, whereas the exact solution and HLLCS' solution does not have a spike. This suggests that the two-phase test should not have a spike in its density or pressure either. The AUSM+-up scheme also gives a spike for the test run by Brown et al. [31], suggesting that neither HLLC+S nor AUSM+-up are very accurate for cases like Test 12.

Test 13

Brown et al. [31] also introduce a test to investigate the interaction of a shock wave with a cross-sectional area reduction for two-phase flow. The initial condition for this test is given in Table 4.14. The initial condition is similar to that of Test 12, but the area change occurs now at $x = 0.9\,\mathrm{m}$ instead of $x = 0.6\,\mathrm{m}$. Once again we use the same number of grid cells and CFL number as Brown et al. [31], $N_j = 1000$ and $C = 0.3$. The computational domain for the test is within $x \in [0, 1.5]\mathrm{m}$.

Table 4.14.: Initial conditions for Test 13.

	p (MPa)	u (ms^{-1})	T (K)	A (m^3)	α_g (-)
$x < 0.6\,\mathrm{m}$	5	0	283.547	1	0.0
$0.6\,\mathrm{m} < x < 0.9\,\mathrm{m}$	4	0	278.565	1	0.986
$x > 0.9\,\mathrm{m}$	4	0	278.565	0.5	0.986

The HLLC+S solution for pressure, density, velocity, Mach number, entropy, and mass fraction of gas are shown in Figures 4.37a, 4.37b, 4.37c, 4.38a, 4.38b, and 4.38c, respectively, for the times 1.5 ms, 2.0 ms and 2.5 ms. For this test the pure liquid rarefaction moves out of the domain just as the shock reaches the area reduction at $t = 1.5\,\mathrm{ms}$. We can see clearly from the pressure plot in Figure 4.37a that the shock is partially reflected and partially transmitted. The reflection causes a significant decrease in the fluid speed to the left of the area change as seen in Figure 4.37c. There is also some increase in the amount of vapour for the reflected shock as shown in Figure 4.38c. Brown et al. [31] get similar behaviour for their test.

Once again there is a peak for the pressure and density of the fluid at the area change, though this is easiest to spot for the pressure. We suspect that this is introduced by the inaccuracy of the HLLC+S scheme across the area change. HLLC+S also introduces a bump in the pressure and velocity solutions to the right of the shock. We would expect the pressure and velocity to be constant here. The bump is likely caused by HLLC+S' poor resolution of the stationary state, giving a fictitious wave travelling to the right. This effect is not seen for the AUSM+-up scheme.

4.3.3. Summary

In this section, two-phase tests have been conducted for HLLC+S with the HEM and the Peng-Robinson EOS. We have conducted simulations for two-phase CO_2 flow in a converging-diverging nozzle and studied two Riemann problems suggested by Brown et al [31].

The results for the converging-diverging nozzle test shows that HLLC+S can resolve the two-phase flow with the HEM fairly well. However we see an odd peak for one of the simulations which includes a strong steady shock in the nozzle. We suspect the peak comes from an inaccuracy of the HLLC+S method. We observe that the flow follows the saturation line once it becomes two-phase within the nozzle for the HEM.

We have further attempted to recreate the two two-phase tests presented in Brown et al. [31], Test 12 and Test 13. We provide initial conditions for the tests which give similar initial states as those Brown et al. give for their tests. The tests show that HLLC+S is robust enough to be used for two-phase flow with large cross-sectional area changes. In both Test 12 and Test 13, it is suspected that HLLC+S provides a somewhat inaccurate solution, however. This is due to the presence of a peak in the pressure and density for the solution of both test cases.

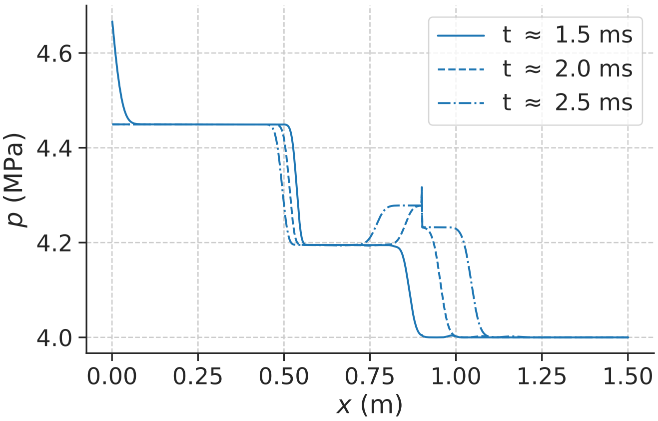

(a) Pressure

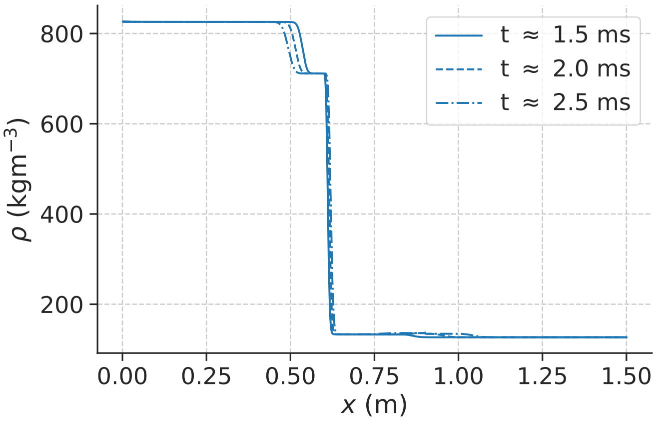

(b) Density

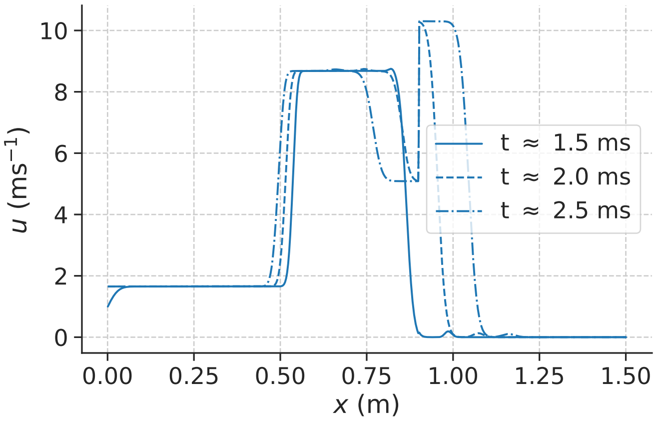

(c) Velocity

Figure 4.37.: HLLC+S' solution for pressure (a), density (b) and velocity (c) for Test 13.

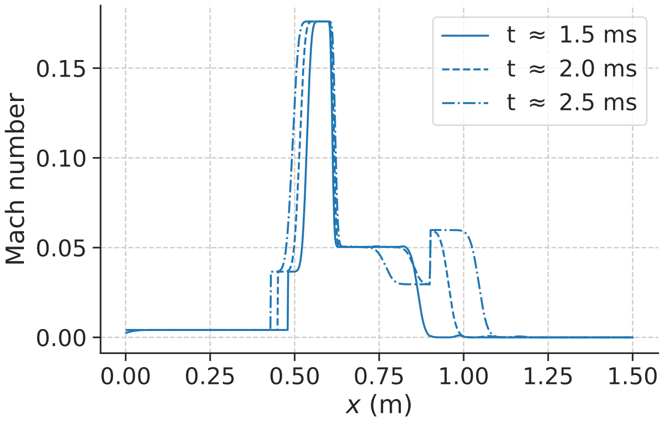

(a) Mach number

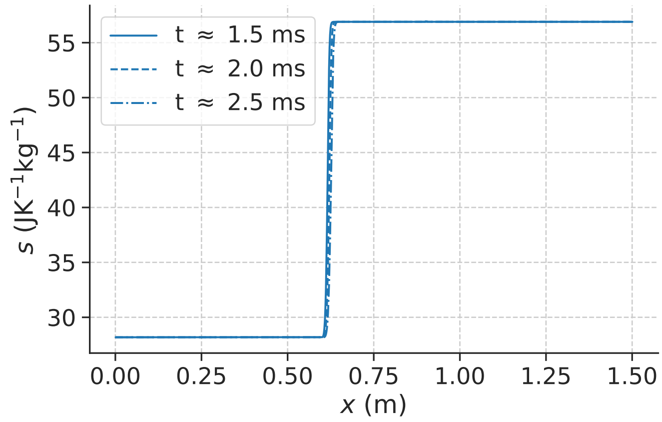

(b) Entropy

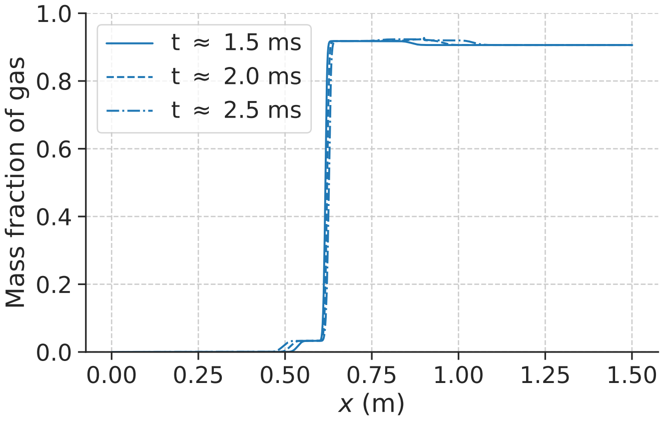

(c) Mass fraction of gas

Figure 4.38.: HLLC+S' solution for Mach number (a), entropy (b) and mass fraction of gas (c) for Test 13.

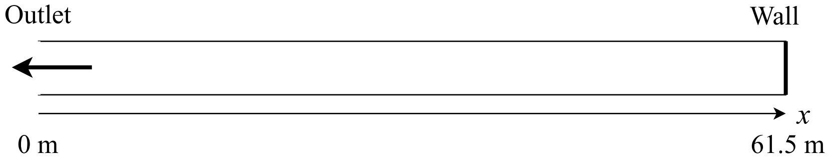

Figure 4.39.: Sketch of the system being simulated.

When Test 12 is run with the ideal gas EOS, HLLC+S again gives a peak in the density, whereas HLLCS does not. As HLLCS is more accurate than HLLC+S, we assume that this peak should not be present in the solution. Brown's AUSM+-up scheme also gives a peak in their test, suggesting that this solver has a similar error as HLLC+S. For Test 13 there is also a bump in the solution where the flow should be uniform. We suspect this is caused by HLLC+S not being well-balanced, such that a fictitious wave is created across the area change for steady-state flow.

4.4. Test of boundary conditions for the Euler equations: full-bore depressurization

In this section, numerical results for a full-bore depressurization to ambient air of a pipe with high-density liquid CO_2 are presented for Lax Friedrichs (LxF) and HLLC. For the simulations, the HEM is used with the Peng-Robinson (PR) EOS. The three different BCs for subsonic flow outlined in Section 3.2 are tested for both methods and the results are compared to experimental data provided by SINTEF Energy Research [12].

4.4.1. Depressurization setup and results

The experimental data is measured at SINTEF Energy Research's newly built experiment rig for pipe depressurization of CO_2 [54]. This facility is part of the European Carbon Dioxide Capture and Storage Laboratory Infrastructure (ECCSEL). The rig has a pipe with a rupture disk at one end and a solid wall at the other end. When the disk separating the high-pressure CO_2 from the ambient air is ruptured, the depressurization experiment starts.

In Figure 4.39, the layout of the pipe is sketched. $x = 0$ is set at the position of the rupture disk and the positions of pressure sensors are measured by their distance from

Table 4.15.: Initial conditions for the full-scale depressurization test, inside the pipe and outside.

	p (MPa)	u (ms^{-1})	T (K)	α_g (-)
Inside	125	0	295	0
Outside	1	0	295	1

the disk. We therefore get flow in the negative x-direction. The initial condition for the test is presented in Table 4.15.

The results of numerical simulations for pressure across the pipe at $t = 0.05\,\mathrm{s}$ are plotted with SINTEF's experimental pressure measurements in Figures 4.40a and 4.40b for LxF and HLLC respectively. We see for both methods that the results agree fairly well with the experimental data, validating both the two-phase modelling in general and the wave-speed estimate for HLLC given in Subsection 3.1.9. The good agreement with experimental data suggests that the phases are indeed well-mixed in the depressurization such that the HEM performs well. The experimental pressure point at $x = 20\,\mathrm{m}$ suggests that there should be a positive slope to the pressure in the approximate area $x \in [10, 20]$m, where both LxF and HLLC give a flat plateau, however. Effects which we have omitted in the physical modelling such as friction and heat conduction from the pipe wall would likely give a pressure increase as we see in the experimental data. More accurate results will likely also be achieved by applying the Span-Wagner EOS, [55] which is specifically designed for CO_2, instead of the PR EOS.

We will now investigate the results of each method more closely. For LxF, the result shows that the different BCs perform fairly similarly, with the Characteristic BC providing the result closest to the experimental data. For HLLC, the resulting pressure for the different BCs are practically overlapping with the exception of a much lower pressure at the first grid cell in the domain for the Naive BC than for the other BCs. One may note that HLLC has a sharper transition in the pressure near the pipe outlet ($x = 0\,\mathrm{m}$) than what is found experimentally. LxF appears to fit the experimental data better. HLLC has little numerical dissipation [35, 45], whereas LxF is a very dissipative method. It seems like the numerical dissipation added by LxF happens to “correct” to some extent the physical modelling lacking dissipation from friction and heat conduction. When the grid for LxF is refined to 5000 grid cells, it also obtains a sharper transition in the pressure than what is found experimentally, as shown in Figure 4.41.

We further assess the results for LxF and HLLC with different BCs by comparing their Mach numbers across the pipe. The flow should be subsonic within the pipe and choked at the pipe outlet. The simulated Mach number at $t = 0.05\,\mathrm{s}$ is plotted for $x \in [0, 40]$m for LxF and HLLC with the different BCs in Figures 4.42a and 4.42b, respectively. Note first that the sudden fall in Mach number for LxF and HLLC, near $x = 10\,\mathrm{m}$ for LxF and $x = 5\,\mathrm{m}$ for HLLC, indicates the transition from two-phase to liquid flow, and the positions differ as LxF spreads the phases out more due to its dissipative nature.

All the BCs perform similarly for the Mach number within the pipe where the flow is indeed subsonic. The outlet Mach numbers vary, however. For LxF there is supersonic flow in the first $2 - 3$ grid cells near the outlet at $x = 0\,\mathrm{m}$ for both the Bernoulli BC and the Naive BC. The Characteristic BC gives choked flow. For HLLC there is only supersonic flow in the first grid cell with the Naive BC, otherwise the flow is choked. Interestingly, the Naive BC performs worse when applied with HLLC than with LxF. For future simulation purposes the Characteristic BC should be applied if the flow near and at the outlet is of interest, but otherwise all BCs can be applied for flow within the pipe.

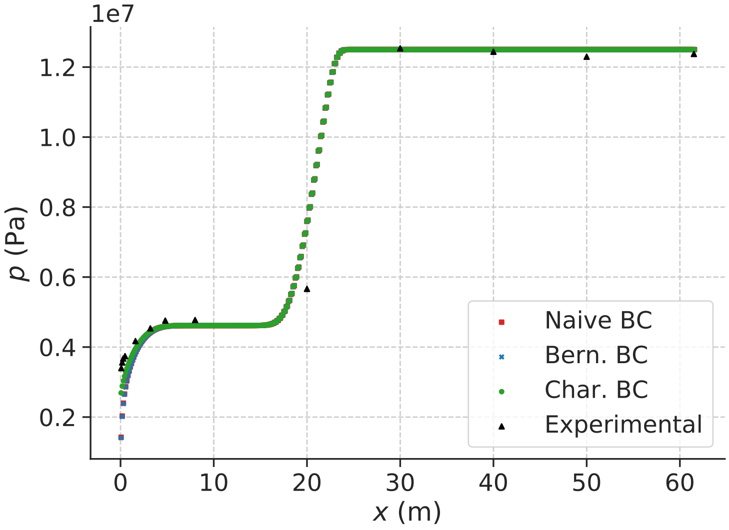

(a) LxF

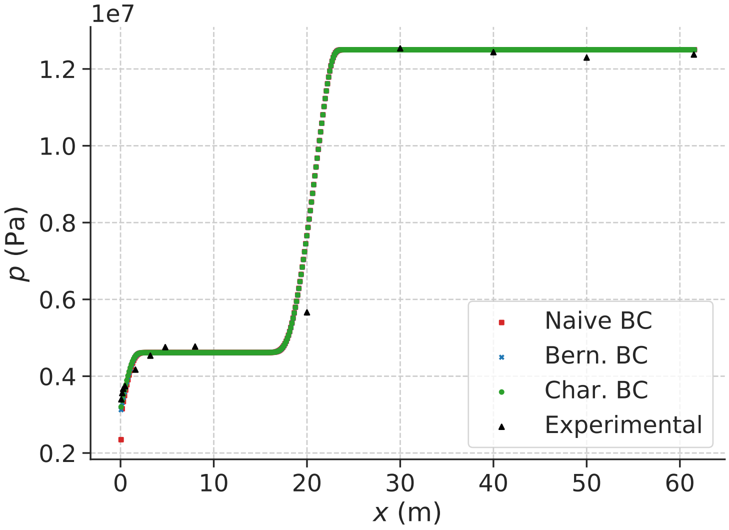

(b) HLLC

Figure 4.40.: Simulated results using LxF (a) and HLLC (b) on the HEM with the PR EOS and three different BCs as outlined in Section 3.2, $N_j = 500$ and $t = 0.05\,\mathrm{s}$. The results are compared to experimental data provided by SINTEF Energy Research.

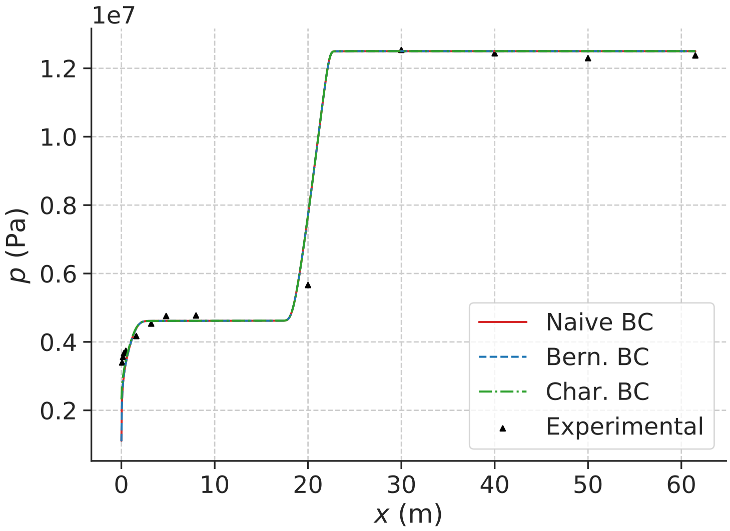

Figure 4.41.: Simulated results using LxF on the HEM with the PR EOS and three different BCs as outlined in Section 3.2, $N_j = 5000$ and $t = 0.05\,\text{s}$. The results are compared to experimental data provided by SINTEF Energy Research.

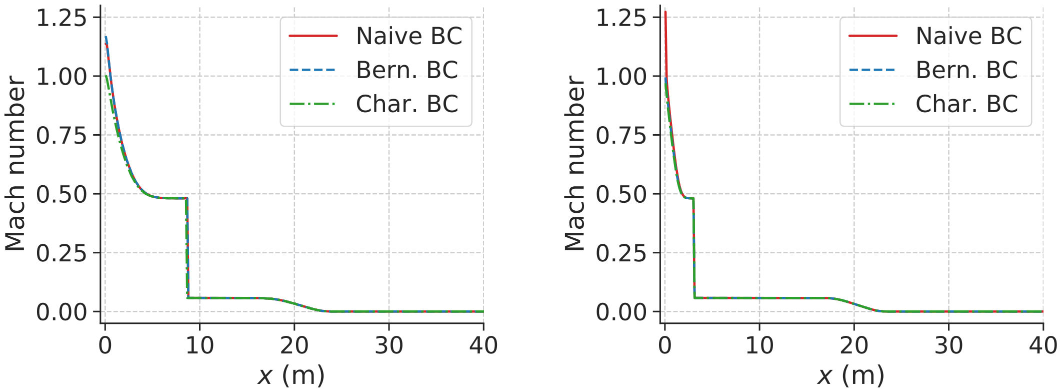

(a) LxF

(b) HLLC

Figure 4.42.: Simulated Mach number across the pipe using LxF (a) and HLLC (b) on the HEM with PR EOS and three different BCs for subsonic flow as outlined in Section 3.2. $N_j = 500$ and $t = 0.05\,\text{s}$.

4.4.2. Summary

A depressurization test has been conducted to validate the modelling of the CO_2 flow in pipes with LxF and HLLC on the HEM with the PR EOS, and to test different BCs. The simulated results agree with experimental data, and differences can be attributed to the physical modelling omitting friction and thermal conduction from the pipe walls. The agreement with experimental results further validates the Roe average wave speed estimate for the Euler equations presented in Subsection 3.1.9.

For the depressurization simulations, three outflow BCs were tested, the Naive BC, the Bernoulli BC and the Characteristic BC. The Characteristic BC was found to be the most accurate, reaching choked flow at the outlet for both HLLC and LxF. The Bernoulli BC gives choked flow at the outlet for HLLC, but not for LxF, and the Naive BC reaches supersonic flow at the outlet for both methods. All the BCs give similar results for the flow within the pipe.

5. Conclusions and further work

5.1. Summary and conclusions

In this work, the HLLC method has been extended for flow in pipes with varying cross-sectional area, and the two proposed methods, HLLC+S and HLLCS, have been applied to a range of benchmark tests with the ideal gas EOS. HLLC+S has also been tested for two-phase CO_2 flow with the PR EOS and the HEM on a converging-diverging nozzle and two tests proposed by Brown et al [31]. Lastly, LxF and HLLC have been tested with different outflow BCs for the simulation of a full-bore CO_2 pipe depressurization.

Flow in pipes with varying cross-sectional area

The FVMs HLLC+S and HLLCS have been proposed to solve flow in pipes with varying cross-sectional area. HLLC+S simply adds a source term to the well-known HLLC method, whereas HLLCS is a new approximate Riemann solver including the additional stationary wave accounting for the source term present.

HLLC+S is found to be the least accurate method. As found from tests with the ideal gas EOS, the solver is not well-balanced, i.e. it does not conserve the steady-state. Furthermore, the solver does not converge to the exact solution for discontinuous area change and its error becomes large for strong source terms. For sufficiently small source terms, HLLC+S can be applied for straightforward problems in addition to problems with resonance and non-uniqueness, so it has valuable generality. HLLC+S is also tested for two-phase CO_2 flow in a converging-diverging nozzle and for tests suggested by Brown et al. [31]. The tests indicate that HLLC+S is robust enough for two-phase simulations, though its results are likely somewhat inaccurate for sharp area changes. Simulations of two-phase flow with the HEM in converging-diverging nozzles are consistent with results in the literature where equilibrium [51] or near-equilibrium [50] is imposed. We observe, for the HEM, that when the fluid reaches saturation within the nozzle, the pressure and temperature follows the saturation line.

HLLCS has been tested with two possible source terms, the Roe average-based source term (RS) and the flux-based source term (FS). FS is based on subsonic flow and is not used for supersonic flow. HLLCS assumes a specific wave structure for the problem and requires the solution of a nonlinear system for subsonic flow. It is found that the system usually has two solutions for ideal gas. However, the system does not have a solution for resonant problems, where HLLCS' assumption of the wave structure is incorrect. FS requires the solution of this system to give a good estimate of the source term. Therefore, HLLCS with FS cannot be used for resonant problems.

Results from the benchmark tests with ideal gas EOS show that HLLCS with FS has superior accuracy for non-resonant, subsonic flow. The solver is well-balanced, handles strong source terms and chooses the physical solutions for the non-unique Riemann problems tested. For tests with supersonic and resonant flow, HLLCS with RS performs well and is more accurate than HLLC+S. We note, however, that HLLCS with RS finds the unphysical solution for one of the non-unique Riemann problems tested.

The results are promising and suggest that the HLLCS solver should be extended for two-phase flow due to its superior accuracy. HLLCS in its current form is, however, not general nor very robust due to the nonlinear system for subsonic flow, which can have multiple or zero solutions. This can be improved upon as we will come back to in the suggestions for further work.

Depressurization test

LxF and HLLC have been tested for the simulation of a CO_2 pipe depressurization. For the simulations, the PR EOS with the HEM was used. Three different outflow BCs were tested for the simulations: the Naive BC, the Bernoulli BC and the Characteristic BC. All the BCs gave similar results for the flow within the pipe, but different flow just at the pipe outlet. The Characteristic BC is most accurate at the outlet, as expected. The simulations agree with experimental data, and differences can be explained by the physical model in the simulation lacking friction and thermal conduction from the pipe walls. The agreement suggests that the phases are well-mixed during the depressurization, and that the wavespeed estimate for HLLC works well.

5.2. Suggestions for further work

- An FS-type source term for HLLCS can be derived for supersonic flow as well, using Rankine-Hugoniot conditions similarly to the approach for subsonic flow. Then, the well-balanced property achieved for subsonic flow for HLLCS with FS can likely be extended for supersonic flow as well.
- A condition can be determined to recognize resonant flow in the HLLCS solver. If resonant flow is found, RS can be automatically applied and the same HLLCS algorithm can be applied for resonant and non-resonant problems alike.
- A linearization of the HLLCS solver can be investigated to remove the unpredictable factor of the nonlinear system for subsonic flow. This may make the solver more general, efficient and robust. Then, special considerations will likely not be needed for resonant cases.
- HLLCS can be extended for a general EOS and tested for two-phase flow. Even if HLLCS is found to not be robust enough for tough cases with two-phase flow, it can likely still be used as a reference for less tough cases to check the accuracy of other, more robust methods.
- Different discretizations of the source term in HLLC+S, which is already a general and robust method, can be explored to increase the method's accuracy.
- Nonequilibrium models can be explored for the two-phase flow of CO_2 in nozzles. This will likely increase the accuracy of nozzle simulations, since experimental results from the literature suggest that the phase-change in nozzles is a nonequilibrium process, as noted in Subsection 4.3.1.

Bibliography

[1] V. Masson-Delmotte, P. Zhai, H. O. Pörtner, D. Roberts, J. Skea, P. R. Shukla, A. Pirani, W. Moufouma-Okia, C. Péan, R. Pidcock, S. Connors, J. B. R. Matthews, Y. Chen, X. Zhou, M. I. Gomis, E. Lonnoy, T. Maycock, M. Tignor, and T. Waterfield (eds.). Global Warming of 1.5°C.An IPCC Special Report on the impacts of global warming of 1.5°C above pre-industrial levels and related global greenhouse gas emission pathways, in the context of strengthening the global response to the threat of climate change, sustainable development, and efforts to eradicate poverty. Technical report, IPCC, 2018.

[2] B. Metz, O. Davidson, H. C. de Coninck, M. Loos, and L. A. Meyer (eds.). IPCC Special Report on Carbon Dioxide Capture and Storage. Technical report, IPCC, 2005. URL `https://www.ipcc.ch/site/assets/uploads/2018/03/srccs_wholereport-1.pdf`. Prepared by Working Group III of the Intergovernmental Panel on Climate Change.

[3] J. Tosun, S. Biesenbender, and K. Schulze (Eds.). *Energy Policy Making in the EU - Building the Agenda, Chapter 11.4*. Springer, Munich, 2015.

[4] The Norwegian Ministry of Petroleum and Energy. Capture, transport and storage of CO_2. URL `https://www.regjeringen.no/en/topics/energy/carbon-capture-and-storage/capture-transport-and-storage-of-co2/id443518/`. Accessed 31.05.2020.

[5] Northern lights - A European CO_2 transport and storage network. URL `https://northernlightsccs.com/`. Accessed 30.05.2020.

[6] H. Mahgerefteh, S. Brown, and G. Denton. Modelling the impact of stream impurities on ductile fractures in CO_2 pipelines. *Chem. Eng. Sci.*, 74:200–210, 05 2012. doi: 10.1016/j.ces.2012.02.037. URL `https://doi.org/10.1016/j.ces.2012.02.037`.

[7] E. Aursand, C. Dørum, M. Hammer, A. Morin, S. T. Munkejord, and H. O. Nordhagen. CO_2 pipeline integrity: comparison of a coupled fluid-structure model and uncoupled two-curve methods. *Energy Proc.*, 51:382–391, 2014. doi: 10.1016/j.egypro.2014.07.045. URL `https://doi.org/10.1016/j.egypro.2014.07.045`.

[8] X. K. Zhu. State-of-the-art review of fracture control technology for modern and vintage gas transmission pipelines. *Eng. Fract. Mech.*, 148:260–280, 11 2015. doi: 10.1016/j.engfracmech.2015.05.055. URL `https://doi.org/10.1016/j.engfracmech.2015.05.055`.

[9] M. D. Biagio, A. Lucci, E. Mecozzi, and C. M. Spinelli. Fracture Propagation Prevention on CO_2 Pipelines: Full Scale Experimental Testing and Verification Approach, 2017. URL `https://www.eprg.net/fileadmin/EPRG_public/eprg-docs/papers/2017_-_3R_-Di_Biagio_et_al_-_Fracture_in_CO2_Pipelines.pdf`. Berlin.

[10] P. Aursand, M. Hammer, S. T. Munkejord, and Ø. Wilhemsen. Pipeline transport of CO_2 mixtures: Models for transient simulation. *Int. J. Greenh. Gas Con.*, 15: 174–185, 07 2013. doi: 10.1016/j.ijggc.2013.02.012. URL `https://doi.org/10.1016/j.ijggc.2013.02.012`.

[11] S. T. Munkejord and M. Hammer. Depressurization of CO_2-rich mixtures in pipes: Two phase flow modelling and comparison with experiments. *Int. J. Greenh. Gas Con.*, 37:398–411, 03 2015. doi: 10.1016/j.ijggc.2015.03.029. URL `https://doi.org/10.1016/j.ijggc.2015.03.029`.

[12] S. T. Munkejord, A. Austegard, H. Deng, M. Hammer, H. G. J. Stang, and S. W. Løvseth. Depressurization of CO_2 in a pipe: High-resolution pressure and temperature data and comparison with model predictions. Submitted, 2020.

[13] A. M. Log. Investigation of the HLLC finite volume method for one- and two-phase flow with a general equation of state, 2019. 9th semester project report, NTNU.

[14] E. F. Toro, M. Spruce, and W. Speares. Restoration of the contact surface in the HLL-Riemann solver. *Shock Waves*, 4(1):25—-34, 1994. doi: 10.1007/BF01414629. URL `https://doi.org/10.1007/BF01414629`.

[15] E. F. Toro and S. Billett. Centred TVD schemes for hyperbolic conservation laws. *IMA Journal of Numerical Analysis*, 20(1):47–79, 2000. doi: 10.1093/imanum/20.1.47. URL `https://doi.org/10.1093/imanum/20.1.47`.

[16] S. T. Munkejord, C. Bernstone, S. Clausen, G. de Koeijer, and M. J. Mølnvik. Combining Thermodynamic and Fluid Flow Modelling for CO_2 Flow Assurance. *Energy Procedia*, 37:2904–2013, 2013. doi: 10.1016/j.egypro.2013.06.17. URL `https://doi.org/10.1016/j.egypro.2013.06.176`.

[17] J. Hetland, J. Barnett, A. Read, J. Zapatero, and J. Veltin. CO_2 Transport Systems Development: Status of Three Large European CCS Demonstration Projects with EEPR Funding. *Energy Procedia*, 63:2458–2466, 2014. doi: 10.1016/j.egypro.2013.06.17. URL `https://doi.org/10.1016/j.egypro.2013.06.176`.

[18] N. Andrianov and G. Warnecke. On the Solution to The Riemann Problem for the Compressible Duct Flow. *SIAM J. Appl. Math*, 64(3):878–901, 2004. doi: 10.1137/S0036139903424230. URL `https://doi.org/10.1137/S0036139903424230`.

[19] M. D. Thanh and D. Kröner. Numerical treatment of nonconservative terms in resonant regime for fluid flows in a nozzle with variable cross-section. *Comp. &*

Fluids, 66(15):130—-139, 2012. doi: 10.1016/j.compfluid.2012.06.021. URL `https://doi.org/10.1016/j.compfluid.2012.06.021`.

[20] P. Goatin and P. G. LeFloch. The Riemann problem for a class of resonant hyperbolic systems of balance laws. *Annales de l'Institut Henri Poincare (C) Non Linear Analysis*, 21(6):881—-902, 2004. doi: 10.1016/j.anihpc.2004.02.002. URL `https://doi.org/10.1016/j.anihpc.2004.02.002`.

[21] D. Kröner and M. D. Thanh. Numerical Solutions to Compressible Flows in a Nozzle with Variable Cross-section. *SIAM J. Numer. Anal*, 43(2):796—-824, 2005. doi: 10.1137/040607460. URL `https://doi.org/10.1137/040607460`.

[22] Philippe Helluy, Jean-Marc Hérard, and Hélène Mathisa. A well-balanced approximate Riemann solver for compressible flows in variable cross-section ducts. *J. Comput. and Appl. Mathem.*, 236(7):1976–1992, 2012. doi: 10.1016/j.cam.2011.11.008. URL `https://doi.org/10.1016/j.cam.2011.11.008`.

[23] D. H. Cuong and M. D. Thanh. Constructing a Godunov-type scheme for the model of a general fluid flow in a nozzle with variable cross-section. *Appl. Mathem. and Comput.*, 305(15):136–160, 2017. doi: 10.1016/j.amc.2017.01.065. URL `https://doi.org/10.1016/j.amc.2017.01.065`.

[24] S. Clain and D. Rochette. First- and second-order finite volume methods for the one-dimensional nonconservative Euler system. *J. Comput. Phys.*, 228(22):8214–8248, 2009. doi: 10.1016/j.jcp.2009.07.038. URL `https://doi.org/10.1016/j.jcp.2009.07.038`.

[25] S. A. Tokareva and E. F. Toro. HLLC-type Riemann solver for the Baer–Nunziato equations of compressible two-phase flow. *J. Comp. Phys.*, 229:3573–3604, 05 2010. doi: 10.1016/j.jcp.2010.01.016. URL `https://doi.org/10.1016/j.jcp.2010.01.016`.

[26] J. Murillo and P. García-Navarro. Augmented versions of the HLL and HLLC Riemann solvers including source terms in one and two dimensions for shallow flow applications. *J. Comput. Phys.*, 231(20):6861–6906, 2012. doi: 10.1016/j.jcp.2012.06.031. URL `https://doi.org/10.1016/j.jcp.2012.06.031`.

[27] T. Gallouët, J. Hérard, and N. Seguin. Some approximate Godunov schemes to compute shallow-water equations with topography. *Comp. & Fluids*, 32(4):479—-513, 2003. doi: 10.1016/S0045-7930(02)00011-7. URL `https://doi.org/10.1016/S0045-7930(02)00011-7`.

[28] Q. Liang and F. Marche. Numerical resolution of well-balanced shallow water equations with complex source terms. *Advances in Water Resources*, 32(6):873—-884, 2009. doi: 10.1016/j.advwatres.2009.02.010. URL `https://doi.org/10.1016/j.advwatres.2009.02.010`.

[29] E. Audusse, F. Bouchut, M. Bristeau, R. Klein, and B. Perthame. A Fast and Stable Well-Balanced Scheme with Hydrostatic Reconstruction for Shallow Water Flows. *SIAM J. Sci. Comput.*, 25(6):2050—-2065, 2006. doi: 10.1137/S1064827503431090. URL `https://doi.org/10.1137/S1064827503431090`.

[30] F. Bouchut. *Nonlinear Stability of Finite Volume Methods for Hyperbolic Conservation Laws and Well-Balanced Schemes for Sources.* Birkhäuser, 2004. doi: 10.1007/b93802.

[31] S. Brown, S. Martynov, and H. Mahgerefteh. Simulation of two-phase flow through ducts with discontinuous cross-section. *Comp. & Fluids*, 120(5):46–56, 2015. doi: 10.1016/j.compfluid.2015.07.018. URL `https://doi.org/10.1016/j.compfluid.2015.07.018`.

[32] S. LeMartelot, B. Nkong, and R. Saurel. Liquid and liquid–gas flows at all speeds. *J. Comput. Phys.*, 255:53–82, 2013. doi: 10.1016/j.jcp.2013.08.001. URL `https://doi.org/10.1016/j.jcp.2013.08.001`.

[33] M. R. Baer and J. W. Nunziato. A two-phase mixture theory for the deflagration-to-detonation transition (ddt) in reactive granular materials. *Int. J. Multiphase Flow*, 12:861–889, 1986. doi: 10.1016/0301-9322(86)90033-9. URL `https://doi.org/10.1016/0301-9322(86)90033-9`.

[34] R. J. Leveque. *Finite Volume Methods for Hyperbolic Problems.* Cambridge University Press, 32 Avenue of the Americas, New York, NY 10013-2473, USA, 2007. doi: 10.1017/CBO9780511791253.005.

[35] E. F. Toro. *Riemann Solvers and Numerical Methods for Fluid Mechanics - A Practical Introduction, 2nd edition.* Springer, Springer Dordrecht Heidelberg London New York, 1999. doi: 10.1007/978-3-540-49834-6.

[36] N. Andrianov. CONSTRUCT, a collection of MATLAB routines for constructing the exact solution to the Riemann problem for the Baer-Nunziato model of two-phase flows, 2004. URL `https://github.com/nikolai-andrianov/CONSTRUCT`.

[37] N. Andrianov and G. Warnecke. The Riemann problem for the Baer–Nunziato two-phase flow model. *J. Comput. Phys.*, 195(2):434–464, 2004. doi: 10.1016/j.jcp.2003.10.006. URL `https://doi.org/10.1016/j.jcp.2003.10.006`.

[38] A. H. S. Hansen. Modeling and simulation of respiratory flow. Master's thesis, NTNU, 2019.

[39] D. Y. Peng and D. B. Robinson. A New Two-Constant Equation of State. *Ind. Eng. Chem. Fundam.*, 15:59–64, 02 1976. doi: 10.1021/i160057a011. URL `https://doi.org/10.1021/i160057a011`.

[40] A. Harten. High resolution schemes for hyperbolic conservation laws. *J. Comput. Phys.*, 49(3):357–393, 1983. doi: 10.1016/0021-9991(83)90136-5. URL `https://doi.org/10.1016/0021-9991(83)90136-5`.

[41] M. Liou, C. Chang, L. Nguyen, and T. G. Theofanous. How to Solve Compressible Multifluid Equations: A Simple, Robust, and Accurate Method. *AIAA JOURNAL*, 46(9):2345—-2356, 2008. doi: 10.2514/1.34793. URL `https://doi.org/10.2514/1.34793`.

[42] S. F. Davis. Simplified Second-Order Godunov-Type Methods. *SIAM J. Sci. Stat. Comput.*, 9(3):445–437, 1988. doi: 10.1137/0909030. URL `https://doi.org/10.1137/0909030`.

[43] B. Einfeldt. On Godunov-type methods for gas dynamics. *SIAM J. Numer. Anal.*, 25(2):294—-318, 1988. doi: 10.1137/0725021. URL `https://doi.org/10.1137/0725021`.

[44] P. L. Roe. Approximate Riemann Solvers, Parameter Vectors, and Difference Schemes. *J. Comput. Phys.*, 43(2):357–372, 1981. doi: 10.1016/0021-9991(81)90128-5. URL `https://doi.org/10.1016/0021-9991(81)90128-5`.

[45] M. Prebeg, T. Flåtten, and B. Müller. Large time step HLL and HLLC schemes. *ESAIM: M2AN*, 52(4):1239–1260, 2018. doi: 10.1051/m2an/2017051. URL `https://doi.org/10.1051/m2an/2017051`.

[46] D. Rochette, S. Clain, and W. Bussière. Unsteady compressible flow in ducts with varying cross-section: Comparison between the nonconservative euler system and the axisymmetric flow model. *Comput. & Fluids*, 53:53 – 78, 2012. doi: 10.1016/j.compfluid.2011.09.004. URL `https://doi.org/10.1016/j.compfluid.2012.06.021`.

[47] C. M. Xisto, J. C. Páscoa, P. J. Oliveira, and D. A. Nicolini. A hybrid pressure–density-based algorithm for the Euler equations at all Mach number regimes. *Int. J. Numer. Methods Fluids*, 70(8):961–976, 11 2011. doi: 10.1002/fld.2722. URL `https://doi.org/10.1002/fld.2722`.

[48] I. Demirdžić, Ž. Lilek, and M. Perić. A collocated finite volume method for predicting flows at all speeds. *Int. J. Numer. Methods Fluids*, 16(12):1029–1050, 1993. doi: 10.1002/fld.1650161202. URL `https://doi.org/10.1002/fld.1650161202`.

[49] F. Moukalled and M. Darwish. A high-resolution pressure-based algorithm for fluid flow at all speeds. *J. Comp. Phys.*, 168(1):101–130, 2001. doi: 10.1006/jcph.2000.6683. URL `https://doi.org/10.1006/jcph.2000.6683`.

[50] R. Berry, L. Zou, H. Zhao, D. Andrs, J. Peterson, and H. Zhang. RELAP-7: Demonstrating Seven-Equation, Two-Phase Flow Simulation in a Single- Pipe, Two-Phase Reactor Core and Steam Separator/Dryer. Technical report, Idaho National Laboratory, 2013. URL `https://doi.org/10.2172/1107263`.

[51] S. Zanzi. *Numerical Simulation of Condensing CO_2 Supersonic Flows at High Pressure*. PhD thesis, Politecnico di Milano, 2019.

[52] C. Lettieri, D. Paxson, Z. Spakovszky, and P. Bryanston-Cross. Characterization of Nonequilibrium Condensation of Supercritical Carbon Dioxide in a de Laval Nozzle. *J. Eng. Gas Turbines Power*, 140, 04 2018. doi: 10.1115/1.4038082. URL `https://doi.org/10.1115/1.4038082`.

[53] C. H. Lim. Visualization of Nucleation of Supercritical Carbon Dioxide Flow Through a Nozzle. Master's thesis, Georgia Institute of Technology, 2019.

[54] DEPRESS - Depressurization facility. URL `https://www.eccsel.org/facilities/transport/no25_sintef_er_depress/`. Trondheim, Norway.

[55] R. Span and W. Wagner. A New Equation of State for Carbon Dioxide Covering the Fluid Region from the Triple-Point Temperature to 1100 K at Pressures up to 800 MPa. *J. Phys. Chem. Ref. Data*, 25(6):1509—-1596, 1996. doi: 10.1063/1.555991. URL `https://doi.org/10.1063/1.555991`.

A. Full derivation of the general Jacobian matrix for the Euler equations

We have the following;

$$\boldsymbol{U} = \begin{pmatrix} U_1 \\ U_2 \\ U_3 \end{pmatrix} = \begin{pmatrix} \rho \\ \rho u \\ E \end{pmatrix}, \ \boldsymbol{F(U)} = \begin{pmatrix} F_1 \\ F_2 \\ F_3 \end{pmatrix} = \begin{pmatrix} \rho u \\ \rho u^2 + p \\ (E+p)u. \end{pmatrix}$$

and wish to find

$$\boldsymbol{A(U)} = \begin{pmatrix} \frac{\partial F_1}{\partial U_1} & \frac{\partial F_1}{\partial U_2} & \frac{\partial F_1}{\partial U_3} \\ \frac{\partial F_2}{\partial U_1} & \frac{\partial F_2}{\partial U_2} & \frac{\partial F_2}{\partial U_3} \\ \frac{\partial F_3}{\partial U_1} & \frac{\partial F_3}{\partial U_2} & \frac{\partial F_3}{\partial U_3} \end{pmatrix}.$$

In order to find $\boldsymbol{A}$, we must first find differential relations between the different variables u, e, and p and $dU_i,\ i = 1,\, 2,\, 3$. First we find an expression for du;

$$\begin{aligned} dU_2 &= d(\rho u) = u d\rho + \rho du = u dU_1 + \rho du \\ \Rightarrow du &= -\frac{u}{\rho} dU_1 + \frac{1}{\rho} dU_2. \end{aligned}$$

Then we can find de by dU_3;

$$\begin{aligned} dU_3 &= d\left(\rho(e + \frac{1}{2}u^2)\right) \\ &= d\left(\rho e\right) + d\left(\frac{1}{2}\rho u^2\right) \\ &= e dU_1 + \rho de + \frac{1}{2}\rho du^2 + \frac{1}{2}u^2 dU_1 \\ &= e dU_1 + \rho de + u\rho du + \frac{1}{2}u^2 dU_1. \end{aligned}$$

Here we can insert the relation found above for du;

$$dU_3 = e dU_1 + \rho de + u\rho\left(-\frac{u}{\rho} dU_1 + \frac{1}{\rho} dU_2\right) + \frac{1}{2}u^2 dU_1,$$

and rearrange to give

$$\begin{aligned} dU_3 &= \left(e - \frac{1}{2}u^2\right) dU_1 + \rho de + u dU_2 \\ \Rightarrow de &= -\frac{1}{\rho}\left(e - \frac{1}{2}u^2\right) dU_1 - \frac{u}{\rho} dU_2 + \frac{1}{\rho} dU_3. \end{aligned}$$

Since we want to prove this generally, we cannot assume an equation of state relation between e, ρ and p. However, the following general relation holds:

$$dp = \left(c^2 - \frac{p}{\rho}\Gamma\right) d\rho + \Gamma \rho de.$$

Using the relations found above we can now express $d\boldsymbol{F}$ in terms of $d\boldsymbol{U}$.

$$dF_1 = dU_2,$$

$$\begin{aligned}
dF_2 &= d\left(\rho u^2 + p\right) \\
&= udU_2 + \rho udu + dp \\
&= udU_2 + \rho u\left(-\frac{u}{\rho}dU_1 + \frac{1}{\rho}dU_2\right) + \left(c^2 - \frac{p}{\rho}\Gamma\right) dU_1 \\
&\quad + \Gamma\rho\left(-\frac{1}{\rho}\left(e - \frac{1}{2}u^2\right) dU_1 - \frac{u}{\rho}dU_2 + \frac{1}{\rho}dU_3\right) \\
&= \left(c^2 - u^2 - \Gamma\left(e + \frac{p}{\rho} - \frac{1}{2}u^2\right)\right) dU_1 + \left(2u - \Gamma u\right) dU_2 + \Gamma dU_3
\end{aligned}$$

and, finally

$$\begin{aligned}
dF_3 &= d\left(\left(\rho(e + \frac{1}{2}u^2) + p\right) u\right) \\
&= ud\left(\rho(e + \frac{1}{2}u^2) + p\right) + \left(\rho(e + \frac{1}{2}u^2) + p\right) du \\
&= udU_3 + udp + \left(\rho(e + \frac{1}{2}u^2) + p\right) du \\
&= udU_3 + u\left((c^2 - \frac{p}{\rho}\Gamma)dU_1 + \Gamma\rho de\right) + \left(\rho(e + \frac{1}{2}u^2) + p\right)\left(-\frac{u}{\rho}dU_1 + \frac{1}{\rho}dU_2\right) \\
&= udU_3 + u\left(c^2 - \frac{p}{\rho}\Gamma\right) dU_1 + u\Gamma\rho\left(-\frac{1}{\rho}(e - \frac{1}{2}u^2)dU_1 - \frac{u}{\rho}dU_2 + \frac{1}{\rho}dU_3\right) \\
&\quad + \left(\rho(e + \frac{1}{2}u^2) + p\right)\left(-\frac{u}{\rho}dU_1 + \frac{1}{\rho}dU_2\right) \\
&= u\left(c^2 - \Gamma(e - \frac{1}{2}u^2 + \frac{p}{\rho}) - e - \frac{1}{2}u^2 - \frac{p}{\rho}\right) dU_1 + \left((e + \frac{1}{2}u^2 + \frac{p}{\rho}) - u^2\Gamma\right) dU_2 \\
&\quad + \left(\Gamma + 1\right) udU_3 \\
&= u\left(c^2 + \Gamma u^2 - \left(\Gamma + 1\right)(e + \frac{1}{2}u^2 + \frac{p}{\rho})\right) dU_1 + (e + \frac{1}{2}u^2 + \frac{p}{\rho} - \Gamma u^2)dU_2 \\
&\quad + (\Gamma + 1)udU_3.
\end{aligned}$$

This finally gives us the general Jacobian matrix for the Euler equations:

$$\boldsymbol{A} = \begin{pmatrix} 0 & 1 & 0 \\ c^2 - u^2 - \Gamma(e + \frac{p}{\rho} - \frac{1}{2}u^2) & (2-\Gamma)u & \Gamma \\ u\left(c^2 - (\Gamma+1)(e + \frac{1}{2}u^2 + \frac{p}{\rho}) + \Gamma u^2\right) & e + \frac{p}{\rho} + \frac{1}{2}u^2 - \Gamma u^2 & (\Gamma+1)u \end{pmatrix}$$

B. Proof of the form of the characteristic variables for the Euler equations

As explained in Section 2.2.1, the characteristic variables are defined by $\partial \boldsymbol{W} = \boldsymbol{R}^{-1}\partial \boldsymbol{U}$, where $\boldsymbol{R}^{-1}$ is the inverse of the right eigenvector matrix of the Jacobian matrix $\boldsymbol{A}$ of the Euler equations. The right eigenvectors are given in Equation (2.14), producing the following right eigenvector matrix;

$$\boldsymbol{R} = [\boldsymbol{r}_1, \boldsymbol{r}_2, \boldsymbol{r}_3] = \begin{pmatrix} 1 & 1 & 1 \\ u - c & u & u + c \\ H - uc & H - \frac{c^2}{\Gamma} & H + uc \end{pmatrix}, \tag{B.1}$$

where $H = \frac{E+p}{\rho} = e + \frac{p}{\rho} + \frac{1}{2}u^2$. The inverse of this matrix can be found using a symbolic computation program such as Maple for example, or as I have used; the symbolic python library *SymPy*. This gives

$$\boldsymbol{R}^{-1} = \begin{pmatrix} \dfrac{1}{2} + \dfrac{u}{2c} - \dfrac{\Gamma}{2c^2}(H - u^2) & -\dfrac{1}{2c^2}(c + \Gamma u) & \dfrac{\Gamma}{2c^2} \\ \dfrac{\Gamma}{c^2}(H - u^2) & \dfrac{\Gamma u}{c^2} & -\dfrac{\Gamma}{c^2} \\ -\dfrac{1}{2} + \dfrac{u}{2c} + \dfrac{\Gamma u}{c} - \dfrac{\Gamma}{2c^2}(H + u^2) & \dfrac{1}{2c^2}(c - \Gamma u) & \dfrac{\Gamma}{2c^2} \end{pmatrix}. \tag{B.2}$$

We then get

$$\partial \boldsymbol{W} = \boldsymbol{R}^{-1}\partial \boldsymbol{U} \tag{B.3}$$

$$= \begin{pmatrix} \dfrac{1}{2} + \dfrac{u}{2c} - \dfrac{\Gamma}{2c^2}(H - u^2) & -\dfrac{1}{2c^2}(c + \Gamma u) & \dfrac{\Gamma}{2c^2} \\ \dfrac{\Gamma}{c^2}(H - u^2) & \dfrac{\Gamma u}{c^2} & -\dfrac{\Gamma}{c^2} \\ -\dfrac{1}{2} + \dfrac{u}{2c} + \dfrac{\Gamma u}{c} - \dfrac{\Gamma}{2c^2}(H + u^2) & \dfrac{1}{2c^2}(c - \Gamma u) & \dfrac{\Gamma}{2c^2} \end{pmatrix} \begin{pmatrix} \partial \rho \\ \partial(\rho u) \\ \partial E \end{pmatrix}. \tag{B.4}$$

Here,

$$\partial(\rho u) = \rho \partial u + u \partial \rho$$

and

$$\partial E = \partial\left(\rho(e + \frac{1}{2}u^2)\right) = \rho \partial e + e \partial \rho + \rho u \partial u + \frac{1}{2}u^2 \partial \rho.$$

In addition, as we assume that $p = p(\rho, e)$, the following relation can be used

$$\partial p = (c^2 - \frac{p}{\rho}\Gamma)\partial\rho + \Gamma\partial e,$$

as usual. This relation can be solved for ∂e, giving

$$\partial e = \frac{1}{\Gamma\rho}\partial p - \frac{1}{\Gamma\rho}(c^2 - \Gamma\frac{p}{\rho})\partial\rho.$$

Inserting the relations for $\partial(\rho u)$, ∂E and ∂e in Equation (B.4), we finally get

$$\partial \boldsymbol{W} = \begin{pmatrix} -\frac{\rho}{2c}\partial u + \frac{1}{2c^2}\partial p \\ \partial\rho - \frac{1}{c^2}\partial p \\ \frac{\rho}{2c}\partial u + \frac{1}{2c^2}\partial p \end{pmatrix}. \tag{B.5}$$

C. Proof of entropy being constant along lines of smooth flow

The Euler equations can be manipulated to show that the entropy in the system will stay constant along lines of smooth flow. This can be shown by first using the momentum conservation law (2.8) and the mass conservation law (2.7) to express how the kinetic energy changes over time.

$$\begin{aligned}
\frac{\partial(\rho u)}{\partial t} + \frac{\partial(u\rho u)}{\partial x} + \frac{\partial p}{\partial x} &= 0 \\
u\frac{\partial(\rho u)}{\partial t} + u\frac{\partial(u\rho u)}{\partial x} + u\frac{\partial p}{\partial x} &= 0 \\
u^2\frac{\partial \rho}{\partial t} + u\rho\frac{\partial u}{\partial t} + u^2\frac{\partial(\rho u)}{\partial x} + u\rho u\frac{\partial u}{\partial x} + u\frac{\partial p}{\partial x} &= 0 \\
\frac{1}{2}u^2\frac{\partial \rho}{\partial t} + u\rho\frac{\partial u}{\partial t} + \frac{1}{2}u^2\frac{\partial(\rho u)}{\partial x} + u\rho u\frac{\partial u}{\partial x} + u\frac{\partial p}{\partial x} &= -\frac{1}{2}u^2\cancelto{0}{\left(\frac{\partial \rho}{\partial t} + \frac{\partial(\rho u)}{\partial x}\right)} \\
\Rightarrow \frac{\partial(\frac{1}{2}\rho u^2)}{\partial t} + \frac{\partial(u\frac{1}{2}\rho u^2)}{\partial x} + u\frac{\partial p}{\partial x} &= 0
\end{aligned}$$

The kinetic energy evolution can then be subtracted from the energy conservation law (2.9).

$$\begin{aligned}
\frac{\partial E}{\partial t} + \frac{\partial(uE)}{\partial} + \frac{\partial(uP)}{\partial} &= 0 \\
\frac{\partial(\rho e)}{\partial t} + \frac{\partial(\frac{1}{2}\rho u^2)}{\partial t} + \frac{\partial(u\rho e)}{\partial x} + \frac{\partial(u\frac{1}{2}\rho u^2)}{\partial x} + \frac{\partial(up)}{\partial x} &= 0 \\
\frac{\partial(\rho e)}{\partial t} + \frac{\partial(u\rho e)}{\partial x} + \frac{\partial(up)}{\partial x} - u\frac{\partial p}{\partial x} &= 0 \\
\frac{\partial(\rho e)}{\partial t} + \frac{\partial(u\rho e)}{\partial x} + p\frac{\partial u}{\partial x} &= 0
\end{aligned}$$

This can be expanded, rearranged, and the conservation of mass can be used to cancel terms;

$$e\cancelto{0}{\left(\frac{\partial \rho}{\partial t} + \frac{\partial(\rho u)}{\partial x}\right)} + \rho\frac{\partial e}{\partial t} + \rho u\frac{\partial e}{\partial x} + p\frac{\partial u}{\partial x} = 0$$

Using the first law of thermodynamics

$$de = Tds + \frac{p}{\rho^2}d\rho,$$

this can be written in terms of entropy giving:

$$\rho T\frac{\partial s}{\partial t}+\frac{p}{\rho}\frac{\partial \rho}{\partial t}+\rho uT\frac{\partial s}{\partial x}+u\frac{p}{\rho}\frac{\partial \rho}{\partial x}+p\frac{\partial u}{\partial x}=0$$

$$\rho T\frac{\partial s}{\partial t}+\rho uT\frac{\partial s}{\partial x}+\frac{p}{\rho}\cancelto{0}{\left(\frac{\partial \rho}{\partial t}+u\frac{\partial \rho}{\partial x}+\rho\frac{\partial u}{\partial x}\right)}=0.$$

This finally yields:

$$\frac{\partial s}{\partial t}+u\frac{\partial s}{\partial x}=0,$$

which means that the entropy is constant along smooth lines of flow.

D. Full derivation of the general Jacobian matrix for the Euler equations with area change

We have the following;

$$\boldsymbol{U} = \begin{pmatrix} U_1 \\ U_2 \\ U_3 \\ U_4 \end{pmatrix} = \begin{pmatrix} \rho A \\ \rho u A \\ EA \\ A \end{pmatrix}, \ \boldsymbol{F}(\boldsymbol{U}) = \begin{pmatrix} F_1 \\ F_2 \\ F_3 \\ F_4 \end{pmatrix} = \begin{pmatrix} \rho u A \\ (\rho u^2 + p)A \\ (E+p)uA \\ 0 \end{pmatrix}, \boldsymbol{S} = \begin{pmatrix} S_1 \\ S_2 \\ S_3 \\ S_4 \end{pmatrix} = \begin{pmatrix} 0 \\ p\frac{\partial A}{\partial x} \\ 0 \\ 0 \end{pmatrix}.$$

where $E = \rho(e + \frac{1}{2}u^2)$ and we wish to find $\boldsymbol{A}(\boldsymbol{U})$ such that the system

$$(\rho A)_t + (\rho u A)_x = 0 \tag{D.1}$$

$$(\rho u A)_t + \big((\rho u^2 + p)A\big)_x - pA_x = 0 \tag{D.2}$$

$$(EA)_t + ((E+p)uA)_x = 0 \tag{D.3}$$

$$A_t = 0 \tag{D.4}$$

can be written on the form

$$\boldsymbol{U}_t + \boldsymbol{A}(\boldsymbol{U})\boldsymbol{U}_x = \boldsymbol{0}. \tag{D.5}$$

We know a priori that the Jacobi matrix will be on the form

$$\boldsymbol{A}(\boldsymbol{U}) = \begin{pmatrix} \dfrac{\partial F_1}{\partial U_1} & \dfrac{\partial F_1}{\partial U_2} & \dfrac{\partial F_1}{\partial U_3} & \dfrac{\partial F_1}{\partial U_4} \\ \dfrac{\partial F_2}{\partial U_1} & \dfrac{\partial F_2}{\partial U_2} & \dfrac{\partial F_2}{\partial U_3} & \dfrac{\partial F_2}{\partial U_4} - p \\ \dfrac{\partial F_3}{\partial U_1} & \dfrac{\partial F_3}{\partial U_2} & \dfrac{\partial F_3}{\partial U_3} & \dfrac{\partial F_3}{\partial U_4} \\ \dfrac{\partial F_4}{\partial U_1} & \dfrac{\partial F_4}{\partial U_2} & \dfrac{\partial F_4}{\partial U_3} & \dfrac{\partial F_4}{\partial U_4} \end{pmatrix}, \tag{D.6}$$

where the p being subtracted from $\dfrac{\partial F_2}{\partial U_4}$ comes from the source term $p\dfrac{\partial A}{\partial x} = p\dfrac{\partial U_4}{\partial x}$.

In order to find $\boldsymbol{A}$, we must first find differential relations between the different variables u, e, and p and $dU_i,\ i = 1,\ 2,\ 3,\ 4$. First we find an expression for du;

$$\begin{aligned} dU_2 &= d(\rho u A) = u d(\rho A) + \rho A du = u dU_1 + \rho A du \\ \Rightarrow du &= -\frac{u}{\rho A} dU_1 + \frac{1}{\rho A} dU_2. \end{aligned} \tag{D.7}$$

Then we can find de by dU_3;

$$\begin{aligned} dU_3 &= d\left(\rho(e + \frac{1}{2}u^2)A\right) \\ &= d\left(\rho A e\right) + d\left(\frac{1}{2}\rho A u^2\right) \\ &= e dU_1 + \rho A de + \frac{1}{2}\rho A du^2 + \frac{1}{2}u^2 dU_1 \\ &= e dU_1 + \rho A de + u\rho A du + \frac{1}{2}u^2 dU_1. \end{aligned}$$

Here we can insert the relation found above for du;

$$dU_3 = e dU_1 + \rho A de + u\rho A\left(-\frac{u}{\rho A} dU_1 + \frac{1}{\rho A} dU_2\right) + \frac{1}{2}u^2 dU_1,$$

and rearrange to give

$$\begin{aligned} dU_3 &= \left(e - \frac{1}{2}u^2\right) dU_1 + \rho A de + u dU_2 \\ \Rightarrow de &= -\frac{1}{\rho A}\left(e - \frac{1}{2}u^2\right) dU_1 - \frac{u}{\rho A} dU_2 + \frac{1}{\rho A} dU_3. \end{aligned} \tag{D.8}$$

We assume a general equation of state $p = p(\rho, e)$. Then the following general relation holds:

$$dp = \left(c^2 - \frac{p}{\rho}\Gamma\right) d\rho + \Gamma\rho de. \tag{D.9}$$

This can be rewritten in terms of dU_i, $i = 1, 2, 3, 4$.

$$\begin{aligned} dp &= \left(c^2 - \frac{p}{\rho}\Gamma\right) d\left(\frac{\rho A}{A}\right) + \Gamma\rho de \\ &= \left(c^2 - \frac{p}{\rho}\Gamma\right)\left(-(\rho A)\frac{1}{A^2} dA + \frac{1}{A} d(\rho A)\right) + \Gamma\rho de \\ &= \left(c^2 - \frac{p}{\rho}\Gamma\right)\left(-(\rho A)\frac{1}{A^2} dU_4 + \frac{1}{A} dU_1\right) + \Gamma\rho\left(-\frac{1}{\rho A}\left(e - \frac{1}{2}u^2\right) dU_1 - \frac{u}{\rho A} dU_2 + \frac{1}{\rho A} dU_3\right) \end{aligned} \tag{D.10}$$

Using the relations found above we can now express dF_1, dF_2 and dF_3 in terms of $d\boldsymbol{U}$.

$$dF_1 = dU_2,$$

$$\begin{aligned}
dF_2 &= d\left(\left(\rho u^2 + p\right) A\right) \\
&= udU_2 + \rho u A du + A dp + p dA \\
&= udU_2 + \rho u A \left(-\frac{u}{\rho A} dU_1 + \frac{1}{\rho A} dU_2\right) + A\left(c^2 - \frac{p}{\rho}\Gamma\right)\left(-(\rho A)\frac{1}{A^2} dU_4 + \frac{1}{A} dU_1\right) \\
&\quad + A\Gamma\rho\left(-\frac{1}{\rho A}\left(e - \frac{1}{2}u^2\right) dU_1 - \frac{u}{\rho A} dU_2 + \frac{1}{\rho A} dU_3\right) + p dU_4 \\
&= \left(c^2 - u^2 - \Gamma\left(e + \frac{p}{\rho} - \frac{1}{2}u^2\right)\right) dU_1 + (2 - \Gamma)\, u dU_2 + \Gamma dU_3 + \left(p(\Gamma + 1) - \rho c^2\right) dU_4,
\end{aligned}$$

and

$$\begin{aligned}
dF_3 &= d\left(\left(\rho(e + \frac{1}{2}u^2) + p\right) uA\right) \\
&= ud\left(\rho(e + \frac{1}{2}u^2)A + pA\right) + \left(\rho(e + \frac{1}{2}u^2)A + pA\right) du \\
&= udU_3 + ud(pA) + \left(\rho(e + \frac{1}{2}u^2)A + pA\right) du \\
&= udU_3 + u[Adp + pdA] + \left(\rho(e + \frac{1}{2}u^2)A + pA\right) du \\
&= udU_3 + u\Bigg[A\left(c^2 - \frac{p}{\rho}\Gamma\right)\left(-(\rho A)\frac{1}{A^2} dU_4 + \frac{1}{A} dU_1\right) \\
&\qquad\qquad + A\Gamma\rho\left(-\frac{1}{\rho A}\left(e - \frac{1}{2}u^2\right) dU_1 - \frac{u}{\rho A} dU_2 + \frac{1}{\rho A} dU_3\right) + p dU_4\Bigg] \\
&\quad + \left(\rho(e + \frac{1}{2}u^2)A + pA\right)\left(-\frac{u}{\rho A} dU_1 + \frac{1}{\rho A} dU_2\right) \\
&= u\left(c^2 - \frac{p}{\rho}\Gamma\right) dU_1 - u\left(\Gamma\left(e - \frac{1}{2}u^2\right)\right) dU_1 - u\left(e + \frac{1}{2}u^2 + \frac{p}{\rho}\right) dU_1 \\
&\quad - u^2\Gamma dU_2 + \left(e + \frac{1}{2}u^2 + \frac{p}{\rho}\right) dU_2 \\
&\quad + udU_3 + u\Gamma dU_3 \\
&\quad + u\left(p\Gamma - \rho c^2\right) dU_4 + upd U_4 \\
&= u\left(c^2 - (\Gamma + 1)\,(e + \frac{1}{2}u^2 + \frac{p}{\rho}) + \Gamma u^2\right) dU_1 + \left(e + \frac{1}{2}u^2 + \frac{p}{\rho} - \Gamma u^2\right) dU_2 \\
&\quad + u(\Gamma + 1) dU_3 + u\left(p(\Gamma + 1) - \rho c^2\right) dU_4.
\end{aligned}$$

This finally gives us the general Jacobian matrix for the Euler equations with area change:

$$\boldsymbol{A} = \begin{pmatrix} 0 & 1 & 0 & 0 \\ c^2 - u^2 - \Gamma(e + \dfrac{p}{\rho} - \dfrac{1}{2}u^2) & (2-\Gamma)u & \Gamma & \Gamma p - \rho c^2 \\ u\left(c^2 - (\Gamma+1)(e + \dfrac{1}{2}u^2 + \dfrac{p}{\rho}) + \Gamma u^2\right) & e + \dfrac{p}{\rho} + \dfrac{1}{2}u^2 - \Gamma u^2 & (\Gamma+1)u & u\left(p(\Gamma+1) - \rho c^2\right) \\ 0 & 0 & 0 & 0 \end{pmatrix}.$$

E. Full derivation of the Jacobian matrix of the nonlinear system in HLLCS for positive subsonic flow

E.1. Introduction

We have the following set of equations

$$\boldsymbol{f} = \begin{pmatrix} A_L \rho_L^-(p_L^-) u_L^-(p_L^-) - A_R \rho_R^+ \left(p_R^+, s(p_L^-)\right) u_R^+(p_R^+) \\ h_R^+ \left(p_R^+, s(p_L^-)\right) + \frac{1}{2}\left(u_R^+(p_R^+)\right)^2 - \left[h_L^- \left(p_L^-, s(p_L^-)\right) + \frac{1}{2}\left(u_L^-(p_L^-)\right)^2\right] \end{pmatrix}, \tag{E.1}$$

with the Jacobian matrix

$$d\boldsymbol{f} = \begin{pmatrix} \dfrac{\partial \boldsymbol{f}_1}{\partial p_L^-} & \dfrac{\partial \boldsymbol{f}_1}{\partial p_R^{++}} \\ \dfrac{\partial \boldsymbol{f}_2}{\partial p_L^-} & \dfrac{\partial \boldsymbol{f}_2}{\partial p_R^{++}} \end{pmatrix}. \tag{E.2}$$

We have that

$$\rho_L^-(p_L^-) = \rho_L \frac{S_L - u_L}{S_L - u_L^-(p_L^-)}, \tag{E.3}$$

$$u_L^-(p_L^-) = u_L + \frac{p_L^- - p_L}{\rho_L (S_L - u_L)}, \tag{E.4}$$

$$E_L^-(p_L^-) = \rho_L^-(p_L^-) \left(\frac{E_L}{\rho_L} + (u_L^-(p_L^-) - u_L)\left(u_L^-(p_L^-) + \frac{p_L}{\rho_L(S_L - u_L)}\right)\right), \tag{E.5}$$

and

$$\rho_R^{++}(p_R^{++}) = \rho_R \frac{S_R - u_R}{S_R - u_R^{++}(p_R^{++})}, \tag{E.6}$$

$$u_R^+(p_R^{++}) = u_R^{++} = u_R + \frac{p_R^{++} - p_R}{\rho_R (S_R - u_R)}. \tag{E.7}$$

$$E_R^{++}(p_R^{++}) = \rho_R^{++}(p_R^{++}) \left(\frac{E_R}{\rho_R} + (u_R^{++}(p_R^{++}) - u_R)\left(u_R^{++}(p_R^{++}) + \frac{p_R}{\rho_R(S_R - u_R)}\right)\right). \tag{E.8}$$

This gives the following general derivatives with respect to p_L^-:

$$\frac{\partial u_L^-}{\partial p_L^-} = \frac{1}{\rho_L (S_L - u_L)}, \tag{E.9}$$

$$\frac{\partial \rho_L^-}{\partial p_L^-} = \rho_L \frac{S_L - u_L}{(S_L - u_L^-)^2} \frac{\partial u_L^-}{\partial p_L^-} = \frac{1}{(S_L - u_L^-)^2}, \tag{E.10}$$

and the following derivative with respect to p_R^+

$$\frac{\partial u_R^+}{\partial p_R^+} = \frac{1}{\rho_R (S_R - u_R)}. \tag{E.11}$$

All other derivatives in the Jacobi matrix will come from an equation of state.

E.2. Derivation

The full Jacobian matrix is derived below. We start by the first term, $\dfrac{\partial \boldsymbol{f}_1}{\partial p_L^-}$.

$$\begin{aligned}
\frac{\partial \boldsymbol{f}_1}{\partial p_L^-} &= \frac{\partial \left[A_L \rho_L^-(p_L^-) u_L^-(p_L^-) - A_R \rho_R^+ \left(s(p_L^-) \right) u_R^+ \right]}{\partial p_L^-} \\
&= A_L \frac{\partial \left[\rho_L^-(p_L^-) u_L^-(p_L^-) \right]}{\partial p_L^-} - A_R u_R^+ \frac{\partial \rho_R^+ \left(s(p_L^-) \right)}{\partial p_L^-} \\
&= A_L \left[u_L^- \frac{\partial \rho_L^-(p_L^-)}{\partial p_L^-} + \rho_L^- \frac{\partial u_L^-(p_L^-)}{\partial p_L^-} \right] - A_R u_R^+ \frac{\partial \rho_R^+(s)}{\partial s} \frac{\partial s(p_L^-)}{\partial p_L^-}
\end{aligned}$$

The derivatives involving the entropy depend on the equation of state. For the purpose of initial tests in this work, ideal gas EOS is used. In that case, enforcing that $s_L^- = s_R^+ = s$ gives

$$\rho_R^+ = \rho_L^-(p_L^-) \left[\frac{p_R^+}{p_L^-} \right]^{1/\gamma}. \tag{E.12}$$

We then get that

$$\frac{\partial \rho_R^+(p_L^-)}{\partial p_L^-} = \left[\frac{p_R^+}{p_L^-} \right]^{1/\gamma} \left(\frac{\partial \rho_L^-}{\partial p_L^-} - \frac{\rho_L^-}{\gamma p_L^-} \right). \tag{E.13}$$

For ideal gas,

$$\frac{\partial \boldsymbol{f}_1^{\text{ideal}}}{\partial p_L^-} = A_L \left[u_L^- \frac{\partial \rho_L^-(p_L^-)}{\partial p_L^-} + \rho_L^- \frac{\partial u_L^-(p_L^-)}{\partial p_L^-} \right] - A_R u_R^+ \left[\frac{p_R^+}{p_L^-} \right]^{1/\gamma} \left(\frac{\partial \rho_L^-(p_L^-)}{\partial p_L^-} - \frac{\rho_L^-}{\gamma p_L^-} \right). \tag{E.14}$$

The next term in the Jacobian, $\dfrac{\partial \boldsymbol{f}_1}{\partial p_R^+}$ is computed in a similar manner

$$\begin{aligned}
\frac{\partial \boldsymbol{f}_1}{\partial p_R^+} &= \frac{\partial \left[A_L \rho_L^- u_L^- - A_R \rho_R^+ \left(p_R^+ \right) u_R^+(p_R^+) \right]}{\partial p_R^+} \\
&= -A_R \frac{\partial \left[\rho_R^+ \left(p_R^+ \right) u_R^+(p_R^+) \right]}{\partial p_R^+} \\
&= -A_R \left[u_R^+ \frac{\partial \rho_R^+ \left(p_R^+ \right)}{\partial p_R^+} + \rho_R^+ \frac{\partial u_R^+ \left(p_R^+ \right)}{\partial p_R^+} \right].
\end{aligned}$$

The derivative of the density once again depends on the EOS. For ideal gas, the density derivative can be expressed as

$$\frac{\partial \rho_R^+}{\partial p_L^+} = \frac{\rho_L^-}{\gamma p_R^+}\left[\frac{p_R^+}{p_L^-}\right]^{1/\gamma}. \tag{E.15}$$

For ideal gas

$$\frac{\partial \boldsymbol{f}_1^{\text{ideal}}}{\partial p_R^+} = -A_R\left[\frac{\rho_L^- u_R^+}{\gamma p_R^+}\left[\frac{p_R^+}{p_L^-}\right]^{1/\gamma} + \rho_R^+\frac{\partial u_R^+\left(p_R^+\right)}{\partial p_R^+}\right]. \tag{E.16}$$

We now continue to the next derivative, $\dfrac{\partial \boldsymbol{f}_2}{\partial p_L^-}$:

$$\begin{aligned}
\frac{\partial \boldsymbol{f}_2}{\partial p_L^-} &= \frac{\partial\left[h_R^+\left(s(p_L^-)\right) + \frac{1}{2}\left(u_R^+\right)^2 - \left[h_L^-\left(p_L^-, s(p_L^-)\right) + \frac{1}{2}\left(u_L^-(p_L^-)\right)^2\right]\right]}{\partial p_L^-} \\
&= \frac{\partial h_R^+\left(s(p_L^-)\right)}{\partial p_L^-} - \frac{\partial h_L^-\left(p_L^-\right)}{\partial p_L^-} - \frac{\partial\left[\frac{1}{2}\left(u_L^-(p_L^-)\right)^2\right]}{\partial p_L^-} \\
&= \frac{\partial h_R^+}{\partial s}\frac{\partial s(p_L^-)}{\partial p_L^-} - \frac{\partial h_L^-\left(p_L^-\right)}{\partial p_L^-} - u_L^-\frac{\partial u_L^-(p_L^-)}{\partial p_L^-}.
\end{aligned}$$

If we assume ideal gas

$$h = \frac{\gamma}{\gamma-1}\frac{p}{\rho} \tag{E.17}$$

we get that

$$\frac{\partial h_L^-\left(p_L^-\right)}{\partial p_L^-} = \frac{\gamma}{\gamma-1}\frac{1}{\rho_L^-}\left[1 - \frac{p_L^-}{\rho_L^-}\frac{\partial \rho_L^-}{\partial p_L^-}\right], \tag{E.18}$$

and

$$\frac{\partial h_R^+}{\partial p_L^-} = -\frac{\gamma}{\gamma-1}p_R^+\frac{1}{(\rho_R^+)^2}\frac{\partial \rho_R^+}{\partial p_L^-}. \tag{E.19}$$

We then have, for ideal gas

$$\frac{\partial \boldsymbol{f}_2^{\text{ideal}}}{\partial p_L^-} = -\frac{\gamma}{\gamma-1}p_R^+\frac{1}{(\rho_R^+)^2}\frac{\partial \rho_R^+}{\partial p_L^-} - \frac{\gamma}{\gamma-1}\frac{1}{\rho_L^-}\left[1 - \frac{p_L^-}{\rho_L^-}\frac{\partial \rho_L^-}{\partial p_L^-}\right] - u_L^-\frac{\partial u_L^-(p_L^-)}{\partial p_L^-}. \tag{E.20}$$

Lastly, the final term in the Jacobian is

$$\begin{aligned}
\frac{\partial \boldsymbol{f}_2}{\partial p_R^+} &= \frac{\partial\left[h_R^+\left(p_R^+, s\right) + \frac{1}{2}\left(u_R^+(p_R^+)\right)^2 - \left[h_L^- + \frac{1}{2}\left(u_L^-\right)^2\right]\right]}{\partial p_R^+} \\
&= \frac{\partial h_R^+\left(p_R^+, s\right)}{\partial p_R^+} + u_R^+\frac{\partial u_R^+(p_R^+)}{\partial p_R^+}.
\end{aligned}$$

If we assume ideal gas EOS the enthalpy derivative becomes

$$\frac{\partial h_R^+\left(p_R^+, s\right)}{\partial p_R^+} = \frac{\gamma}{\gamma - 1}\frac{1}{\rho_R^+}\left(1 - \frac{p_R^+}{\rho_R^+}\frac{\partial \rho_R^+}{\partial p_R^+}\right), \tag{E.21}$$

such that

$$\frac{\partial \boldsymbol{f}_2^{\text{ideal}}}{\partial p_R^+} = \frac{\gamma}{\gamma - 1}\frac{1}{\rho_R^+}\left(1 - \frac{p_R^+}{\rho_R^+}\frac{\partial \rho_R^+}{\partial p_R^+}\right) + u_R^+\frac{\partial u_R^+(p_R^+)}{\partial p_R^+}. \tag{E.22}$$

E.3. Summary

The Jacobi matrix,

$$d\boldsymbol{f} = \begin{pmatrix} \dfrac{\partial \boldsymbol{f}_1}{\partial p_L^-} & \dfrac{\partial \boldsymbol{f}_1}{\partial p_R^+} \\ \dfrac{\partial \boldsymbol{f}_2}{\partial p_L^-} & \dfrac{\partial \boldsymbol{f}_2}{\partial p_R^+}. \end{pmatrix} \tag{E.23}$$

is given by

$$\frac{\partial \boldsymbol{f}_1}{\partial p_L^-} = A_L\left[u_L^-\frac{\partial \rho_L^-(p_L^-)}{\partial p_L^-} + \rho_L^-\frac{\partial u_L^-(p_L^-)}{\partial p_L^-}\right] - A_R u_R^+\frac{\partial \rho_R^+(s)}{\partial s}\frac{\partial s(p_L^-)}{\partial p_L^-}, \tag{E.24}$$

$$\frac{\partial \boldsymbol{f}_1}{\partial p_R^+} = -A_R\left[u_R^+\frac{\partial \rho_R^+\left(p_R^+\right)}{\partial p_R^+} + \rho_R^+\frac{\partial u_R^+\left(p_R^+\right)}{\partial p_R^+}\right], \tag{E.25}$$

$$\frac{\partial \boldsymbol{f}_2}{\partial p_L^-} = \frac{\partial h_R^+(s)}{\partial s}\frac{\partial s(p_L^-)}{\partial p_L^-} - \frac{\partial h_L^-\left(p_L^-\right)}{\partial p_L^-} - u_L^-\frac{\partial u_L^-(p_L^-)}{\partial p_L^-} \tag{E.26}$$

and

$$\frac{\partial \boldsymbol{f}_2}{\partial p_R^+} = \frac{\partial h_R^+\left(p_R^+, s\right)}{\partial p_R^+} + u_R^+\frac{\partial u_R^+(p_R^+)}{\partial p_R^+}, \tag{E.27}$$

where

$$\frac{\partial u_L^-}{\partial p_L^-} = \frac{1}{\rho_L(S_L - u_L)}, \tag{E.28}$$

$$\frac{\partial \rho_L^-}{\partial p_L^-} = \rho_L\frac{S_L - u_L}{(S_L - u_L^-)^2}\frac{\partial u_L^-}{\partial p_L^-} = \frac{1}{(S_L - u_L^-)^2}, \tag{E.29}$$

and

$$\frac{\partial u_R^+}{\partial p_L^+} = \frac{1}{\rho_R(S_R - u_R)}. \tag{E.30}$$

The derivatives related to ρ_R^+, h_R^+ and h_L^- depend on the EOS. For ideal gas they are

$$\frac{\partial \rho_R^+(p_L^-)}{\partial p_L^-} = \left[\frac{p_R^+}{p_L^-}\right]^{1/\gamma}\left(\frac{\partial \rho_L^-}{\partial p_L^-} - \frac{\rho_L^-}{\gamma p_L^-}\right), \tag{E.31}$$

$$\frac{\partial \rho_R^+}{\partial p_L^+} = \frac{\rho_L^-}{\gamma p_R^+}\left[\frac{p_R^+}{p_L^-}\right]^{1/\gamma}, \tag{E.32}$$

$$\frac{\partial h_L^-\left(p_L^-\right)}{\partial p_L^-} = \frac{\gamma}{\gamma-1}\frac{1}{\rho_L^-}\left[1-\frac{p_L^-}{\rho_L^-}\frac{\partial \rho_L^-}{\partial p_L^-}\right], \tag{E.33}$$

$$\frac{\partial h_R^+}{\partial p_L^-} = -\frac{\gamma}{\gamma-1}p_R^+\frac{1}{(\rho_R^+)^2}\frac{\partial \rho_R^+}{\partial p_L^-}, \tag{E.34}$$

and finally

$$\frac{\partial h_R^+\left(p_R^+, s\right)}{\partial p_R^+} = \frac{\gamma}{\gamma-1}\frac{1}{\rho_R^+}\left(1-\frac{p_R^+}{\rho_R^+}\frac{\partial \rho_R^+}{\partial p_R^+}\right). \tag{E.35}$$

F. Configuration data for CONSTRUCT

In this work, the exact solutions of the Euler equations with area change for Test 3, 4, and 5 were produced by Andrianov's MATLAB program CONSTRUCT [36]. Below, the configuration datafiles needed to produce these exact solutions in CONSTRUCT are given. This solver is mainly designed for the Baer-Nunziato equations, but due to the equivalency between the Euler equations with area change and the Baer-Nunziato equations, the solver can be used for the Euler equations with area change as well.

F.1. Test 3

```
##############Remarks to solution##############
Strong shock test
###############################################
Domain
0    % a: left interval bound
1    % b: right interval bound
0.5  % Position of diaphragm
300  % Number of cells
0.1  % Output time
Phase constants
1.4  % Gamma for the solid phase
0    % Pi for the solid phase
1.4  % Gamma for the gas phase
0    % Pi for the gas phase
Parameters at U0 (left of solid contact)
0.1  % Solid volume fraction left
1    % Solid density at U0
0    % Solid velocity at U0
1    % Solid pressure at U0
1    % Gas density at U0
0.1  % Gas velocity at U0
1    % Gas pressure at  U0
Some parameters at U1 (right of solid contact)
0.8  % Solid volume fraction right
1    % Solid density behind the solid contact
Waves
rg2c 0.5     % Right gas contact
rg3s 2   % Right gas 3-shock
lg1r 3   % Left gas 1-rarefaction
```

F.2. Test 4

F.2.1. Configuration A

```
##############Remarks to solution##############
the non—realizable conf A
###############################################
Domain
0    % a: left interval bound
2    % b: right interval bound
0.5  % Position of diaphragm
300  % Number of cells
0.4  % Output time
Phase constants
1.4  % Gamma for the solid phase
0    % Pi for the solid phase
1.4  % Gamma for the gas phase
0    % Pi for the gas phase
Parameters at U0 (left of solid contact)
0.2  % Solid volume fraction left
1    % Solid density at U0
0    % Solid velocity at U0
10   % Solid pressure at U0
0.2069287047486187   % Gas density at U0
3.991374155713258    % Gas velocity at U0
0.07141302258941416  % Gas pressure at  U0
Some parameters at U1 (right of solid contact)
0.7  % Solid volume fraction right
1    % Solid density behind the solid contact
Waves
rg1s 0.9498449509699555  % Right gas 1—shock
rg2c 0.7238127005244245  % Right gas contact
rg3s 2.747750293276058   % Right gas 3—shock
```

F.2.2. Configuration B

```
##############Remarks to solution##############
The realizable conf B.
###############################################
Domain
0    % a: left interval bound
2    % b: right interval bound
0.5  % Position of diaphragm
300  % Number of cells
0.4  % Output time
Phase constants
1.4  % Gamma for the solid phase
0    % Pi for the solid phase
```

```
1.4  % Gamma for the gas phase
0    % Pi for the gas phase
Parameters at U0 (left of solid contact)
0.2  % Solid volume fraction left
1    % Solid density at U0
0    % Solid velocity at U0
10   % Solid pressure at U0
1.108788473166335    % Gas density at U0
0.338206979126617    % Gas velocity at U0
3.466645541783839    % Gas pressure at  U0
Some parameters at U1 (right of solid contact)
0.7  % Solid volume fraction right
1    % Solid density behind the solid contact
Waves
rg2c 0.7     % Right gas contact
rg3s 2   % Right gas 3—shock
lg1s —0.5    % Left gas 1—shock
```

F.3. Test 5

F.3.1. Configuration B

```
##############Remarks to solution##############
The realizable conf B.
###############################################
Domain
0    % a: left interval bound
1    % b: right interval bound
0.7  % Position of diaphragm
300  % Number of cells
0.2  % Output time
Phase constants
1.4  % Gamma for the solid phase
0    % Pi for the solid phase
1.4  % Gamma for the gas phase
0    % Pi for the gas phase
Parameters at U0 (left of solid contact)
0.7  % Solid volume fraction left
1    % Solid density at U0
0    % Solid velocity at U0
1000     % Solid pressure at U0
0.5093607318859084   % Gas density at U0
0.2142492415498989   % Gas velocity at U0
4.135537209047921    % Gas pressure at  U0
Some parameters at U1 (right of solid contact)
0.2  % Solid volume fraction right
1    % Solid density behind the solid contact
Waves
lg1s —1.780671535653408  % Left gas 1—shock
rg2c 1.092675618708552   % Right gas contact
```

```
rg3s 0.9943557227438373  % Right gas 3-shock
```

F.3.2. Configuration D

```
##############Remarks to solution##############
Configuration D
###############################################
Domain
0    % a: left interval bound
1    % b: right interval bound
0.7  % Position of diaphragm
300  % Number of cells
0.2  % Output time
Phase constants
1.4  % Gamma for the solid phase
0    % Pi for the solid phase
1.4  % Gamma for the gas phase
0    % Pi for the gas phase
Parameters at U0 (left of solid contact)
0.7  % Solid volume fraction left
1    % Solid density at U0
0    % Solid velocity at U0
1    % Solid pressure at U0
0.5552061419927415   % Gas density at U0
-3.842416666495061   % Gas velocity at U0
0.2923425377966596   % Gas pressure at  U0
Some parameters at U1 (right of solid contact)
0.2  % Solid volume fraction right
1    % Solid density behind the solid contact
Waves
lg3s -0.1512908326786574     % Left gas 3-shock
lg2c 0.6288002023059001  % Left gas contact
lg1s -2.907208535818758  % Left gas 1-shock
```

G. Boundary conditions for the converging-diverging nozzle tests with the ideal gas EOS

For subsonic flow, though it is common to set only pressure and temperature at the nozzle inlet, we here also set $u_0 = 0$ to ensure the stable buildup to the steady state. This means that the pressure, p_0 and temperature T_0 were set to rather high values such that there is sufficient flux from the stagnant ghost-cell to the moving flow in the nozzle. For the outlet, the pressure was set and u, T were extrapolated. The values are presented in Table G.1. In the plot for these tests the ghost cells are omitted, otherwise there is a long "tail" up to the cell 0 value for the pressure and temperature and down to the Mach number and velocity of 0.

Table G.1.: Boundary conditions for the ideal gas converging-diverging nozzle tests with subsonic flow

Inlet Mach	p_0	u_0	T_0	p_{N_j+1}
≈ 0.05	1.0	0.0	1.0	0.93
≈ 0.15	1.0	0.0	1.0	0.8
≈ 0.30	1.0	0.0	1.0	0.633

For supersonic flow, p, u, T is set at the inlet and extrapolated at the outlet. The values set at the inlet are presented in Table G.2.

Table G.2.: Boundary conditions for the ideal gas converging-diverging nozzle tests with supersonic flow

Inlet Mach	p_0	u_0	T_0
≈ 2.28	10.0	2.63	1.0
≈ 2.60	10.0	3.1	1.0
≈ 3.00	10.0	3.55	1.0

Alexandra Metallinou Log

Master's thesis

NTNU
Norwegian University of
Science and Technology